



Universiteit
Leiden
The Netherlands

Quantum dots in microcavities: from single spins to engineered states of light

Steindl, P.

Citation

Steindl, P. (2023, July 5). *Quantum dots in microcavities: from single spins to engineered states of light*. *Casimir PhD Series*. Retrieved from <https://hdl.handle.net/1887/3629753>

Version: Publisher's Version

License: [Licence agreement concerning inclusion of doctoral thesis in the Institutional Repository of the University of Leiden](#)

Downloaded from: <https://hdl.handle.net/1887/3629753>

Note: To cite this publication please use the final published version (if applicable).

**Quantum dots in microcavities:
From single spins to engineered quantum states of light**

Proefschrift

ter verkrijging van
de graad van doctor aan de Universiteit Leiden,
op gezag van rector magnificus prof.dr.ir. H. Bijl,
volgens besluit van het college voor promoties
te verdedigen op woensdag 5 juli 2023
klokke 16:15 uur

door

Petr Steindl

geboren te Brno, Tsjechië
in 1994

Promotor: Prof. dr. D. Bouwmeester

Co-promotor: Dr. W. Löffler

Promotiecommissie: Prof. dr. J. Finley (Technical University of Munich, Munich, Germany)

Prof. dr. P. Senellart-Mardon (Université Paris-Saclay, Paris, France)

Dr. S. Bhattacharyya

Dr. E.P.L. van Nieuwenburg

Prof. dr. J.M. van Ruitenbeek

Prof. dr. J. Aarts

Casimir PhD series, Delft-Leiden 2023-12

ISBN: 978-90-8593-560-5

An electronic version of this thesis can be found at <https://openaccess.leidenuniv.nl>

The research project described in this thesis was conducted at the Leiden Institute of Physics, Leiden University. The project received funding from the European Union's Horizon 2020 research and innovation programme under grant agreement No. 862035 (QLUSTER) and by the Netherlands Organisation for Scientific Research (NWO/OCW), as part of the Frontiers of Nanoscience program (NanoFront) and the Quantum Software Consortium (project number 024.003.037 / 3368).



Universiteit Leiden



Copyright © 2023 Petr Steindl

The cover designed by Alexander Kuric shows a single-photon emitting device used in this thesis - a semiconductor quantum dot embedded in a Fabry-Perot microcavity.

Schematics of optical setups use components adapted from the *ComponentLibrary* by Alexander Franzen, which is licensed under a CC BY-NC 3.0 Licence.

Contents

1	Introduction	1
1.1	Single photons	1
1.2	From single to entangled photons	2
1.3	The QD as a spin-photon interface	3
1.4	Resonant laser spectroscopy	3
1.5	Thesis outline	4
2	Cavity-QD device with an electron blocking layer	5
2.1	Cavity design	6
2.2	A QD in a micropillar cavity	8
2.2.1	Growth	8
2.2.2	Electrical tuning of QD state	8
2.3	Trion identification of QD spin-state configuration in the presence of an optical cavity	10
2.3.1	Resonant Stark spectroscopy under cross-polarization	10
2.3.2	Resonant spectroscopy in an in-plane magnetic field	11
2.3.3	Semi-classical model	12
2.4	Single-photon emission	13
3	Cross-polarization extinction enhancement and spin-orbit coupling of light for quantum-dot cavity-QED spectroscopy	15
3.1	Introduction	16
3.2	Scattering elimination	17
3.3	Vector-beam effects upon multiple reflections	18
3.4	Single emitter polarization extinction improvement	19
3.5	Conclusions	22
3.6	Appendix	23
3.6.1	Scattering elimination with various analyzers	23
3.6.2	Maximal polarization extinction upon multiple reflections	24
4	Resonant two-laser spin-state spectroscopy of a negatively charged quantum dot-microcavity system with a cold permanent magnet	25
4.1	Introduction	26
4.2	Permanent magnet assembly	26
4.3	Spin-state determination	28
4.4	Two-color resonant laser excitation	30
4.5	Conclusions	33
4.6	Appendix	35
4.6.1	Permanent magnet assembly simulations	35
4.6.2	Experimental setup and characterization	36
4.6.3	Single-laser resonance fluorescence	37

4.6.4	Rate-equation model of resonant two-color spectroscopy of a negatively charged exciton	39
4.6.4.1	Spin population rate equations	39
4.6.4.2	2D two-color resonant excitation model	40
4.6.4.3	Estimate of excitation and detection rates	41
4.6.4.4	Model rates estimation	41
4.6.4.5	Excitation-power dependent two-color resonant excitation	42
5	Single-photon addition and photon correlations	47
5.1	Introduction	48
5.2	Displaced Fock states from quantum interference	48
5.2.1	Influence of loss	50
5.3	Photon correlations	50
5.4	Effect of photon indistinguishability	52
5.5	Single-photon addition with quantum dot sources	53
5.6	Conclusions	55
5.7	Appendix	56
5.7.1	Derivation of $g_{\theta}^{(2)}(0)$	56
5.7.2	Photon correlations: single-photon-added coherent states vs displaced Fock states	57
6	Artificial coherent states of light by multi-photon interference in a single-photon stream	59
6.1	Introduction	60
6.2	Single-photon source	60
6.3	Photon correlations between source and delay loop	63
6.4	Building artificial coherent states	63
6.5	Conclusions	66
6.6	Appendix	68
6.6.1	The two-photon picture	68
6.6.1.1	Detection of VH correlations	68
6.6.1.2	Detection of HH correlations	69
6.6.1.3	Relation to source correlations	70
6.6.1.4	Loss in the delay loop	70
6.6.2	Simulation details	71
6.6.2.1	Quantum interference at waveplate WP2 in the delay loop	72
6.6.2.2	Delay loop: Round-trip loss and diffraction	73
6.6.3	Visibility measurement	74
6.6.4	How many photons do interfere?	75
6.6.5	Properties of the artificial coherent state	76
	Bibliography	78
	Summary	99
	Samenvatting	101
	Curriculum Vitae	103

List of publications	105
Acknowledgements	107

1 Introduction

1.1 Single photons

Photons, the elementary quantum particles of light, are truly fascinating objects. Some studies even suggest that the human eye can register them individually, despite typically being processed in much larger quantities [1]. The availability of sources of entangled photons has made photons the most popular platform to demonstrate quantum phenomena such as quantum superposition, quantum non-locality [2], and quantum teleportation [3]. Since then, scientists fascinated by quantum theories have designed a variety of applications based on these properties. For example, many photons in linear optical networks have recently achieved an important demonstration of the “quantum advantage” [4]. Also, for universal quantum computation, photons have potential, either in the form of many single photons [5–7] or using multi-photon entangled states such as cluster states [8–11] as a resource. In the one-way quantum computing scheme [8], challenges from probabilistic or deterministic two-photon gates are shifted to the engineering of large-scale cluster states [12]. The weak interaction with the environment protects photons from decoherence, but this also limits their interaction with matter or with other photons, therefore it is in fact hard to generate both single photons and cluster states in the first place.

In this thesis, we follow one of the roadmaps of single and entangled photon generation – using a III-V self-assembled InGaAs quantum dot (QD) embedded in an optical microcavity. Electrons and holes in the QD have discrete energy levels similar to atoms. Under resonant excitation, the QD can be considered a two-level system and transitions between the states happen by the absorption or emission of a photon. Like for atoms, this interaction is in homogeneous materials not efficient, and therefore, we embed the quantum dot in a Fabry-Perot cavity formed by two highly reflective mirrors. This leads to an increased interaction of light with the QD, and allows for deterministic photon-matter interaction. Furthermore, inserting the QD into a cavity leads to acceleration of the emission into the particular cavity mode, known as the Purcell effect, with two important effects on single-photon generation. First, the single-photon collection benefits from this effect because the QD preferentially emits into the selected cavity mode. Second, the Purcell effect shortens the recombination time of the QD electron-hole pair, leading to higher photon indistinguishability due to a reduced influence of dephasing. Together with the fact that a two-level system can only emit one photon at a time, the QD-cavity system is a near-ideal source of single photons and allows for photon generation on demand [13–15].

Tremendous progress has been made in the last decade with QD-cavity-based single-photon sources [16], where scientists carefully optimized every single device parameter [17] and brought these sources close to perfection. The best single-photon sources now show excellent single-photon purity (97.9%), indistinguishability (97.5%), and brightness (57%) [15]. The possibility to collect photons efficiently with an optical fiber directly attached to the top of the single-photon-source semiconductor chip [18] and commercialization thereof [19] makes these sources also very appealing for wide distribution and application in a variety of quantum technologies. High-quality true single-photon sources

would be a crucial advantage for optical quantum computing approaches.

For applications in quantum networks, key challenges are the indistinguishability of photons produced by separate single-photon sources and the photon wavelength, which should be compatible with telecom technologies. Because QD properties, including emission wavelength, can be tailored by the nanostructure composition, scientists are positive about a bright telecom single-photon near-term future. Already now, the first telecom single-photon sources have been reported, either based on InP technology [20, 21] or frequency conversion [22]. Yet, the preparation of two (or more) identical single-photon emitters necessary for large quantum networks is still an open problem, mostly due to limited control of the atomic-scale composition of individual QDs during their self-assembly [23]. Only recently, advanced QD growth techniques such as droplet etching epitaxy [24, 25] have allowed demonstration of two-photon interference with near-unity visibility (93.0 %) using photons from two completely separate quantum dots [26].

1.2 From single to entangled photons

Having access to QD-cavity-based sources of high-quality and indistinguishable single photons allows us to manipulate them and synthesize never-produced complex quantum states of light. This simply requires an optical beam splitter: If two indistinguishable photons arrive simultaneously at the two inputs of a beam splitter, the photons will “bunch” and exit the beam splitter always together through one exit port. This result is very different from the classical situation, where there is always a finite probability that photons leave the beam splitter separately. This photon bunching is a purely quantum effect called Hong-Ou-Mandel (HOM) interference [27] and allows, for example, a direct comparison of two states of light. This state comparison is used to experimentally characterize the photon indistinguishability of single-photon emitters [28] or for guaranteeing security in quantum network protocols [29].

In quantum optics, by only using beam splitters and phase shifters, one can construct arbitrary unitary operations on quantum states of light for quantum information processing [30, 31], where the HOM effect plays an essential role. On the long way towards the processing, there is a simpler interesting application of repeated HOM interference - boson sampling [32], where several indistinguishable photons in Fock states are combined in a large free-space or integrated-optics interferometer [4, 33–35]. This interferometer or photonic circuit implements an unitary operation from the inputs to its outputs. The outcome of this circuit is computationally hard to calculate on classical computers [36], making boson sampling useful to demonstrate a “quantum advantage”. A few proof-of-principle experiments with photons have been reported, including realizations with de-multiplexed single photons from a QD-cavity system [34, 35]. The largest photonic interferometer to date with true single photons was implemented in free space with 60 input and output ports and 20 single photons prepared by de-multiplexing of a QD-cavity single-photon source [37]. Despite the enormous size of the Hilbert space accessible in the experiment (3.7×10^{14}), corresponding to 48 qubits, the interferometer was built only for a specific unitary operation. Currently, scientists are developing large, scalable, and programmable photonic chips (or processors) [38], enabling the implementation of arbitrary linear optical transformations necessary for universal photonic quantum computing.

Moreover, having these processors, we can engineer complicated photonic states, including multi-photon entangled states such as cluster states [39], for other quantum applications. Sometimes, for a specific application, the interferometer can be strongly simplified.

For example, using time-bin photon encoding, boson sampling can be performed with a single beam splitter, if photons from one exit mode are directed back to the same beam splitter, forming an optical delay loop [40, 41]. Here, the delayed loop-photons interfere with single photons from the source and develop complex photon statistics [41]. A similar optical delay loop was used to entangle sequentially emitted single photons from a QD-cavity device into a linear cluster state [42]. In general, entanglement of many photons using linear optical interferometers is often not fully deterministic, this is where the QD again provides solutions as we discuss now.

1.3 The QD as a spin-photon interface

Another remarkable property of quantum dots is to trap a charge carrier. This confined extra electron or hole provides a spin to the originally empty ground state. This spin can be used as a quantum memory with information encoded in the spin orientation [43]. The extra charge changes the QD optical selection rules connecting the photon polarization to the spin state, therefore the charge level of the QD can be confirmed by polarization analysis of the single photons emitted by the QD [44].

The singly-charged QD has two ground states of opposite spin. These states are naturally energy degenerate but can be split by the Zeeman effect in an external magnetic field. This splitting enables spin initialization [45, 46] and read-out [47] with optical fields, therefore entangling photons with the single spin. Due to the recent impressive improvement of the spin coherence time up to $T_2 = 0.113$ ms [48], the QD spin can be entangled with many photons during the spin coherence time. This, in combination with entanglement swapping [49] using the HOM effect at a beam splitter, is an essential tool to establish a quantum link between distant places. Integrating the charged QD into an optical cavity to accelerate the spin-photon entangling rate would further increase the remote-entanglement generation rate, but cavity-QD devices with both high Purcell-accelerated emission and extra-long spin coherence still have to be optimized.

Moreover, spin-photon entanglement generation in combination with spin precession in a weak magnetic field also allows for the deterministic generation of linear cluster states [50]. Here, each emitted photon is entangled with the same spin, and the spin can be “traced out” in the end to obtain a purely photonic entangled state. Despite being deterministic in principle, this scheme has been experimentally limited by reduced photon collection efficiency to less than 1% due to the absence of a cavity [51, 52]. Only recently, using a charged exciton in a Fabry-Perot cavity, the group of Pascale Senellart achieved three-particle entanglement with fidelities up to 63% [53].

1.4 Resonant laser spectroscopy

Any successful quantum protocol starts with qubit initialization, often carried out by excitation with a resonant laser. In singly-charged QDs, successful spin initialization can be detected by observation of the QD resonant fluorescence because of the optical selection rules. For this, the weak QD emission has to be separated from the stronger excitation laser light. This laser filtering is typically done in the polarization degree of freedom using cross-polarization where the excitation and detection polarizations are orthogonal, and cross-polarization extinction ratios up to 10^8 [54] have been achieved. Surprisingly, these ratios are more than one order of magnitude higher than expected from the specification

of the polarizers. The physical origin of this has been an open question until recently [55], and turns out to be a combination of residual ellipticities and spin-orbit coupling of light. Since QD-cavity systems require cryogenic temperatures, it is essential to also achieve high extinction ratios in a cryostat - which is complicated by several issues, from the cavity birefringence to strained cryostat windows.

1.5 Thesis outline

In Chapter 2, we introduce and characterize our cavity device containing singly-charged QDs. Further, we present a resonant spectroscopy toolbox used for QD spin-state identification and characterization.

In Chapter 3, we experimentally study cross-polarization extinction in several optical setups, including firstly in a cryogenic confocal microscope. We find that using optical reflection with single-mode filtering detection leads to potential cross-polarization extinction improvement above the limit given by bare polarizers. This improvement is associated with Fresnel-reflection-induced effects, including the spin-orbit coupling of light, allowing for small pre-compensation of the residual ellipticity of linear polarizers. We identify this effect in confocal microscopy and use it to demonstrate improvement in single-photon emission from a singly charged quantum dot in a birefringent optical microcavity.

In Chapter 4, we develop a cryogenic permanent (Voigt geometry) magnet assembly and use it to split the electron spin states of a charged QD resonant with a micropillar cavity. Then, using two-color resonant spectroscopy, we demonstrate spin population manipulation by controlling the relative power of the excitation lasers, and we observe an increase in single-photon emission.

Adding a single photon on a highly reflective beam splitter to a classical optical field is a known but experimentally challenging technique to prepare complex multi-photon quantum states. In Chapter 5, we theoretically study this scheme for the generation of displaced Fock states with various single-photon sources. By analytical theory, we show that photon-correlations of the produced states exhibit a global maximum as a function of the strength of the single-photon state. Further, we discuss experimental realization and the use of photon correlations to optimize the mode-matching between single-photon and coherent states.

In Chapter 6, we use our QD-cavity device as a single-photon source, and by repeated quantum interference we build from the single-photon stream complex photon-number superposition states with tunable photon statistics, including approximately coherent states of light. The engineered artificial coherent states are more complex than the conventional coherent states, containing quantum entanglement of photons, making them a promising resource of multi-photon entanglement.

2 Cavity-QD device with an electron blocking layer

For the research in this thesis, we use self-assembled quantum dots embedded in optical microcavities with a cavity design originally developed for semiconductor lasers [56–58] (and Ph.D. theses [59–61]). The cavity is formed by two distributed Bragg reflectors (DBR) around a λ -thick active region of a *p-i-n* junction containing semiconductor quantum dots (QDs) and a $3/4\lambda$ -thick oxide aperture. For this research, the design was adopted with a small change in the diode active region, allowing deterministic QD spin loading due to an added electron-blocking layer. In this chapter, we discuss the optical properties of devices with this blocking layer and discuss experimental techniques we use to determine the spin state and certify the single-photon emission of our QDs.

2.1 Cavity design

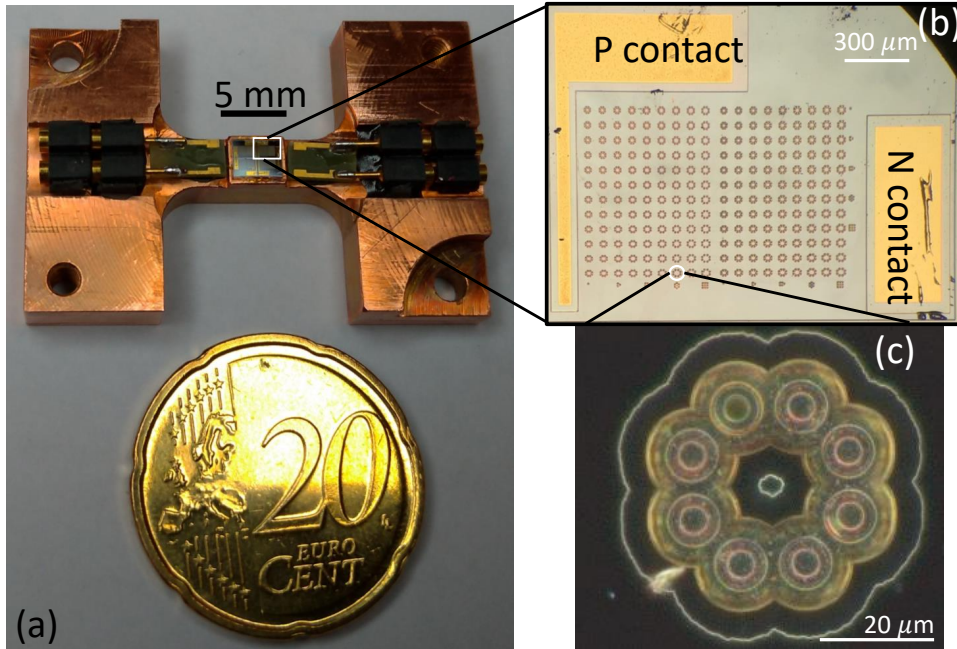


Figure 2.1: Optical images of the sample. (a) A photograph of the sample glued on the sample holder. (b) An optical microscope image of one-quarter of the semiconductor chip containing over 200 micropillar cavities. (c) Top view dark optical image of a cavity device after etching away the top DBR with eight etched trenches forming an octagon shape oxide aperture.

Images of the sample used in this thesis are shown in Fig. 2.1. Figure 2.1(a) is an optical image of the sample holder with the semiconductor chip glued on top and electrically connected through gold wire bonds to electric contacts. Figure 2.1(b) shows an optical-microscope image of one-quarter of the chip with over 200 micropillar cavities with common electrical contacts. Panel (c) shows the top view on a cavity device with eight holes etched in an octagon shape into the top cavity mirror. Due to refractive index contrast, we easily distinguish the oxide aperture from the cavity center.

Figure 2.2(a) shows the cross-sectional plot of the micropillar design. The top DBR mirror is composed of 26 pairs of $\lambda/4$ -thick layers of GaAs and $\text{Al}_{0.9}\text{Ga}_{0.1}\text{As}$, while the bottom mirror consists of 13 pairs of layers of GaAs and AlAs and 16 pairs of GaAs and $\text{Al}_{0.9}\text{Ga}_{0.1}\text{As}$ layers. The oxide aperture used to increase in-plane light confinement (due to the reduction of refractive index from $n \approx 3$ to $n \approx 1.5$) to the center of the cavity is prepared by wet oxidation of a 10-nm AlAs layer embedded in the p -rich layer [63, 64]. We use an octagon-shaped oxide aperture with eight holes which we also call trenches. On the chip, the distance between the trenches varies cavity-to-cavity by design, allowing the manufacture of oxide apertures of different diameters and ellipticities. Reduction of the aperture diameter yields smaller cavity mode volumes due to stronger transverse light confinement while varying ellipticity allows controlling the fundamental cavity mode splitting [64]. The QD layer is grown in an intra-cavity electric-field anti-node in the intrinsic region of the p - i - n junction at a position determined by transmission matrix method (TMM) calculations.

In Fig. 2.2(b), we show a polarization-resolved spectrum of cavity modes recorded

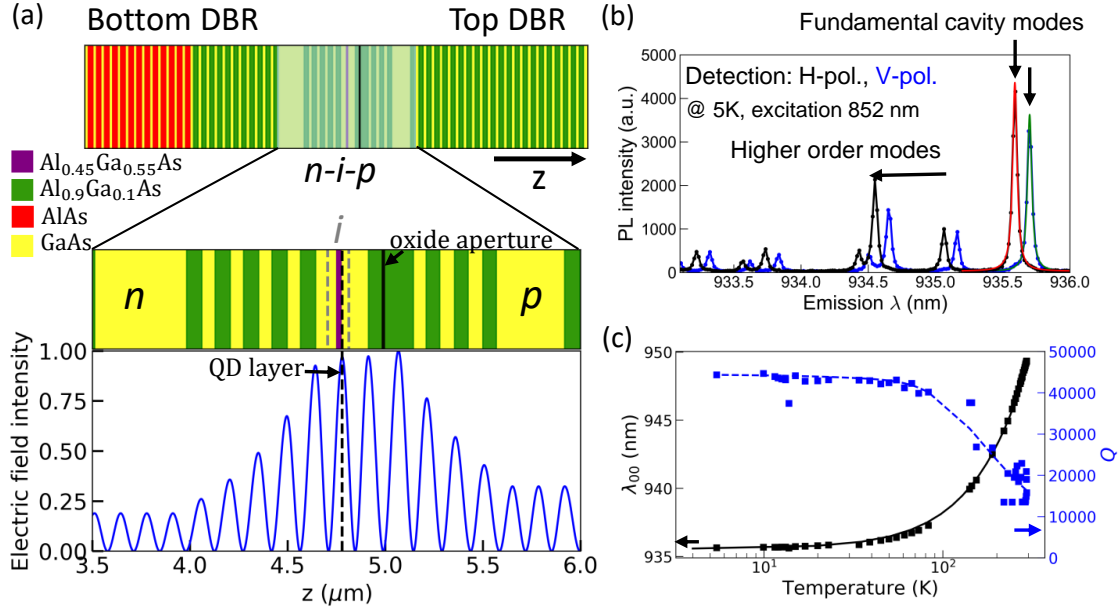


Figure 2.2: Micropillar cavity design and optical characterization. (a) TMM (transmission matrix method) cavity design with the calculated intra-cavity electric field. The gray dashed area shows the intrinsic part of the $p-i-n$ junction, including the QD layer (dashed black line). (b) The spectrum of cavity modes was measured in two orthogonal linear polarizations. (c) The temperature-mediated shift of resonant wavelength λ_{00} (black) and Q factor (blue) of the fundamental cavity mode. Symbols: experiment, solid line: TMM calculation, dashed line: Q factor calculated assuming phonon broadening of the cavity resonance [62].

with a spectrometer [65]. We intentionally did not optimize the spatial coupling of the excitation laser to the micropillar cavity to also observe higher-order cavity modes. The fundamental cavity mode presented in Fig. 2.2(b) is split by shape- and strain-induced birefringence by ~ 0.1 nm into two orthogonal linearly polarized modes (H and V). The cavity splitting was determined by a Lorentzian curve fit. Neglecting the mode-splitting, the measured resonant wavelength of about 935.5 nm agrees well with simple TMM calculation.

In Fig. 2.2(c), we confirm the device design by monitoring the fundamental mode wavelength λ_{00} and quality factor Q as a function of sample temperature. The wavelength λ_{00} shifts towards higher wavelengths due to material expansion at elevated temperatures and band-gap changes influencing the refractive index. We reproduce this shift with a simple temperature-dependent TMM simulation where the real part of the refractive index is temperature dependent because of shifts of the band gaps [66] and cavity expansion by lattice parameters [67]. We correct the modeled temperature dependence of λ_{00} in Fig. 2.2(c) by subtraction of 1.07 nm. This correction is needed to account for other effects, such as band-gap changes induced by mechanical stress [68] created by multi-layer stacking or for a complex spatial profile of oxidation aperture. At 5 K, we measure a Q factor of around 43 000, in good agreement with the simulations.

2.2 A QD in a micropillar cavity

2.2.1 Growth

We use self-assembled semiconductor QDs grown in Stranski-Krastanov growth mode with molecular-beam epitaxy [69, 70]. After the deposition of 1.5 monolayers of indium arsenide (InAs) on gallium arsenide (GaAs) buffer (at 500 °) [71], it becomes energetically favorable to form small nanometer-scale islands and thus partially release accumulated strain energy induced by material lattice mismatch. This self-organization simultaneously occurs at random positions on the wafer and leads to the assembly of few-nanometers high pyramid-shaped islands with high crystalline quality [72], the InGaAs quantum dots.

The GaAs matrix with a higher semiconductor band gap than InGaAs QDs serves as a three-dimensional potential barrier for charge carriers in the InGaAs, leading to the carrier localization within the In-rich region. The strong confinement of the carriers in the QD results in electron and hole state energy quantization responsible for sharp optical transitions between these discrete levels observed at cryogenic temperatures, similar to atoms [73].

Unlike in atoms, electronic states and optical properties of QDs can be tailored by the size, shape, and composition of the QDs and the surrounding material. We use this tunability during the final phase of the QD growth. First, the GaAs capping layer is deposited, limiting indium atom diffusion and ensuring both electron- and hole-carrier localization in the QD [74, 75]. Then, the composition and emission energy of QDs are adjusted by In-Ga atom intermixing driven by thermal annealing at 600 ° [76].

2.2.2 Electrical tuning of QD state

We embed a single layer of QDs in the active region of a *p-i-n* junction. Figure 2.3(a) shows a sketch of the *p-i-n* junction band scheme, where the red dashed line indicates the Fermi level. We can use the Fermi level adjustment by applying lateral bias voltage V_G to fine-tune the QD transition energy via the quantum-confined Stark effect. This effect was identified by Miller et al. [77], and it became a popular tool in the quantum dot community [78–82] to engineer the QD emission energy. The emission energy can be described by $E(F) = E_0 - pF - \beta F^2$, where p is the permanent electric dipole, β the polarizability of a QD with zero bias energy E_0 [80, 83]. Our *p-i-n* diode has a built-in voltage $V_{bi} \approx 0.95$ V, resulting in an electric field $F = (V_G - V_{bi})/d$ in the intrinsic region of thickness $d \approx 142$ nm [84]. Due to the built-in voltage, the flat-band condition ($F = 0$ kVcm⁻¹) is reached at $V_G = V_{bi}$. Figure 2.3(b) presents the Stark-shift of a single dot with $p = 7 \pm 1$ $\mu\text{eV kV}^{-1}\text{cm}$, $\beta = 0.16 \pm 0.02$ $\mu\text{eV kV}^{-2}\text{cm}^2$, $E_0 = 1318.0 \pm 0.1$ meV - values typical for InGaAs QDs [84]. This control of the electronic energy levels is essential in cavity quantum electrodynamics for tuning the QD transition into resonance with the optical cavity [18, 85] or for control of photon indistinguishability from remote quantum emitters [26, 86, 87].

Depending on the total spin number of the QD ground state, QDs host a variety of excitonic states [88, 89]. Excitonic states of the main interest in this thesis are neutral excitons X^0 formed by a single excitation of initially empty QD and singly-charged excitons X^- , where the QD confines an extra electron before the excitation. Due to different spin configurations, these excitonic complexes also have distinct optical selection rules assisting the optical transitions: emission of a linearly polarized photon from X^0 and a photon of circular polarization from X^- . We show sketches of the optical selection rules

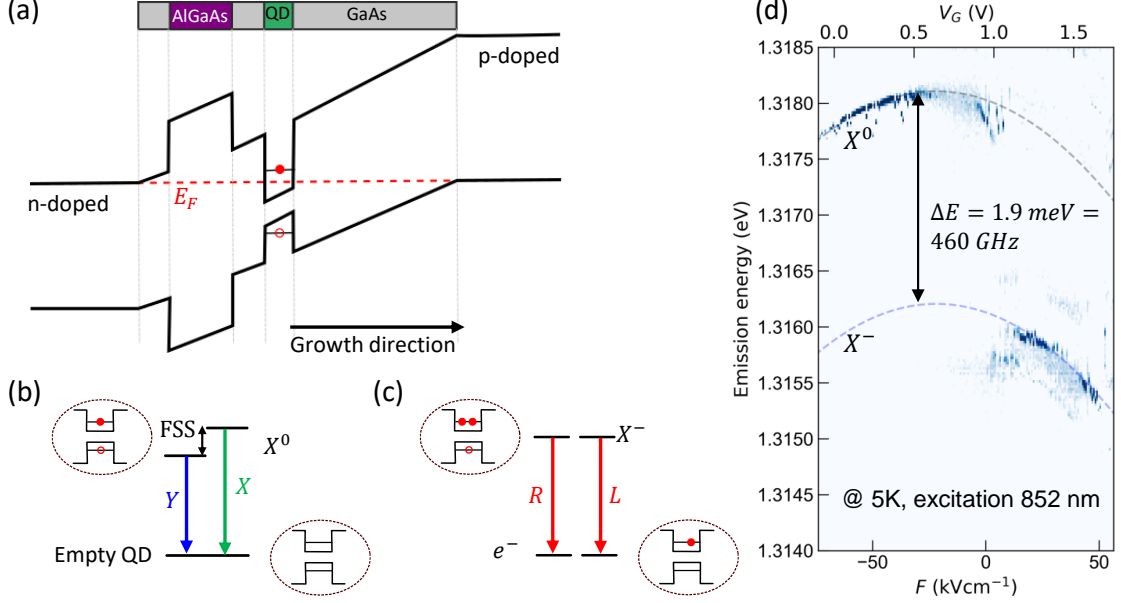


Figure 2.3: Electric field tuning of a QD transition: (a) Sketch of the band alignment in the p - i - n region of the micropillar cavity. Applying a bias voltage shifts the QD levels and allows for fine band-gap tuning. (b,c) Sketches of energy levels with optical selection rules of the neutral X^0 and negatively charged exciton X^- . Excess electrons (full circles) in the conduction band and holes (empty red circles) in the valence band are represented. (d) Voltage-induced tuning of the photon energy of a single QD resolved using off-resonant (excitation $\lambda = 852$ nm, $55 \mu\text{W}$) photoluminescence spectroscopy. Around $V_G = 1$ V, we observe single-electron charging of the QD.

in Fig. 2.3(b,c). In fact, due to QD geometry, there are two orthogonally polarized neutral excitons (denoted as X, Y) separated by the fine structure splitting (FSS) energy. Previous studies of our QDs showed FSS energy between 2 GHz and 4 GHz [18, 90].

During sample growth, we included a 21.8 nm thick $\text{Al}_{0.45}\text{Ga}_{0.55}\text{As}$ layer 5 nm below the QD layer [91, 92]. The combination of the bias control and the extra blocking layer allows for the deterministic trapping of an excess electron (a carrier in general) in the QD and the formation of the negatively charged exciton X^- . If the excess electron is trapped, the QD excitonic complex changes, resulting in a sudden step in the emission energy of the QD [93], while p and β defined dominantly by QD geometry are unchanged [94, 95]. Figure 2.3(d) shows a typical bias-resolved photoluminescence with parabolic dependence given by p and β , and an energy step of $\Delta E = 1.9$ meV ($= 460$ GHz) above $V_G = 1$ V. This energy step is a signature of single-electron charging of a neutral exciton ($V_G < 1$ V) and formation of a negative trion ($V_G > 1$ V). The binding energy ΔE is in good agreement with trion binding energies reported in literature [88, 93, 96], supporting the identification of trion formation. Above $V_G = 1$ V (and below threshold voltage $V_G = 1.52$ V of GaAs at cryogenic temperature), the device works in the Coulomb blockade regime and provides extra spin to access single-spin physics and to implement a spin quantum memory [43].

2.3 Trion identification of QD spin-state configuration in the presence of an optical cavity

Typically, the distinct optical selection rules allow mapping of the polarization of an emitted photon to the QD spin-state configuration. Probably the simplest experiment to learn about polarization is to perform polarized photoluminescence spectroscopy of the QD. Here, the QD is excited non-resonantly with a laser, and the emission is analyzed as a function of linear polarization with a spectrometer with high spectral resolution [44,97]. Unfortunately, being limited by the resolution of our spectrometer of around 6 GHz, this simple technique is challenging for direct discrimination between a single emission line of a trion and that of an exciton doublet with FSS, which is approximately two times smaller than the resolution. Instead, we use resonant excitation spectroscopy, where the spectral resolution is given by the continuous-wave narrow-linewidth laser, scanning across the cavity fundamental modes. Combining this technique with the control of additional parameters, we can identify the spin state and obtain other information about our system. We discuss several examples below.

2.3.1 Resonant Stark spectroscopy under cross-polarization

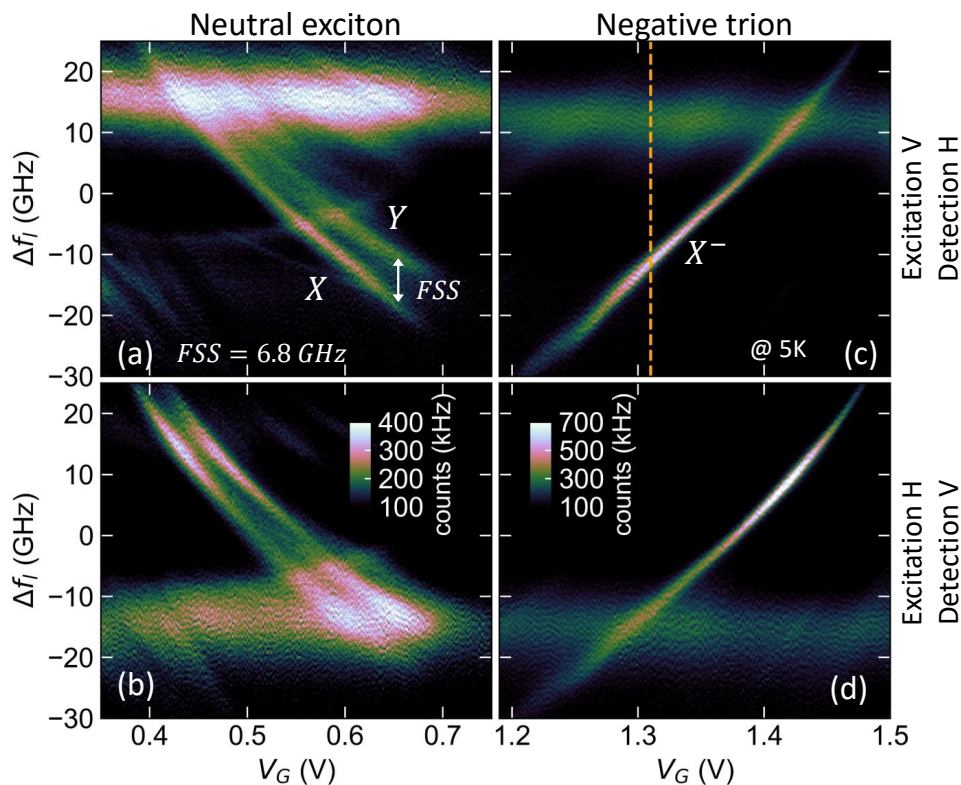


Figure 2.4: QD spin state identification using the Stark spectroscopy with cross-polarization technique. We show voltage scans of the neutral exciton (a,b) and negatively charged trion (c,d) measured in cross-polarization with excitation polarization aligned to V - (top panels) or H - (bottom) polarization of the fundamental cavity mode. The vertical line in (c) shows the bias voltage chosen later in the photon-correlation measurement, Fig. 2.7.

The birefringent cavities that we use have their fundamental resonant mode split by several GHz into two orthogonal linearly polarized modes. We typically associate the used polarization frame with these cavity modes and label them as H - and V -polarized cavity modes. Now, we focus on configurations where the excitation laser has polarization identical to one of the cavity modes. Then, the reflected laser light can almost perfectly be filtered out from the QD emission by cross-polarization filtering with detection polarization orthogonal to excitation. This technique requires fine-tuning of the excitation and detection polarizations which is discussed in detail in the next chapter. In this chapter, we focus only on state identification using this technique. In Fig. 2.4, we compare resonant Stark spectroscopy of neutral and charged excitons, presented in the left and right columns, respectively.

First, we comment on the neutral exciton transition shown in panels (a,b). We typically observe the neutral exciton transition at bias voltages $V_G < 1$ V, in agreement with the photoluminescence spectroscopy presented above. As expected for X^0 , the resonant fluorescence reveals two emission lines (X, Y) with identical Stark shift behavior separated by the FSS energy (6.8 GHz for this QD). These two exciton transitions have orthogonal linear polarizations, however, their orientation is typically not aligned with the polarization of the cavity. Therefore, (i) we can study them both with the resonant Stark spectroscopy, and (ii) they couple to both cavity modes. Importantly, the same transition lines are identified also if the excitation and detection polarizations are swapped, see Fig. 2.4(a,b).

The optical selection rules of the negatively charged QD, on the other hand, allow in the absence of the external magnetic field only energy-degenerate emission of a circularly polarized photon with a helicity depending on the orientation of the spin in the ground state. Thus, we expect to detect a single emission line independently of the excitation polarization, in agreement with the observation in Stark spectroscopy presented in Fig. 2.4(c,d).

2.3.2 Resonant spectroscopy in an in-plane magnetic field

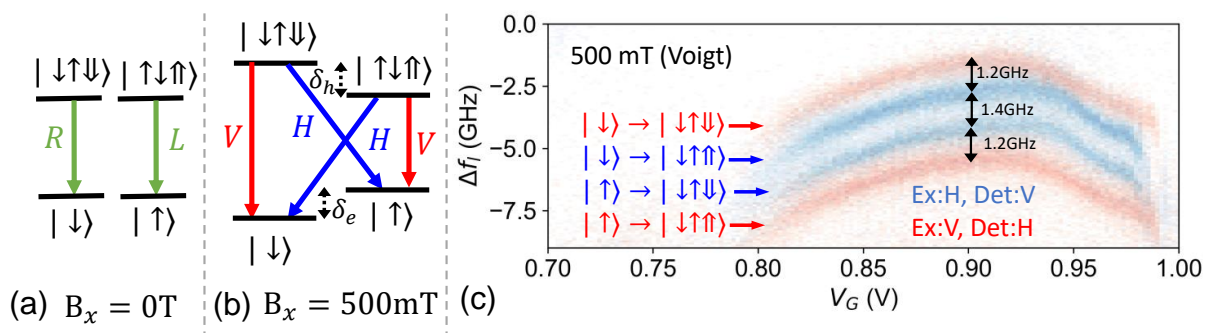


Figure 2.5: Negative trion in an in-plane magnetic field. Energy levels with optical selection rules of negatively charged QD without (a) and with (b) in-plane magnetic field. c) Resonant spectroscopy of negatively charged QD in 500 mT in-plane magnetic field. We compare resonant fluorescence spectra measured in cross-polarization for two orthogonal excitation laser polarizations: H (blue) and V (red). The detected lines are labeled according to the optical selection rules.

Another technique we use to identify trion transitions is based on mapping its spin

configuration in a weak (< 1 T) external in-plane (Voigt geometry) magnetic field. In the magnetic field, initially energy degenerate X^- transitions [Fig. 2.5(a)] are split into two pairs of separated (by Zeeman splitting) lines with orthogonal linear polarization [98], shown in Fig. 2.5(b). Experimentally, we again use Stark spectroscopy with cross-polarization detection to block the reflected excitation laser and monitor the weak QD emission as a function of bias voltage V_G , shown in Fig. 2.3(c). In this figure, we see superimposed two data sets measured with the polarization of the excitation laser aligned to V - (H -) cavity mode. We observe two “red” lines surrounding two “blue” transitions, where the color encoding represents the excitation polarization. This ordering and mutual splitting of 1.4 GHz and 3.8 GHz between the lines is characteristic of a trion with electron and hole g -factors $|g_e| = 0.18$ and $|g_h| = 0.40$. In contrast, the emission of X^0 would show only two bright lines separated already without a magnetic field by fine-structure splitting (FSS) given by QD symmetry [98, 99].

2.3.3 Semi-classical model

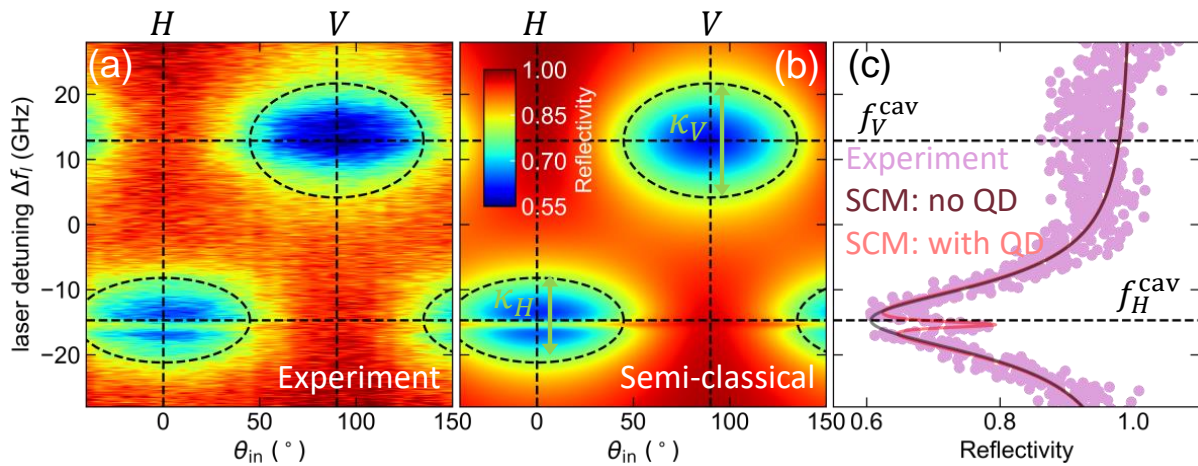


Figure 2.6: Analysis of cavity reflection as a function of laser detuning and linear input polarization. The two false-color plots show (a) experimental data and (b) polarized semi-classical theory results based on [90]. The cross-section plot in (c) compares measured data with excitation polarization direction along the H cavity mode (blue symbols) with a semi-classical model fit with (red) and without (black) QD in cavity resonance. Ellipses highlight the cavity mode resonances: resonant frequencies are shown as horizontal lines, cavity eigenpolarizations as vertical lines, and semi-minor axis is given by κ .

Another method we often use to identify the spin state of a QD coupled to a cavity is based on careful analysis of the cavity reflection as a function of excitation linear polarization direction. For the analysis, we use a semi-classical model derived in the weak coupling “bad-cavity” regime ($g \ll \kappa$) extended with the Jones formalism, allowing to include polarization effects such as cavity birefringence and optical selection rules of the QD transitions [90]. We focus on QD interaction with orthogonally polarized fundamental cavity modes with resonant frequencies f_H^{cav} , f_V^{cav} and cavity loss rates κ_H , κ_V , where the total transmission matrix of the QD-cavity system is given by

$$t_{tot} = \eta_{out} \left[\begin{pmatrix} 1 - 2i\Delta_H & 0 \\ 0 & 1 - 2i\Delta_V \end{pmatrix} + R_{-\theta_{QD}} X R_{\theta_{QD}} \right]^{-1}. \quad (2.1)$$

Here, the interaction between the laser light and cavity modes is described by the first term using the normalized laser detuning $\Delta_m = (f_l - f_m^{\text{cav}})/\kappa_m$, for $m = H, V$, where f_l is the laser frequency of the scanning laser across the cavity modes. The interaction of the cavity and the QD is included in a transmission matrix X , which is diagonal in the QD polarization basis and carries information about the QD transition optical selection rules. In general, the QD-cavity interaction induces frequency-dependent phase shift $\phi = 2C/(1 - i\Delta^{\text{QD}})$ on the light transmitted by the cavity [100]. Here, we define the normalized laser detuning $\Delta^{\text{QD}} = (f_l - f^{\text{QD}})/\gamma_{\perp}$ with respect to the QD resonance frequency f^{QD} , dephasing rate $\gamma_{\perp} = \frac{\gamma_{\parallel}}{2} + \gamma^*$, and the cooperativity parameter $C = \frac{g^2}{\kappa\gamma_{\perp}}$ describing QD-cavity interaction with coupling strength g . Using Jones vectors to describe the QD polarization selection rules, the matrix for the doublet of the neutral exciton can be represented as $X_{X^0} = \begin{pmatrix} \phi_H & 0 \\ 0 & \phi_V \end{pmatrix}$ and $X_{X^-} = \begin{pmatrix} \phi_{\sigma} & 0 \\ 0 & \phi_{\sigma} \end{pmatrix}$ in case of negative trion. Finally, because of possible misalignment of the dipole axes of the QD transitions and the cavity polarization basis, X is rotated to the cavity polarization frame by the 2D rotation matrix $R_{\theta_{\text{QD}}}$, where θ_{QD} is the angle between the cavity and QD linear polarization frames. This frame rotation is essential for the correct description of X^0 doublet, as discussed in detail in Ref. [90]. η_{out} is the probability amplitude that a photon leaves the cavity through one of the mirrors.

Experimentally, we usually measure the cavity reflection as a function of excitation linear polarization orientation. Typical data are shown in Fig. 2.6. Here, we control the linear polarization of the excitation laser by rotation of a half-wave plate, relative to the initial laser polarization. For each half-wave plate angle $\theta_{\text{in}}/2$, we measure with a single-photon detector the reflection as a function of laser detuning, this time without the polarizer in the detection path. Theoretically, the initial polarization can be described by a Jones vector $\mathbf{e}_{\text{in}} = (\cos \theta_{\text{in}}, \sin \theta_{\text{in}})^T$ and measured as $R = 1 - |t_{\text{tot}}\mathbf{e}_{\text{in}}|^2$.

In Fig. 2.6(a), we recognize two elliptical reflection dips if the laser is on-resonance with the fundamental cavity modes. As expected, the cavity modes have linear and orthogonal polarization (H and V polarization) and show energy splitting by shape- and strain-induced birefringence by $f_H^{\text{cav}} - f_V^{\text{cav}} = 29.4 \pm 0.1$ GHz. Further, the H -polarized cavity mode is intersected by a QD transition. Because we observe only a single line with emission independent of the linear excitation polarization, we identify this transition as negative trion X^- .

Now, we fit the experimental data to the polarized semi-classical model [90] and determine all relevant parameters of the cavity-QD device. First, from measurement with the QD detuned from the cavity resonance (not shown), we determine decay rates of both cavity modes: $\kappa_V = 17.5 \pm 0.3$ GHz and $\kappa_H = 13.0 \pm 0.3$ GHz. Keeping the cavity decay rates fixed, we repeat the analysis with a trion transition on resonance with the H -polarized cavity mode and find a QD relaxation rate of $\gamma_{\parallel} = 1.4 \pm 0.3$ GHz, negligible pure dephasing, and QD-cavity coupling constant $g = 1.4 \pm 0.1$ GHz.

2.4 Single-photon emission

Finally, we show that our devices function as single-photon emitters. First, we set the excitation polarization and operating bias voltage such that we resonantly excite a trion transition, shown in Fig. 2.4(c). Second, we use a cross-polarization detection scheme to separate the QD resonant fluorescence (RF) from the continuous-wave excitation laser [101] and collect the RF photons in single-mode fiber. We measure the second-order

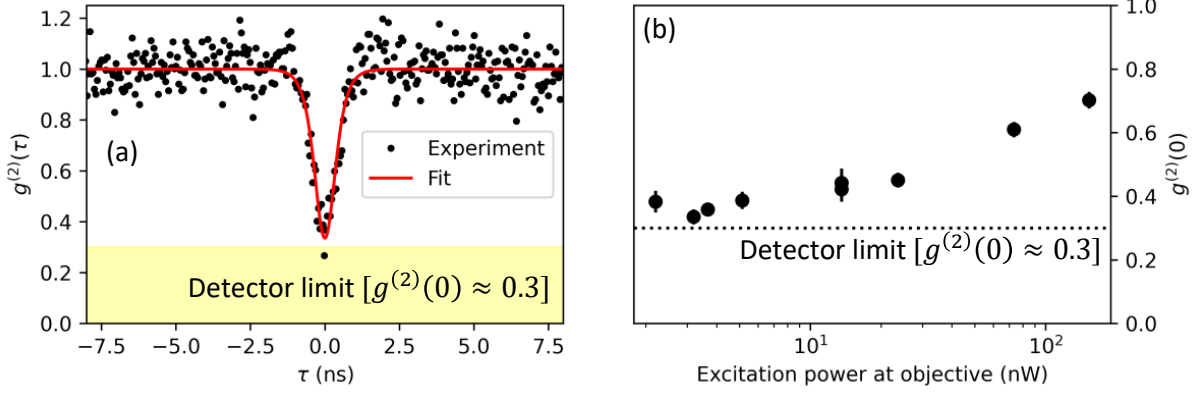


Figure 2.7: Second-order correlation function measured by continuous-wave excitation of a singly-charged QD. (a) Two-photon correlations $g^{(2)}(\tau)$ measured as a function of delay time τ between coincidence clicks. At low excitation power (3 nW) and $\tau = 0$, we observe anti-bunching dip with $g^{(2)}(0) = 0.34 \pm 0.2$. (b) Dependency of $g^{(2)}(0)$ on excitation power.

correlation function $g^{(2)}(\tau)$ with Hanbury-Brown & Twiss (HBT) experiment, where RF is split by a fiber splitter connected to two single-photon detectors registering photon clicks with detection delay τ . Figure 2.7(a) shows the normalized $g^{(2)}(\tau)$ measured with a continuous stream of photons. The correlation function shows a dip at time delay $\tau = 0$ with the raw value of $g^{(2)}(0) = 0.34 \pm 0.02$, a clear signature of a single-photon source. However, because the two-detector jitter of 532 ps is of the same order as the Purcell-enhanced QD emission, the measured dip does not reach $g^{(2)}(0) = 0$ of perfect single-photon source, but its minimum is limited to $g^{(2)}(0) \approx 0.3$. We compare the measured photon correlations with the theoretical curve expected for a perfect single-photon source convolved with the Gaussian instrument response function [18].

Figure 2.7(b) shows $g^{(2)}(0)$ extracted from the experiment as a function of excitation power. In principle, if the detection polarizer could block all residual laser light, a perfectly pure single-photon stream independent of the excitation power (if well below saturation) is expected. However, in our experiments, we achieve polarization extinction around 4×10^6 and a single-photon contrast, i.e., the signal of QD compared to the background, of only about 30. Therefore, with increasing excitation power, the fraction of unblocked laser light contaminating our single photon stream is increasing. This results in lower single-photon purity measured as $1 - g^{(2)}(0)$.

3 Cross-polarization extinction enhancement and spin-orbit coupling of light for quantum-dot cavity-QED spectroscopy

Resonant laser spectroscopy is essential for the characterization, operation, and manipulation of single quantum systems such as semiconductor quantum dots. The separation of the weak resonance fluorescence from the excitation laser is key for high-quality single- and entangled photon sources. This is often achieved by cross-polarization laser extinction, which is limited by the quality of the optical elements. Recently, it was discovered that Fresnel-reflection birefringence in combination with single-mode filtering counteracting spin-orbit coupling effects enables a three-order of magnitude improvement of polarization extinction [PRX 11, 021007 (2021)]. Here, we demonstrate this method for cross-polarization extinction enhancement in cryogenic confocal microscopy of a resonantly excited semiconductor quantum dot in a birefringent optical micro cavity, and observe a $10\times$ improvement of the single-photon contrast.

This chapter is based on: P. Steindl, J.A. Frey, J. Norman, J.E. Bowers, D. Bouwmeester, W. Löffler, *Cross-polarization extinction enhancement and spin-orbit coupling of light for quantum-dot cavity-QED spectroscopy*, arXiv:2302.05359 (submitted) [101].

3.1 Introduction

Highly pure and indistinguishable single-photon sources [13,15,18,28,57,102,103] and spin manipulation [104] often rely on resonant excitation schemes and require a high degree of polarization extinction of the excitation laser. Such experiments are typically carried out in confocal microscope setups having the required high spatial resolution [105,106] to address individual quantum emitters, where the excitation beam is directed onto the sample using mirrors and beam splitters. Because all-dielectric (but also metallic) polarization-preserving mirrors [107] do not exist, usually, linearly polarized light with s or p polarization is used, which, due to symmetry and in the plane-wave approximation, is preserved under reflection. Therefore, the maximal polarization extinction ratios (PER) are limited by the quality of available polarizers to typically $10^5 - 10^6$. Now, experimentally, extinction ratios of up to 10^8 [54] have been observed, but the precise origin of this high ratio has only recently been clearly identified. Benelajla et al. [55] found a 3-orders of magnitude PER improvement by mirror-induced pre-compensation of the residual ellipticity of linear polarizers, in combination with single-mode filtering that eliminates detrimental effects caused by spin-orbit coupling at optical reflection [108–110].

Spin-orbit coupling of light leads to angular and spatial beam shift corrections to specular reflection [111,112], known as Goos–Hänchen [113] and Imbert–Fedorov shifts [114,115]. The latter effect is also referred to as the optical spin-Hall effect of light [116,117]. Here, both of the elliptical eigenpolarizations [118] experience a small opposite transverse shift which leads to a variation in the degree of the circular polarization over the beam cross-section [119]. Measuring in linear cross-polarization, the unwanted (leaked) polarization component of the beam adopts a Hermit-Gaussian profile [55,120,121] with a nodal line in the center, caused by linear polarization projection of the two reflected and shifted beams with opposite helicity. In combination with single-mode fiber detection, Benelajla et al. [55] demonstrated above three orders extinction enhancement after a single optical reflection compared to the bare or conventional polarizer extinction ratio with 90° between the polarizers. This shows a new - only used serendipitously before - application of beam-shifts in addition to high-resolution sensing [122,123] and corrections in astrophysical instruments [124], but the effect has not been clearly identified in confocal microscopy.

Here, we first demonstrate that the elimination of residual scattering from a Glan-type polarizer by propagation or single-mode fiber filtering already enables extinction ratios beyond 10^7 , then we investigate the effect of multiple in-plane reflections (under 45° angle of incidence) on the PER. We find that a single Fresnel reflection is optimal, achieving a PER of nearly 10^8 . Finally, we demonstrate the PER enhancement effect by reflection in a cryogenic confocal microscope. By careful characterization and optimization of the polarizer rotation angles, we achieve extinction ratios up to 10^7 , two orders above the bare polarizer limit, and can clearly attribute this effect to ellipticity and spin-orbit coupling compensation. With this, we demonstrate an improvement of a quantum-dot cavity-QED-based single-photon source.

3.2 Scattering elimination

We start with a simple optical setup shown in the insets of Fig. 3.1. A narrow-linewidth continuous-wave laser with wavelength $\lambda = 935.5$ nm is attenuated with a calibrated set of neutral density filters, mode-filtered with a polarization-maintaining single-mode fiber (PMF) and collimated by an aspheric lens into a Gaussian beam with 0.75 mm beam waist. It is sent to the two polarizers P1 (which is approximately aligned to the incident-light polarization) and P2, which are here two anti-reflection coated calcite Glan-Thompson polarizers, placed 15 cm from each other and mounted in motorized rotation stages with 10^{-2} and 10^{-3} degree resolution, respectively. To analyze the polarizer extinction, the light transmitted through both polarizers is focussed with a lens onto a femtowatt photoreceiver (FWR) that is placed at an adjustable distance d from the analyzer P2, see Fig. 3.1(c). To subtract background light, we use laser modulation and a lock-in amplifier. We determine the polarization extinction ratio $\text{PER} = I_{\text{copol}}/I_{\text{xpol}}$ from the co- and cross-polarized transmitted intensities I_{copol} and I_{xpol} . The front polarizer is kept at a fixed angle β aligned roughly to the polarization of the laser source and I_{xpol} is minimized by rotation of P2.

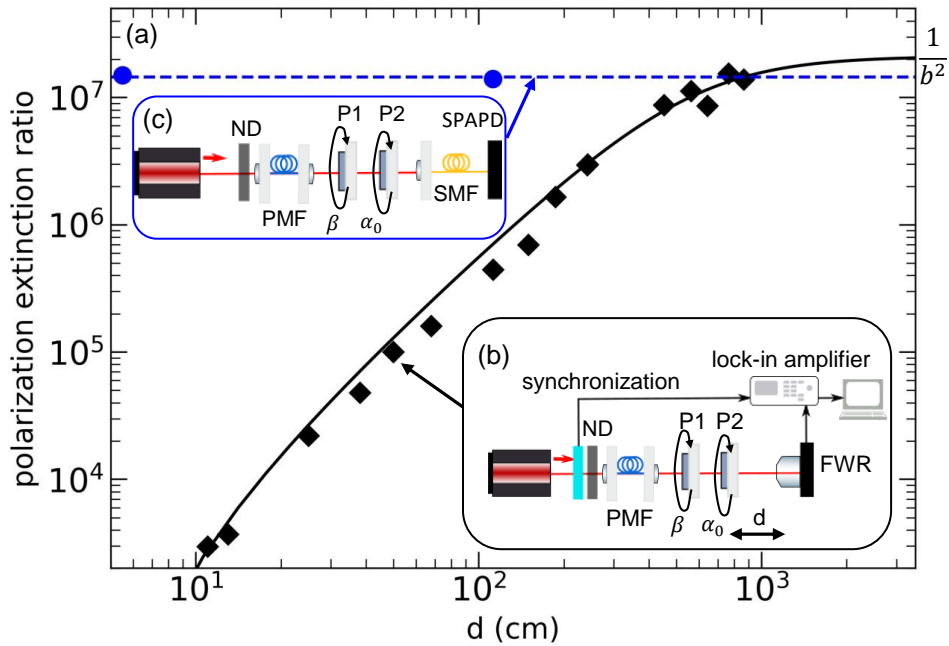


Figure 3.1: The effect of scattered light on the cross-polarization extinction ratio. (a) black symbols: free-space detected PER for increasing detector distance d from the analyzing polarizer, the experimental configuration is sketched in (b). blue: extinction measured using single-mode fiber filtering, (c) shows the setup. The black curve is a model fit as described in the main text.

We measure PER for various distances d up to 8.5 m, collecting in all cases over 90 % of the beam area. The data presented in Fig. 3.1(a) shows a gradual increase of the measured PER with distance, ranging from 10^3 at few centimeter distances to 1.4×10^7 at 8.5 m. Our observed dependency on distance can be explained by scattering including Rayleigh scattering [125]: We model the unwanted light in cross-polarization by (i) residual ellipticity of the polarizers [126] that is limiting the bare extinction ratio to $1/b^2$ [55],

and (ii) (Rayleigh) scattered light, which is quadratically decreasing with distance [127], resulting in $I_{\text{xpolar}} = b^2 + b_{\text{scat}}^2/d^2$. We fit our data and obtain $b = (2.1 \pm 0.2) \times 10^{-4}$ and $b_{\text{scat}} = (12.6 \pm 1.2) \times 10^{-5} \text{ m}^{-1}$, limiting the bare extinction measured after scattering elimination to 2.1×10^7 . This value is very close to the extinction of 1.4×10^7 that we achieve by single-mode fiber (SMF) filtering shown in Fig. 3.1(c). We repeat the SMF-filtered experiment at two distances from P2, including at $d = 4.5 \text{ cm}$ where scattering is dominant without fiber filtering, and observe a constant PER. As expected, a single-mode fiber efficiently removes scattered light.

We operate our photodetector close to the dark current limit, and the signal fluctuated by 5% for the highest PERs. Therefore we repeated the experiments with fiber filtering with a fiber-coupled single-photon avalanche photon detector (SPAPD, 25 % detection efficiency, 200 s^{-1} dark count rate), where the measured PER is limited by dark counts to 6×10^{11} . We obtain a polarization extinction of 1.5×10^7 , confirming our previous results. This is more than two orders of magnitude higher than specified. We have also repeated the same experiment with different pairs of the Glan-Thompson polarizers and always found extinction ratios above 10^7 . This agrees to earlier studies [125, 126], only surpassed by dedicated studies using 10^{-4} degree resolution rotation stages, resulting in extinction ratios up to $\sim 3 \times 10^9$ [128–130]. In the Appendix 3.6.1, we present additional measurements for various analyzers, and show the effect of the anti-reflection coating of Glan-Thompson polarizers, and compare Glan-Thompson polarizers with nanoparticle polarizers.

3.3 Vector-beam effects upon multiple reflections

Now we investigate the influence of (multiple) in-plane reflections on the achievable polarization extinction ratio using experimental setups with 0, 1, and 2 reflections between the polarizers, as shown schematically in panels (a)–(c) of Fig. 3.2. All mirrors are dielectric thin-film mirrors placed approximately under 45° of incidence, and the last mirror in combination with a translation of the fiber collimation lens is used to optimize coupling into the single-mode fiber, where we achieve a coupling efficiency of 80 % in all cases. The single-mode fiber removes scattered light as investigated in the previous section. The initial beam is approximately s -polarized by P1, both P1 and P2 are Glan-Thompson polarizers. We show similar results for p polarization in the Appendix, Sec. 3.6.2. For each configuration, the polarizer angles α and β are fine-adjusted iteratively around the conventional cross-polarization condition ($|\alpha_0 - \beta| = \pi/2$) to optimize the PER. Note that even a small deviation of about 0.03° from the optimal settings of P1 leads to a reduction of PER by one order of magnitude.

First, we discuss the single-reflection case as shown in Fig. 3.2(b), where we reliably reach an extinction ratio of 6.2×10^7 . This extinction ratio is by a factor 3 higher compared to the zero-reflection configuration shown in Fig. 3.2(a). The enhancement is due to compensation of the residual polarizer ellipticities by the small Fresnel-reflection birefringence if the light incident on the mirror is not exactly s or p polarized; and possibly a stress-induced birefringence of the mirror coating. In any case, this birefringence enables for compensation of residual ellipticities of the used polarizers and thus improves the PER [55] compared to the zero-reflection case. As mentioned by Benelajla et al. [55], this can be explained in the plane-wave picture because vector-beam effects and spin-orbit coupling results in higher-order modes, in our case mainly in the first-order Hermite-Gaussian mode [55, 121, 131, 132]. This mode has a nodal line in the center and is shown

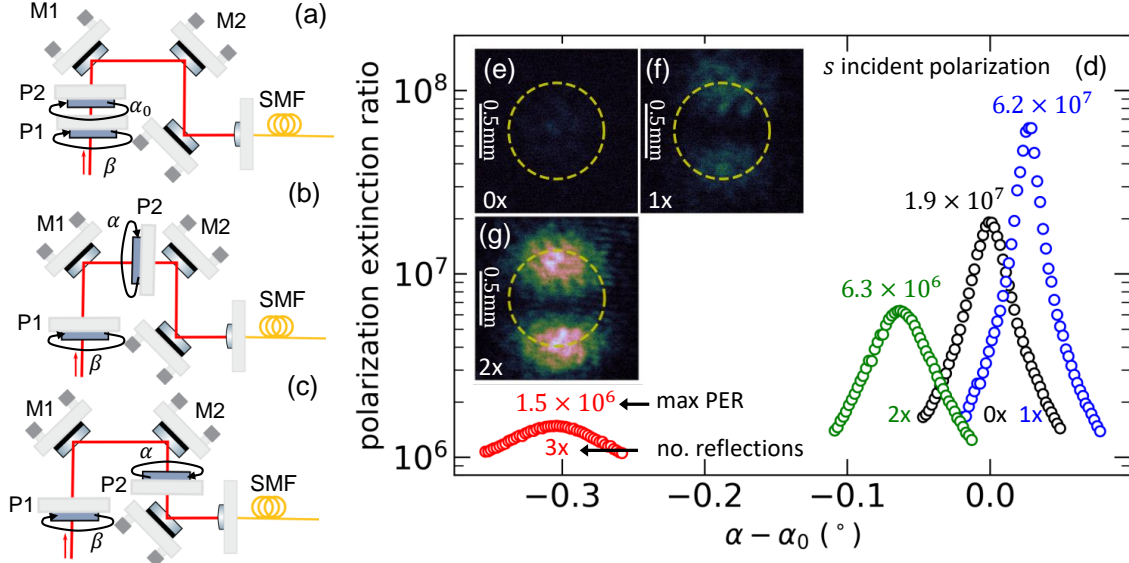


Figure 3.2: Polarization extinction and spin-orbit coupling upon multiple reflections. We use a series of setups with a different number of optical reflections between the polarizers (a-c), determine the maximum achievable polarization extinction (d), and also show the residual unwanted light pattern measured in cross-polarization before coupling into the single-mode fiber (e-g, the dashed circle shows the fiber mode before the collimation lens). In (d), the PER as a function of the analyzing polarizer angle α relative to the conventional cross-polarization angle $\alpha_0 = \beta \pm \pi/2$ is shown. The maximal PER for each configuration with n reflections is indicated.

in Fig. 3.2(f), and it can largely be filtered out by the detection single-mode fiber and does therefore not degrade much the PER.

To further investigate this argument, we have also tested two [Fig. 3.2(c)] and three reflections, each time optimized the polarizer angles, and we observe a reduced PER compared to a single reflection, 6×10^6 after two reflections and 1×10^6 after three reflections. We also observe an increase of the intensity in the first-order Hermite-Gauss mode as shown in Fig. 3.2(g), suggesting that imperfect single-mode filtering can explain the reduction of the PER for multiple reflections.

3.4 Single emitter polarization extinction improvement

Now we investigate whether the method to improve the polarization extinction ratio can also be applied in more complex experimental setups, for which we investigate resonant optical spectroscopy of a single self-assembled InGaAs/GaAs quantum dot (QD) embedded at the antinode of a high-quality micropillar cavity [18,85], using various setups shown in the insets of Fig. 3.3. Instead of the mirror reflection and to independently vary the excitation (P1) and detection polarization (P2), we use a non-polarizing beam splitter (BS) with 90:10 (R:T) splitting ratio to separate excitation and detection paths. The polarization of the excitation narrow-linewidth laser light ($\lambda = 935.5$ nm, FWHM = 200 kHz, beam waist 0.75 mm) is controlled with a Glan-Thompson polarizer mounted in a rotation

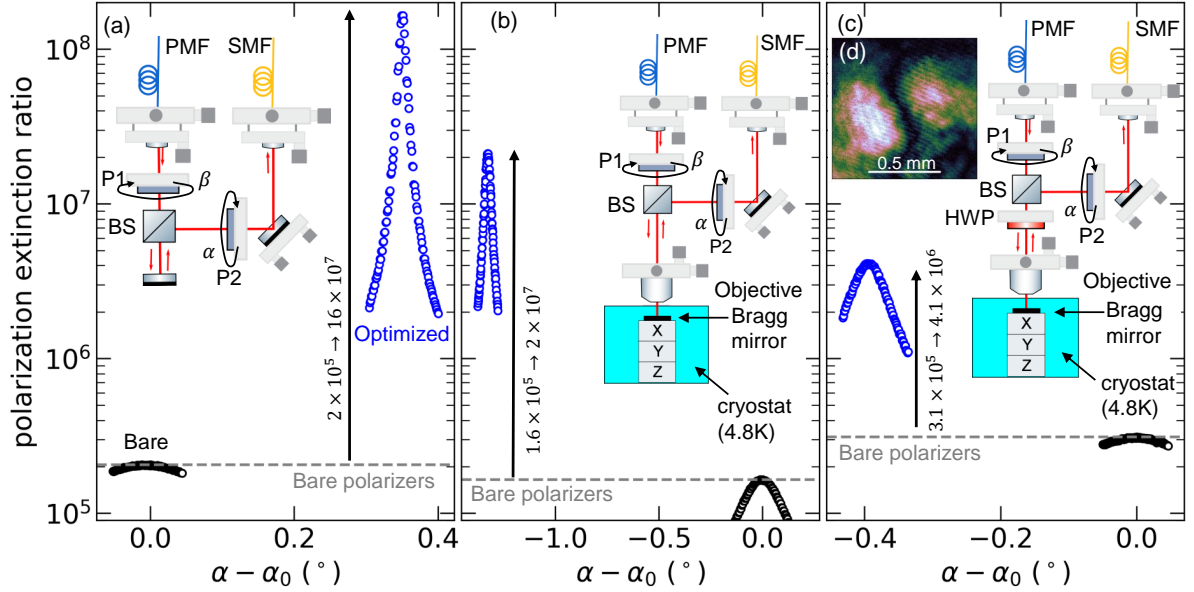


Figure 3.3: Polarization extinction improvement (blue symbols) by reflection in a non-polarizing beam splitter in a cryogenic microscope. Shown is the PER as a function of the angle of the analyzing polarizer α relative to the conventional cross-polarization angle α_0 . First, the case is shown where the cryostat is replaced by a flat mirror, where beyond 10^8 improvement is obtained (a). Then the beam is focussed into the cryostat and reflected there and we obtain beyond 10^7 contrast (b). Finally, the case is shown where a half-wave plate is added before the objective in order to align the linearly polarized cavity modes of the device in the cryostat to the polarization frame of the optical setup (c).

stage with an angular resolution of 0.01 deg. The detection polarization selection is done with a nanoparticle polarizer which is less sensitive to alignment, mounted in a 0.001 deg resolution motorized stage; this polarizer has a bare extinction of 1.9×10^5 . The transmitted light is coupled into a single-mode fiber (coupling efficiency $\sim 85\%$) and detected with a SPAPD.

First, we reflect the incident light from a plane dielectric mirror under normal incidence placed below the beam splitter, as sketched in Fig. 3.3(a). We optimize the PER close to s polarization (at the beam splitter) and obtain a PER of 1.6×10^8 . This is nearly three orders of magnitude higher compared to bare extinction measured with the nanoparticle polarizer in conventional cross-polarization, reproducing our previous results.

Now, we use a long-working-distance plan apochromat objective (0.4 NA, infinity corrected) focussing the light through two silica glass windows into a close-cycle cryostat cooled to 4.8 K. The light is reflected from the top GaAs/AlAs thin-film Bragg mirror of our quantum dot-cavity device. We repeat the optimization of the polarizer angles which are different due to polarization changes caused by the objective and the two silica windows. As shown in Fig. 3.3(b), even in this complex configuration, we reach an extinction ratio of 2×10^7 , a factor 100 above the bare polarization extinction ratio.

Now we perform single-emitter spectroscopy of a single quantum dot in a Fabry-Perot microcavity at around 935.5 nm. The fundamental cavity mode is split by shape and strain induced birefringence [90, 133] by ~ 28 GHz into two orthogonal linearly polarized modes

(V and H). In order to align the polarization frame of reference of the confocal microscope to the frame of the cavity, while avoiding the need to rotate either of them, we use an extra half-waveplate (HWP) below the beam splitter as shown in Fig. 3.3(c). We again optimize the angles of P1 and P2 and reach a PER of 4×10^6 away from the cavity resonances, this is still more than one order of magnitude higher than the bare polarizer extinction ratio. At the same time, as shown in Fig. 3.3(d), we observe in cross-polarization again the typical Hermite-Gauss mode. This suggests that we have demonstrated polarization extinction improvement in a complex cryogenic confocal microscope, despite detrimental effects of the microscope objective and of the focused beam through two cryostat windows, reaching similar extinction ratios as with in-cryostat focussing optics [106].

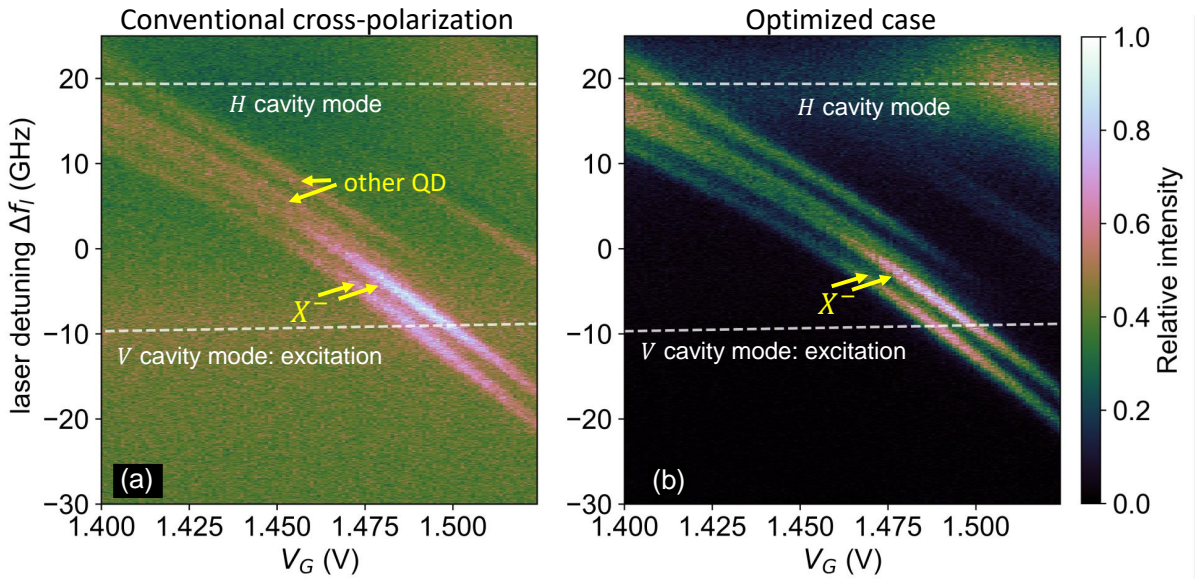


Figure 3.4: Resonant cross-polarized single quantum dot spectroscopy for the conventional cross-polarization configuration (a) and the optimized case (b). Shown is the cross-polarized resonance fluorescence of a negatively charged trion tuned through the cavity resonances by the quantum-confined Stark effect, as a function of laser detuning Δf_l and gate voltage V_G . The incident laser light is polarized along the V cavity axis. Dashed lines indicate both cavity resonance frequencies determined by fits of a semiclassical model [90].

Finally, we demonstrate that the method is also compatible with GHz-scale tuning of the laser, we now show resonant spectroscopy of the negatively charged trion transition X^- of the quantum dot. The dot is embedded in the intrinsic region of a $p-i-n$ diode that allows Stark-shift tuning of the quantum dot resonance through the linearly polarized cavity resonances, see Refs. [90, 133]. Under an in-plane (Voigt geometry) magnetic field of 500 mT we observe in Fig. 3.4 the expected transition doublet [98]; each plot shows the normalized single-photon detection rate acquired under an identical excitation configuration. Compared to the conventional cross-polarization condition shown in Fig. 3.4(a) we see a clear improvement by the optimization polarization condition in Fig. 3.4(b). The ratio of the single photons emitted by the quantum dot to background laser light increases from ~ 2 to ~ 25 - a significant improvement if used as a single-photon source. Note that both the single-photon purity and also indistinguishability [28] benefit from this improved laser extinction. Additionally, the presented technique can be combined with other meth-

ods used for purity and indistinguishability optimization based on spectral filtering [134], non-resonant excitation [17].

3.5 Conclusions

In conclusion, we have clearly identified the polarization extinction improvement effect by optical reflection and spin-orbit coupling of Benelajla et al. [55] in a complex cryogenic confocal microscope setup and obtained more than one order of magnitude improvement of a quantum-dot based single-photon source. We have shown that single-mode fiber detection is important for the reduction of both unwanted scattered light as well as higher-order modes that appear unavoidably by spin-orbit coupling at the mirror or beam splitter. Only with this mode filtering, the polarization extinction ratio enhancement can be described in a plane-wave picture as a reflection-induced birefringence compensation of the residual elliptical polarization of linear polarizers. We have demonstrated that this extinction enhancement has a direct impact on the single-photon contrast in resonant quantum dot spectroscopy, which we have demonstrated with a single quantum dot in a polarization non-degenerate optical micro cavity. To obtain even higher polarization extinction ratios than those reported here (4×10^6), one should rotate the cavity device and remove the half-wave plate since this wave plate most likely also leads to spin-orbit coupling induced modal changes [135] similar to multiple reflections that we have investigated here.

3.6 Appendix

3.6.1 Scattering elimination with various analyzers

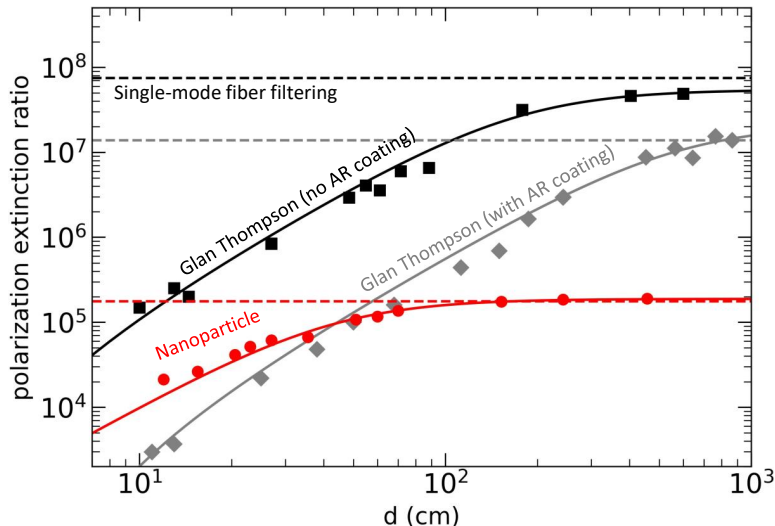


Figure 3.5: Maximum conventional (without mirror reflection) polarization extinction ratio for various analyzer types and conditions: The dashed horizontal lines show the PER using a single-mode fiber, the symbols show the PER using a free-space photo detector at various distances d behind P2. As analyzing polarizer, we used a nanoparticle polarizer (red), and a Glan-Thompson polarizer without (black) and with (gray) anti-reflection coating. Solid lines show the model fit.

In Sec. 3.2 of the main text, we have discussed the importance of the elimination of scattered light for maximal PER. Here we show results (Fig. 3.5) for a wider range of analyzing polarizers P2. We compare Glan-Thompson analyzing polarizers with and without anti-reflection (AR) coating, and a nanoparticle polarizer; the polarizer P1 is an AR-coated Glan-type polarizer in all cases. As in the main text, we model the distance-

Analyzer type	b (10^{-4})	b_{scat} (10^{-4} m^{-1})	Bare extinction $1/b^2$	SMF measured PER
Glan Thompson polarizer (wo AR coating)	1.35 ± 0.03	2.3 ± 0.1	$(5.45 \pm 0.2) \times 10^7$	7.50×10^7
Glan Thompson polarizer (with AR coating)	2.1 ± 0.2	12.6 ± 1.2	$(2.1 \pm 0.3) \times 10^7$	1.38×10^7
Nanoparticle polarizer	23.0 ± 0.3	9.8 ± 0.3	$(1.88 \pm 0.04) \times 10^5$	1.76×10^5

Table 3.1: Fit parameters of the measurements shown in Fig. 3.5.

dependent PER and fit to the data, and we show the fit results of the cross-polarization intensity $I_{\text{xpol}} = b^2 + b_{\text{scat}}^2/d^2$ in Table 3.1. As expected [126], our data shows that AR coating leads to (i) additional scattering captured as an increase in b_{scat} and (ii) extra residual ellipticity of the polarizer reducing the maximal bare extinction. The maximal

bare extinction ratio achieved with the nanoparticle polarizer is strongly reduced, most likely due to residual birefringence of its glass support [126].

3.6.2 Maximal polarization extinction upon multiple reflections

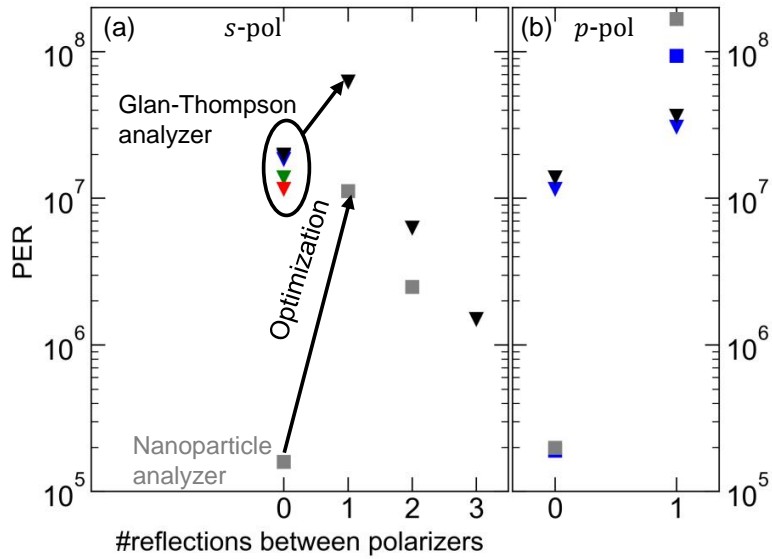


Figure 3.6: Polarization extinction ratio for a different number of reflections for s -polarized (a) and p -polarized (b) incident light, for a Glan-Thompson analyzer (triangles) and a nanoparticle analyzer (squares).

In this section we show additional data for multiple reflections for different polarizer types, and also for s -polarization. As reported by Benelajla et al. [55] and shown in Fig. 3.6, this PER improvement is achieved for both s - and p -polarized light. While the observation of the enhancement is not polarizer-type specific, the absolute value of the maximal PER is a function of the detrimental ellipticity of the polarizers, thus it can vary between individual polarizers.

4 Resonant two-laser spin-state spectroscopy of a negatively charged quantum dot-microcavity system with a cold permanent magnet

A high-efficiency spin-photon interface is an essential piece of quantum hardware necessary for various quantum technologies. Self-assembled InGaAs quantum dots have excellent optical properties, if embedded into an optical micro-cavity they can show near-deterministic spin-photon entanglement and spin readout. In order to address the individual spin states, an external magnetic field is required, which usually is done using a superconducting magnet. Here, we show a compact cryogenically compatible SmCo magnet design that delivers 475 mT in-plane Voigt geometry magnetic field at 5 K, which is suitable to lift the energy degeneracy of the electron spin states and trion transitions of a single InGaAs quantum dot. This quantum dot is embedded in a birefringent high-finesse optical micro-cavity which enables efficient collection of single photons emitted by the quantum dot. We demonstrate spin-state manipulation by addressing the trion transitions with a single and two laser fields. The experimental data agrees well to our model which covers single- and two-laser cross-polarized resonance fluorescence, Purcell enhancement in a birefringent cavity, and variation of the laser powers.

This chapter is based on: P. Steindl, T. van der Ent, H. van der Meer, J.A. Frey, J. Norman, J.E. Bowers, D. Bouwmeester, W. Löffler, *Resonant two-laser spin-state spectroscopy of a negatively charged quantum dot-microcavity system with a cold permanent magnet*, under review, arXiv:2303.02763 (submitted) [136].

4.1 Introduction

An efficient, tunable spin-photon interface that allows high fidelity entanglement of spin qubits with flying qubits, photons, lies at the heart of many building blocks of distributed quantum technologies [137] – ranging from quantum repeaters [138], photonic gates [139, 140], to the generation of photonic cluster states [50,51,53]. Further, to secure connectivity within the quantum network, an ideal spin-photon interface requires near-unity collection efficiency. Therefore an atom or semiconductor quantum dot (QD) carrying a single spin as a quantum memory is integrated into photonic structures such as optical microcavities, where recently 57% in-fiber photon collection efficiency has been achieved [15].

Within the pool of promising systems, singly-charged excitonic complexes of optically active QD devices in III-V materials [43] combine near-unity quantum efficiency, excellent zero-phonon line emission at cryogenic temperatures [141] with nearly lifetime-limited optical linewidth [142]. This, in combination with sub-nanosecond Purcell-enhanced lifetimes, enabled GHz-scale generation rates of indistinguishable single-photons [13–15, 28, 102, 103, 143], robust polarization selection rules [98, 144], and simple on-chip integration facilitating stable-long term operation and tuneability.

The singly-charged QD can be optically excited to the trion state. If this is done with linearly polarized light, the spin state of the resident electron is transferred to the trion hole spin by the optical selection rules. If the trion decays, it will emit a single circularly polarized photon with a helicity depending on the hole spin state, Fig. 4.1(a). To achieve selective spin addressability which is necessary for spin initialization and readout, the QD is typically placed in an external in-plane (Voigt geometry) magnetic field [45, 46], which induces Zeeman splitting of the spin states and trion transitions [98]. The magnetic field modifies the eigenstates of the system and the optical selection rules, and four optical transitions are possible (see Fig. 4.1(b)), which are now linearly polarized. The electron and trion spin, as well as the photon polarization, are now connected by the modified optical selection rules. We obtain two intertwined Λ systems which can be used with steady-state light fields for spin initialization [45, 46], arbitrary spin ground state superposition generation [145], or dynamical spin decoupling from the nuclear bath [146].

Spin manipulation is more difficult if the QD dot is coupled to a polarization non-degenerate birefringent microcavity [15, 85, 143], since the orientation of the in-plane magnetic field needs to be aligned with a cavity polarization axis, and the Purcell enhancement of the QD transitions becomes polarization-dependent. Here we show two-laser resonant spectroscopy [45, 147] of a single spin in a single QD in such a birefringent cavity, and use cross-polarized collection of single photons. We use a simple cryogenic permanent magnet assembly to apply the magnetic field, and we are able to derive the spin dynamics by comparison to a theoretical model.

4.2 Permanent magnet assembly

Magneto-optical quantum dot-based experiments usually rely on large and complex superconducting magnets [53, 99], which generate strong magnetic fields but require both a stabilized current source and cryogenic temperatures. However, many experiments need only a static magnetic field of around 500 mT, which can be achieved with compact strong permanent magnets cooled down together with the QD device [148–150]. Unfortunately, many rare-earth magnetic materials such as NdFeB [151] suffer at cryogenic temperatures from spin reorientation [152] which lowers the effective magnetic field [153] and tilts the

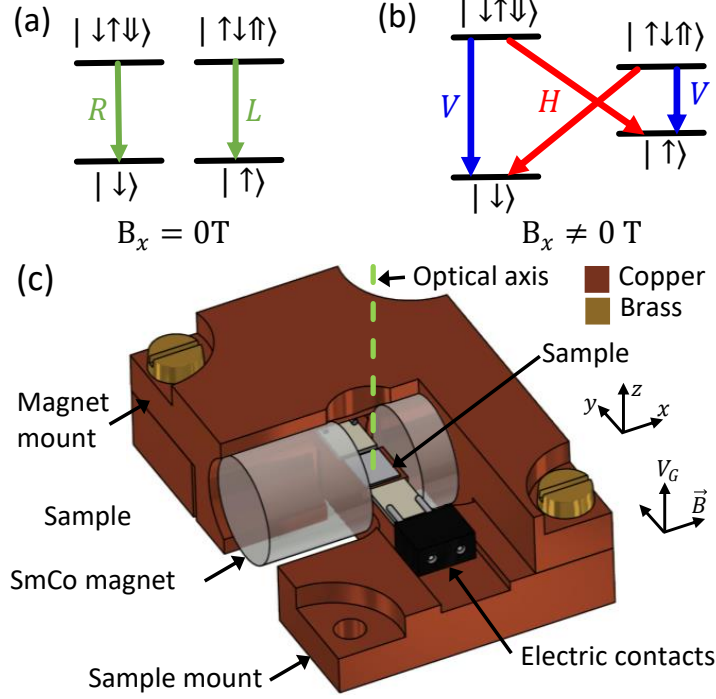


Figure 4.1: Energy level schemes of negatively charged QD and magnetic assembly. Optical selection rules of trion transitions without (a) and with (b) an external in-plane magnetic field. (c) Cut-away schematic of the permanent magnet assembly.

easy axis of the magnetic assembly [151, 154]. Especially, losing control over the magnetic field direction is problematic with quantum dots since it affects mixing between dark and bright states and thus changes both transition energies and optical selection rules [155].

To build our permanent magnet assembly, we have chosen from the strongest commercially available magnetic materials [156, 157] SmCo (grade 2:17) magnets with a room temperature remanence of 1.03 T. This industrially used magnetic system is known for its high Curie temperature (over 800 °C) and high magnetocrystalline anisotropy [158, 159] excellent for high-temperature applications in several fields [160–162]. Especially it is used above the Curie temperatures of NdFeB of 310 °C [159], where current NdFeB-based magnets have relatively poor intrinsic magnetic properties. Moreover, due to low temperature-dependence of remanence and coercivity [157, 163, 164], SmCo-based magnets also show excellent thermal stability of the remanence with near-linear dependence [153, 163] down to 4.2 K. This is in contrast to other common rare-earth magnet compounds such as NdFeB [151], where the remanence at temperatures below 135 K, depending on the specific material composition [153], decreases rapidly by several percent due to the spin-reorientation transition [152].

Our permanent magnet assembly in Fig. 4.1(c) is designed to fit on top of a XYZ piezo motor assembly in a standard closed-cycle cryostat with optical access via an ambient-temperature long working distance objective, which restricts its physical dimensions to approximately 1 cm in height. Thus, we built the assembly from two 9×9 mm commercially available rod-shaped SmCo magnets separated by a 4.5 mm air gap embedded in a $36 \times 24 \times 10.8$ mm copper housing. Due to the large remanence (1.03 T) and small air gap, the assembly in the center of the gap produces a homogeneous magnetic field of about 500 mT, as discussed in Appendix 4.6.1. The assembly is rigidly attached by

brass screws to the H-shaped copper sample mount, where the quantum dot device is horizontally placed in the center of the air gap such that the magnetic field is in-plane (Voigt geometry). The assembly contains electrical contacts to apply a bias voltage V_G to the device. It has a low weight of 69 g (including 4.8 g per magnet), compatible with standard nanopositioners allowing for fine-tuning of the sample position with respect to the optical axis.

The magnetic mount is then cooled down together with the sample to approximately 5 K. Since in SmCo, the spin reorientation transition was reported to be stable down to 10 K [153], we do not expect magnetization axis changes and assume only a small magnetic field drop of 5 % between the room and cryogenic temperatures [151]. This makes SmCo an ideal material choice for strong homogeneous cryogenic magnets, in our case delivering about 475 mT at 5 K.

4.3 Spin-state determination

We study self-assembled InGaAs quantum dots emitting around $\lambda = 935.5$ nm, embedded in $\sim \lambda$ thick GaAs planar cavity, surrounded by two distributed Bragg reflectors (DBR): 26 pairs of $\lambda/4$ thick GaAs/Al_{0.90}Ga_{0.10}As layers from the top and 13 pairs of GaAs/AlAs layers and 16 pairs of GaAs/Al_{0.90}Ga_{0.10}As layers at the bottom [18, 85]. The single QD layer is embedded in a *p-i-n* junction, separated from the electron reservoir by a 31.8 nm thick tunnel barrier including a 21.8 nm thick Al_{0.45}Ga_{0.55}As electron blocking layer designed to allow single electron charging of the QD [91, 92]. A voltage bias V_G applied over the diode allows for charge-control of the ground state of the quantum dot and also to fine-tune the QD transition energies into resonance with the optical cavity mode. The optical in-plane cavity mode confinement is achieved by ion-etching of eight circular trenches arranged in an octagon into the top DBR down to a 10 nm thick AlAs layer. By oxidation of this layer, an intra-cavity lens or aperture is formed, which leads to transverse mode confinement. Details about the device are discussed in Chapter 2. We fabricate 216 cavities per device [61] and select a suitable one with (i) a quantum dot well-coupled to the cavity mode and (ii) low birefringence of the fundamental mode. For the device studied here, the two linearly-polarized modes cavity modes (H and V modes) are split by $\Delta_c = 28$ GHz.

First, we cool down the device to 5 K without the SmCo magnet assembly in a closed-cycle cryostat. For resonant laser spectroscopy, we use a cross-polarization laser extinction method with laser rejection better than 10^6 [101]. Using a free-space polarizer and half-waveplate, the polarization of the excitation laser is aligned along the V cavity polarization axis, and the light reflected from the cavity is recorded with a single-photon detector after passing again the half-wave plate and the crossed polarizer. In Fig. 4.2(a), we show a fluorescence map of this device measured in the cross-polarization scheme as a function of the laser frequency detuning from the V -polarized cavity mode resonance Δf_l and applied bias voltage V_G . We observe a single emission line which is shifted by the quantum-confined Stark effect. The line is in resonance with the V cavity mode at around 1.25 V and with the H cavity mode at around 1.40 V. The same line is visible also if the excitation and detection polarization are swapped, see the cross-sectional plot in Fig. 4.2(c). The fact that we observe the same single line under both perpendicular polarizations and that it is coupled to both fundamental cavity modes, suggests that the emitted photons are circularly polarized and originate from the charged exciton X^- .

Now we cool down the device with the SmCo magnet assembly, to lift the energy

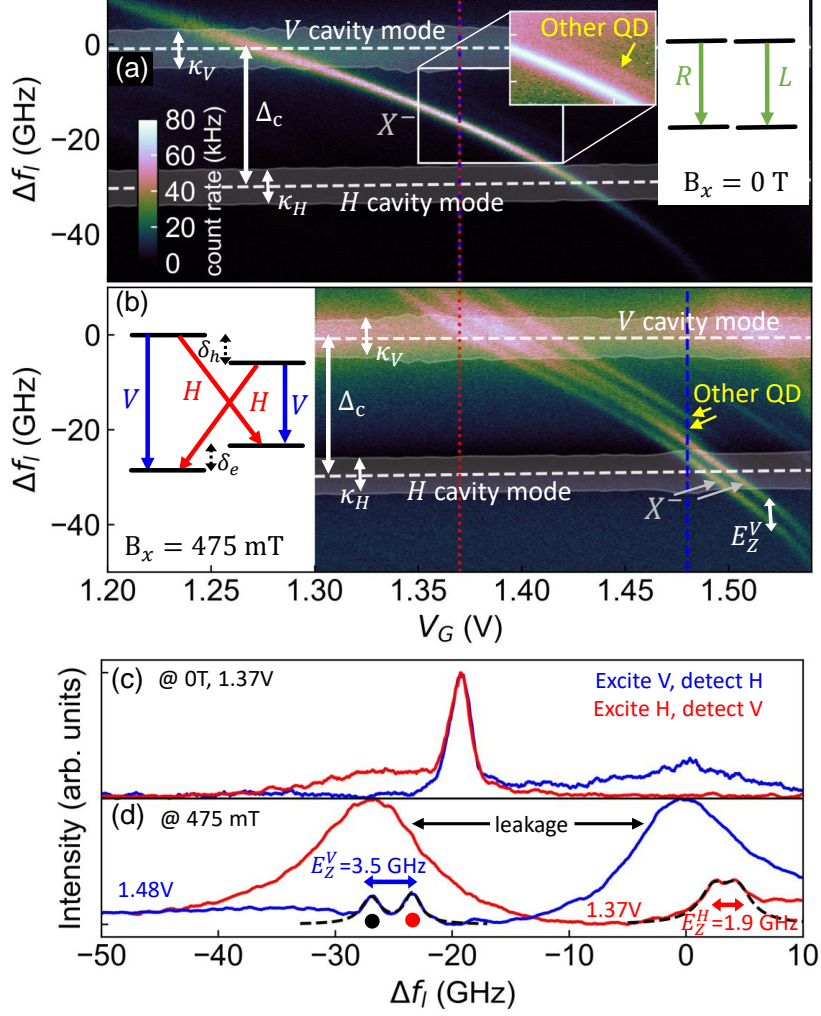


Figure 4.2: Resonant reflection as a function of laser frequency and gate voltage without (a) and with (b) an in-plane external magnetic field, plotted with the same color scale. The excitation laser is polarized along the V cavity axis and reflected laser light is filtered out using a crossed H polarizer, to select photons emitted by the QD trion. Insets show the corresponding optical selection rules. Dashed lines indicate the cavity resonance frequencies, and the cavity linewidth given by the decay rates κ_V , κ_H are shown highlighted; both are determined by semi-classical model fits [90]. The data in the inset of panel (a) are plotted on a logarithmic scale. Panels (c, d) show cross-sectional plots without and with magnetic field for two excitation polarizations (blue: excitation along V cavity mode, red: H) at voltages 1.37 V or 1.48 V, indicated by the vertical lines in panels (a, b). The Zeeman splittings determined from Lorentzian fits (black dashed lines) are given. The excitation power in front of excitation objective is 2 nW, laser scanning speed 41 GHz/s.

degeneracy of the trion transitions. In this scenario, with the energy level scheme in Fig. 4.2(b), the optical selection rules are modified by the in-plane magnetic field from circular to linear polarization. Thus the scanning excitation laser polarized along the V cavity mode can only resonantly address V -polarized transitions, i.e., $|\downarrow\rangle \rightarrow |\downarrow\uparrow\downarrow\rangle$ and $|\uparrow\rangle \rightarrow |\uparrow\downarrow\uparrow\rangle$, therefore we expect to observe a pair of lines Zeeman-split by the energy

$E_Z^V = \delta_e + \delta_h$. Without cavity enhancement, each of the excited trion states radiatively decays with equal probability (by cavity Purcell enhancement, however, this is modified) into the single-spin ground state by emission of a single photon with either V or H polarization depending on the excited and ground states, as depicted in Fig. 4.2(b). Because we measure in cross-polarization, we filter out the emitted V -polarized single photons and detect only photons emitted by the $|\downarrow\uparrow\downarrow\rangle \rightarrow |\uparrow\rangle$ and $|\uparrow\downarrow\uparrow\rangle \rightarrow |\downarrow\rangle$ transitions. Thus, the total detected rate is reduced to half of that without magnetic field. Similarly, the scanning laser polarized along the H cavity mode excites only $|\uparrow\rangle \rightarrow |\downarrow\uparrow\downarrow\rangle$ and $|\downarrow\rangle \rightarrow |\uparrow\downarrow\uparrow\rangle$, and we observe again a pair of fluorescence lines, this time Zeeman split by $E_Z^H = |\delta_e - \delta_h|$. Note that in Fig. 4.2(b) we observe two pairs of emission lines which originate from two different QDs. We focus only on the brighter QD, corresponding to the clear transition in Fig. 4.2(a). In agreement with the trion energy level scheme, the trion transitions exhibit a different Zeeman splitting of $E_Z^V = 3.5 \pm 0.1$ GHz under V - and $E_Z^H = 1.9 \pm 0.1$ GHz H -polarization excitation. This Zeeman splitting was extracted by Lorentzian fits (linewidth ~ 1.5 GHz) to the laser frequency scans shown in Fig. 4.2(d), which allows us to estimate [165] the electron and hole g-factors. We obtain $|g_e| = 0.39$ and $|g_h| = 0.12$; these values agree to literature values for small InGaAs QDs [166]. We also observe a 25 GHz average energy shift of the QD emission caused by a combination of the diamagnetic shift (around 0.5 GHz assuming a diamagnetic constant of $-9.4 \mu\text{eV}/T^2$ [147]), and temperature/strain induced band-gap changes between consecutive cooldowns. These changes are likely also responsible for the brightness change of the second QD, which has been only hardly visible in Fig. 4.2(a). Note that we also observe a broad emission, which is most likely due to non-resonant cavity-enhanced QD transitions [167, 168] in combination with imperfect polarization alignment and/or filtering [101].

4.4 Two-color resonant laser excitation

Now, we demonstrate spin-state manipulation using two individually tunable narrow-linewidth lasers. For a high-degree cross-polarization extinction ratio, we perform resonance fluorescence spectroscopy in the vicinity of the H -cavity mode ($V_G = 1.49$ V). We use V polarization of both excitation lasers to solely address the transitions marked by dots in Fig. 4.2(d). These transitions show Zeeman splitting larger than the QD linewidth leading to frequency-labeling of the spin states, which we use to address the spin states.

In Fig. 4.3(d), we show a reflection map measured in cross-polarization as a function of both laser frequencies f_l (pump) and f_r (repump). The horizontal and vertical lines indicate the trion transition frequencies. Where these frequencies intersect interesting dynamics occurs. First, the nodes oriented along the diagonal represent a condition where both lasers are resonant with the same transition corresponding to the excitation scheme depicted in Fig. 4.3(b). We will call this configuration two-laser resonant excitation (2LRE). The system dynamics under this excitation is equivalent to single-laser excitation (1LRE) with stronger emission due to the higher driving power of $P_l + P_r$. The anti-diagonally oriented nodes correspond to emission under two-color excitation where each laser pumps a distinct transition [Fig. 4.3(c)]; we refer to this scheme as two-color resonant excitation (2CRE) [147]. For clarity, we further focus only on the situation where the first laser of constant power P_l continuously pumps the $|\downarrow\rangle \rightarrow |\downarrow\uparrow\downarrow\rangle$ transition. Due to cross-polarization detection, we observe only H -polarized emission from the $|\downarrow\uparrow\downarrow\rangle \rightarrow |\uparrow\rangle$ transition, a signature of population shelving into the $|\downarrow\rangle$ spin state. This shelved population is repumped, and thus, the total (detected) single-photon rate increased by

re-pumping the $|\uparrow\rangle \rightarrow |\uparrow\downarrow\uparrow\rangle$ transition with the second laser, and we observe a higher photon rate at the anti-diagonal nodes in Fig. 4.3(d).

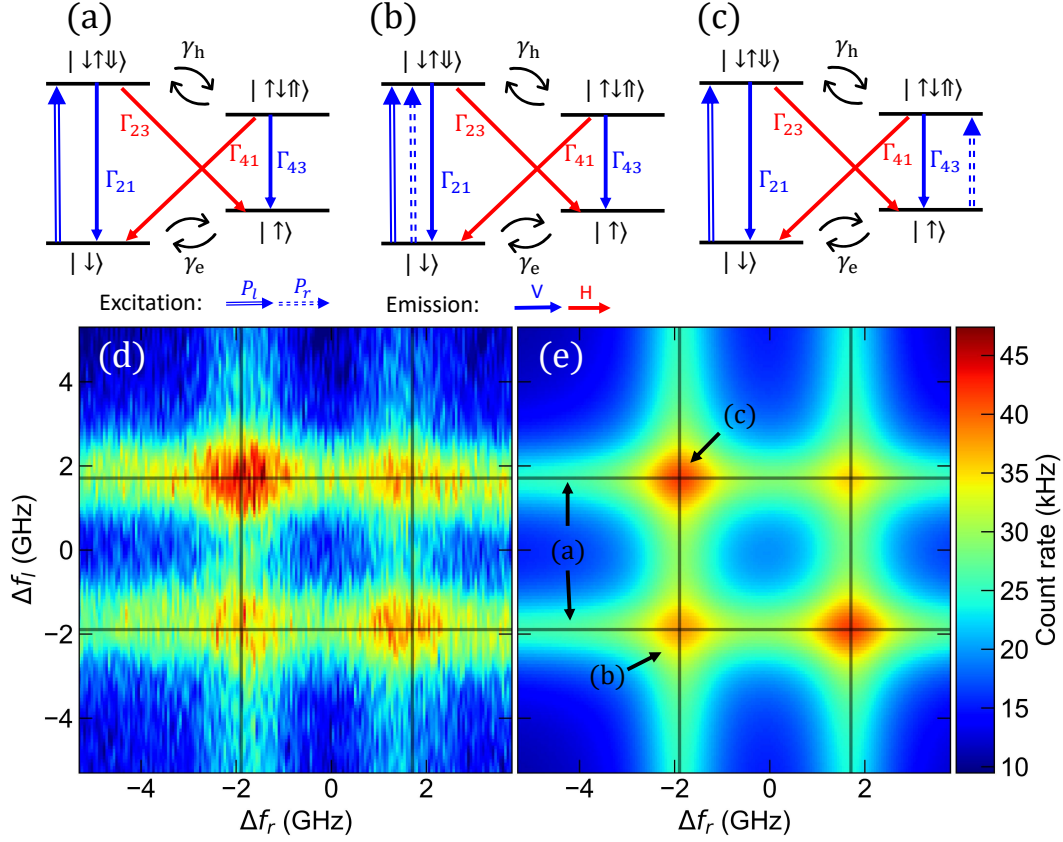


Figure 4.3: Two-color laser trion spectroscopy with a magnetic field in Voigt geometry. (a-c) Comparison of three different trion excitation conditions: single-laser excitation (a), two same-frequency lasers (b), and (c) each laser addresses different trion transitions. Experiment (d) and model (e) data for of two-color experiments, for $P_l = 2.1$ nW pump laser power and $P_r = 2.0$ nW repump laser power, the black lines indicate the QD trion transition frequencies.

To gain a more precise knowledge of the magnitude of the spontaneous decay rates Γ_{xy} as well as electron and hole spin-flip rates γ_e and γ_h involved in the system dynamics, we compare our experiments to a model which is derived in the Appendix 4.6.4. For a laser power below the saturation power P_c , the model is derived from the rate equations describing the steady-state two-scanning lasers pump of the trion energy scheme in Fig. 4.3. The trion transitions are modeled as two coupled Λ systems with asymmetric V and H -polarized radiative transition rates due to cavity enhancement of the latter. A careful analysis of the model parameters and comparison to our experimental results allows us to determine the electron spin-flip rates to be $\gamma_e \approx 2.5$ MHz, while the hole spin-flip rate cannot be determined because of the short lifetime of the excited trion states, as expected. Further we obtain lifetimes of $\Gamma_{21} = 2.1$ GHz, $\Gamma_{43} = 2.7$ GHz, and $\Gamma_{23} = \Gamma_{41} = 0.8$ GHz. Similar spin-flip rates were reported in earlier resonant two-color trion spectroscopy without cavity [147]; the cavity-enhanced radiative rates Γ_{21} , Γ_{43} agree with our power-broadening analysis where we expect a relaxation rate of about 3 GHz for a spectral width of 1.5 GHz, see Appendix 4.6.3. Note, the cavity-enhanced rates Γ_{21}

and Γ_{43} are different due to different Purcell enhancement of the transitions, while the non-enhanced rates Γ_{23}, Γ_{41} are identical, as expected [98, 147].

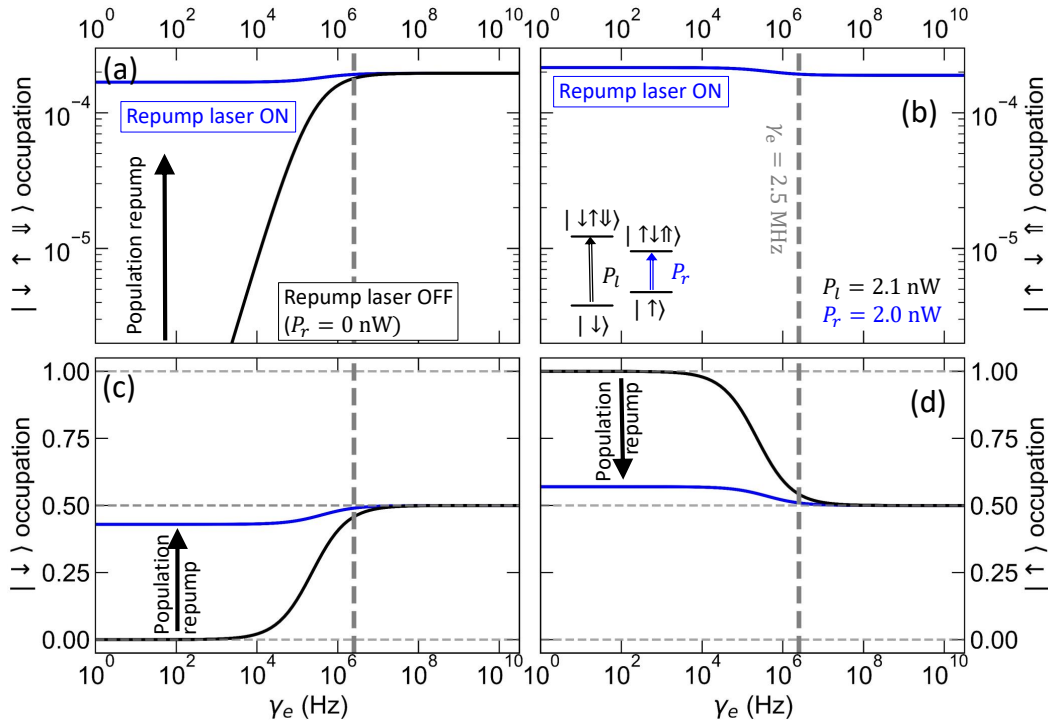


Figure 4.4: Steady-state trion states (a, b) and electron ground-state spin (c, d) occupation probability as a function of electron spin-flip rate, with (blue) and without (black) repump laser. The dashed lines show the determined spin-flip rate of $\gamma_e \approx 2.5$ MHz.

Figure 4.4 shows spin-flip rate dependency of the steady state occupation of the trion and electron spin states predicted by our theory. In the simulation with varied γ_e , we used system parameters found above together with laser powers $P_l = 2.1$ nW and $P_r = 2.0$ nW to demonstrate spin pumping. First, if the electron spin-flip rate is small (below 1 kHz), the weak pump laser pumping the transition $|\downarrow\rangle \rightarrow |\downarrow\uparrow\downarrow\rangle$ initializes the spin state $|\uparrow\rangle$. By optical repumping with the second laser on resonance with $|\uparrow\rangle \rightarrow |\uparrow\downarrow\uparrow\rangle$, the shelved spin population can be largely transferred from $|\uparrow\rangle$ into $|\downarrow\rangle$ as demonstrated in Fig. 4.4(c,d). Due to the optical repumping, the resonant absorption on spin $|\uparrow\rangle$ becomes again possible, leading experimentally in the recovery of transmission signal at the resonant frequency with $|\downarrow\rangle \rightarrow |\downarrow\uparrow\downarrow\rangle$ [147, 169]. Our simulation for the determined spin-flip rate of $\gamma_e \approx 2.5$ MHz shows that the electron spin-flip leads to a comparable spin population of both ground states even without repumping laser field, making conclusive absorption measurements difficult because of the small change between ground state populations with and without optical repumping. However, the spin repumping from $|\uparrow\rangle$ is accompanied by the population of $|\uparrow\downarrow\uparrow\rangle$ resulting in extra emission from this spin state. Importantly, the presence of this extra emission is independent of the ground state spin-flip rate and can be thus used as a signature of optical spin repumping. Moreover, at low γ_e , the emission following the spin repumping benefits also from the extra excited state population of the state $|\downarrow\uparrow\downarrow\rangle$, see Fig. 4.4(a).

Finally, we test our model against a series of excitation-power-dependent experiments

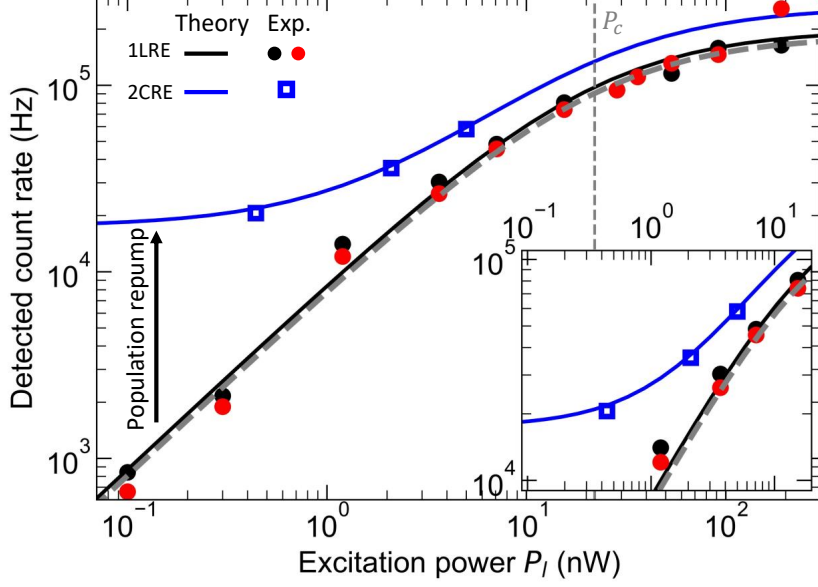


Figure 4.5: Power dependency of the trion resonant fluorescence under different excitation schemes, comparing experimental photon count rates (symbols) to our model (lines) with $\gamma_e = 2.5$ MHz: Only pump laser for both trion transition (1LRE, black and red) and with repump laser (2CRE, blue). The gray dashed lines indicate the standard two-level system saturation behaviour.

shown in Fig. 4.5. Both observed trion transitions under 1LRE (black and red symbols corresponding to lines in Fig. 4.2(d)) show saturation with power described by $180 \text{ kHz}/(1 + P_c/P)$ [18, 170] with a reasonable saturation power of $P_c = 22 \pm 2 \text{ nW}$, in agreement to our model.

In contrast to these single-frequency measurements, the 2CRE scheme shown by the blue symbols in Fig. 4.5 shows clear signs of spin repumping: Due to the continuous repumping of the spin population of both ground states with the two lasers (at a constant $P_r = 2.0 \text{ nW}$), we control the individual steady-state spin populations by altering the relative power of the lasers. Because higher repumping power leads to stronger repumping and thus to higher excited-state occupation, we experimentally observe increased photon rates, following our model predictions. This increase varies with relative powers between pump and repump laser beam from a factor higher than 10 at $P_l = 0.44 \text{ nW}$ to factor 1.3 above P_c .

4.5 Conclusions

We developed a compact cryogenic SmCo permanent magnet assembly delivering an in-plane magnetic field of 475 mT. In contrast to superconducting solenoids, this solution does not need any active control and works from cryogenic to ambient temperatures. Therefore, we believe it could become a preferable, economical, and scalable architecture for spin-photon interfaces where the magnetic field is used in “set-and-forget” mode.

Using this magnetic assembly in Voigt geometry, we have shown Zeeman splitting and spin addressability of the electron and trion states of a negatively charged quantum dot embedded in a birefringent optical microcavity. We demonstrate spin-state manipulation using continuous-wave resonant two-laser spectroscopy, which in combination with a

high-extinction ratio cross-polarization technique enables background-free single-photon readout. This two-laser excitation scheme, similar to earlier schemes [45, 145, 147] without a cavity, will allow for spin-state initialization and manipulation.

4.6 Appendix

4.6.1 Permanent magnet assembly simulations

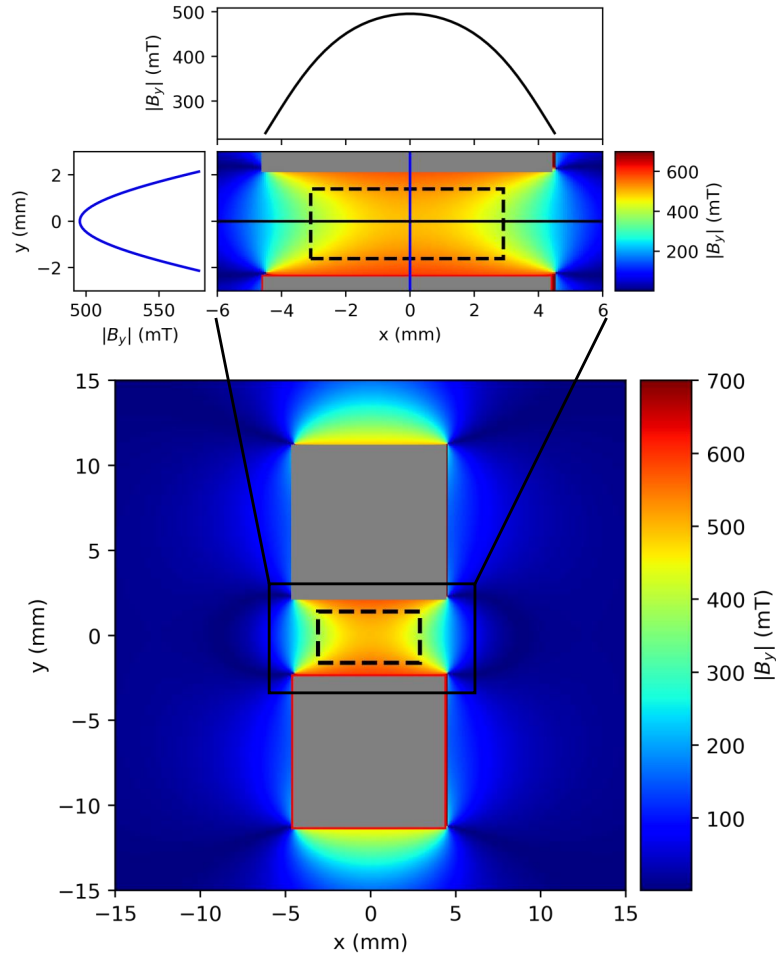


Figure 4.6: Magnetic field simulation of the magnetic assembly with a 4.5 mm air gap at room temperature. The magnitude of the magnetic field strength $|B_y|$ along an xy -cross-section of the assembly (grey regions), with the location of the sample taken to be the origin (outlined by the dashed line). (Inset) Zoom-in $|B_y|$ to the sample region with cross-sections along the x (top) and y (left) direction through the center of the sample.

The magnetic assembly was simulated using Magpylib – a Python package for magnetic field computation [171]. Given the large and thermally stable coercivity of SmCo magnets at cryogenic temperatures [157,164], we model the permanent magnets as 9×9 mm large rods insensitive to any external magnetic field with a residual magnetization of 1.03 T. The copper housing of the magnet was not included in the simulations, because copper is a weak magnetic metal with low magnetic susceptibility [172]. The room temperature simulation of our magnetic mount with a 4.5 mm air gap between the magnetic rods is presented in Fig. 4.6. From the simulation, we see that the assembly produces a strong magnetic field (beyond 500 mT) confined between the poles of the magnets. Due to the simple assembly design, the magnetic field is inhomogeneous over the entire sample footprint of several square millimeters. However, over the few nanometer-size quantum

dot used later in the experiments, the magnetic field can be assumed homogenous. In our experiments, we use QD close to the coordinate origin in Fig. 4.6, where the external magnetic field reaches a strength of 500 mT.

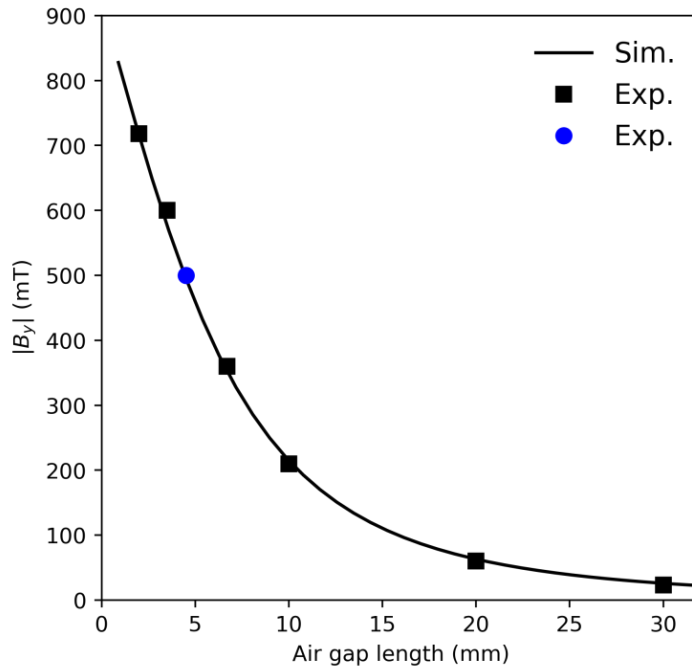


Figure 4.7: Air gap length dependence of magnetic field strength $|B_y|$. The experimental Hall probe data points taken before (black) and after (blue) fixing SmCo magnets into copper mount are compared to at the sample center simulated $|B_y|$ (curve).

The external field can be tuned by the air gap length, as shown in Fig. 4.7. First, before mounting the magnets into the copper housing, we fix a Hall probe to the center of the air gap and vary the gap length. The measured field strengths excellently agree with our simulations for various air gaps. Finally, the rods are glued at the distance of 4.5 mm into the copper housing, and a field of 500 mT in the air gap center is confirmed by Hall probe measurements.

4.6.2 Experimental setup and characterization

For all our resonant fluorescence experiments, we use a confocal microscope [101] sketched in Fig. 4.8. Here, two continuous-wave narrow-linewidth (200 kHz) scanning lasers are fiber coupled to polarization-maintaining fibers (PMF), combined on polarization-maintaining fiber splitter, and launched into the vertical confocal microscope. The laser light is directed on a free space non-polarizing beam splitter (BS, splitting ratio 90:10 with transmission $\eta_{BS,T} = 0.1$) and focused through two silica windows into closed-cycle cryostat with a long-distance working ambient-temperature objective with a total transmission of $\eta_{obj} = 0.62$. The excitation polarization is controlled and aligned along the V cavity mode with a Glan-Thompson polarizer (P1) and zero-order half-waveplate (HWP; @935 nm, quartz, transmission > 0.99), both mounted in finely tunable motorized rotation stages with a resolution of 10 mdeg. The last transmission we need to consider is the fraction of the light transmitted through the top mirror of the cavity. We estimated

this transmission from the distributed Bragg reflector design as $T_{\text{cav}} = 3.4 \times 10^{-4}$ [58]. Then, the measured 21 nW optical excitation power in front of the BS corresponds to an excitation power of 0.44 pW at the location of the QD.

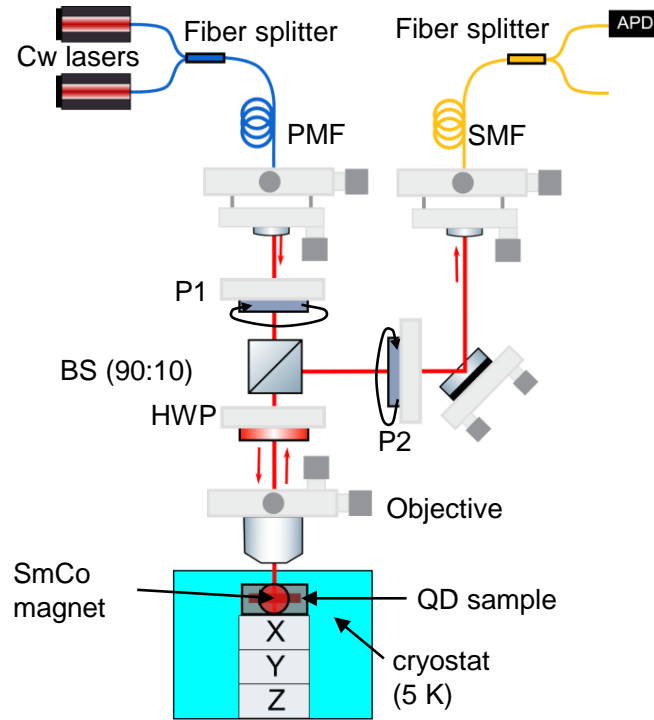


Figure 4.8: Experimental setup.

The photons emitted by the quantum dot and the reflected laser are reflected at the BS with reflectivity $\eta_{\text{BS,R}} = 0.9$. The QD resonant fluorescence is separated from the excitation laser using a cross-polarization scheme, where the excitation laser is rejected by a factor 4×10^6 by using a nanoparticle polarizer (P2; transmission $\eta_{\text{P}} = 0.9$) in a motorized rotation stage with 1 mdeg resolution. Due to the alignment of the magnetic field, we assume that the linearly polarized trion transitions are perfectly aligned with the cavity polarization axes. Thus, the emission from the two transitions with the same polarization as the excitation laser is perfectly filtered out, while emission from the two orthogonal transitions is fully transmitted. The separated emission from the QD is then fiber coupled in a single-mode fiber (SMF; coupling efficiency 0.85, including collimation-lens transmission) and sent through a fiber splitter on a single-photon detector (APD; $\eta = 0.25$). Due to loss in the fiber-splitter, the total free space-to-detector collection efficiency is 0.32. The total transmission through the optical detection system is $\eta_{\text{det}} = 0.32\eta_{\text{obj}}\eta_{\text{BS,R}}\eta_{\text{P}}\eta = 0.04$.

4.6.3 Single-laser resonance fluorescence

The in-plane magnetic field of 475 mT splits the studied trion transition via the Zeeman effect into two pairs of linearly polarized emission lines with mutually orthogonal polarization. We observe a splitting of 3.4 ± 0.1 GHz and 1.8 ± 0.1 GHz between V -polarized and H -polarized transitions, respectively, corresponding to electron and hole g -factors of $|g_{\text{e}}| = 0.39$ and $|g_{\text{h}}| = 0.12$.

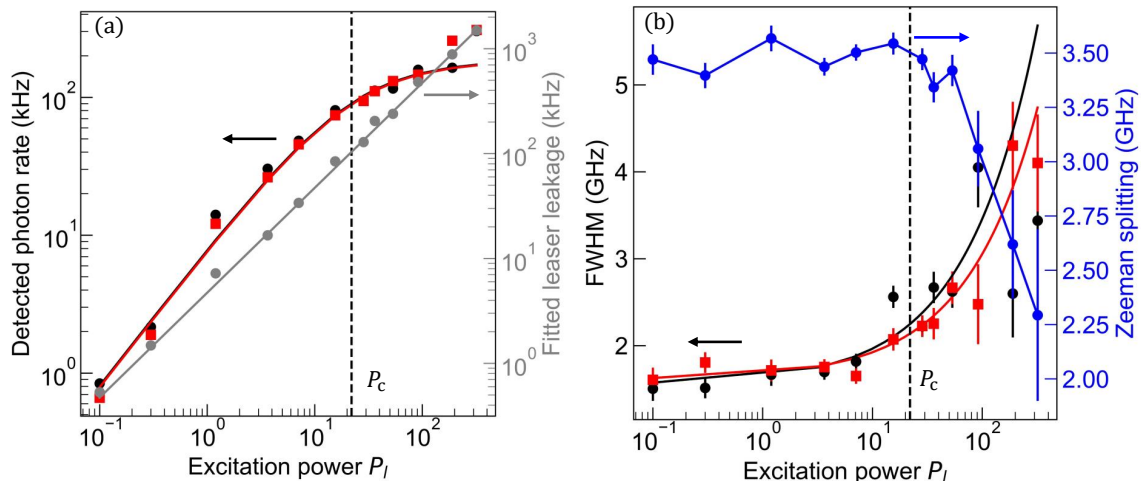


Figure 4.9: Single-laser power dependent characterization. Panel (a) shows how the detected rate of photons from the two trion transitions (black, red) and laser leakage (grey) depends on laser power. Panel (b) shows the power dependence of the full width at half maximum of these two Lorentzian transitions (black, red), and the Zeeman splitting (blue). Error bars show the statistical error of the fit parameters and solid lines show the model fits.

In the main text, we mainly focus on V -polarized resonant excitation with varied excitation power. We observe a constant Zeeman splitting over a bias range of more than 200 mV, therefore we characterize the excitation power properties only for a bias voltage of 1.49 V, a voltage where the transitions are in resonance with the H -polarized cavity mode. The pair of trion emission lines is detected in cross-polarization under V -polarized excitation of varied optical power P_l over three orders in magnitude. We fit the measured resonance fluorescence spectrum with double Lorentzian function with a constant term characterizing an excitation laser leakage due to finite cross-polarization extinction ratio, and present the power dependency of the individual fit parameters in Fig. 4.9. We observe near-identical behavior for the emission lines in both photon rate and line broadening. Figure 4.9(a) shows the detected photon rate, which is well fit by $180 \text{ kHz}/(1+P_c/P_l)$ [170], characterizing the two-level system saturation at power $P_c = 22 \pm 2 \text{ nW}$. Similarly to our previous work [18], we observe a power-linear background (gray), most likely due to imperfect polarization extinction. In Fig. 4.9(b), we analyze excitation-power induced linewidth (FWHM) broadening. The experimental data show a linewidth of $\Gamma = 1.55 \pm 0.1 \text{ GHz}$ at low excitation power, with a significant broadening above P_c . This broadening is well described with a simple power-law model $\Gamma + \beta P_l^{2/3}$ [173, 174], using a parameter $\beta = (77 \pm 10) \times 10^3 \text{ GHz}^{3/2} \text{ W}^{-3/2}$, and can be caused by an increase in the dephasing rate induced by nuclei polarization. The variation of the polarization of the nuclear-spin bath will also affect the eigenenergies, leading to significant changes in Zeeman splitting, as observed in Fig. 4.9(b).

4.6.4 Rate-equation model of resonant two-color spectroscopy of a negatively charged exciton

In this section, we describe our theoretical model used for comparison and understanding of the two-color resonance fluorescence experiments. Limiting the description to continuous-wave (cw) resonant excitation of the trion states in Voigt configuration, we model the trion energy levels as two coupled Λ systems. Figure 4.10 shows a sketch of the interaction, where in total 4 optical transitions in a linear basis are possible: two emitting V -polarized (blue) and two emitting H -polarized photons (red), respectively. In addition to these optical transitions, there are also two spin-flip transitions, one for electron spin γ_e and one for hole spin γ_h .

In the experiment, a strong laser power was used, therefore we can neglect quantization of the excitation light together with stimulated emission, but it was kept at least factor 3 below saturation intensity P_c . Within this limit, we can separate the problem into two steps: (i) setting up and solving rate equations characteristic to individual energy level configurations, and (ii) expression of emitted photon rates based on state populations found from (i).

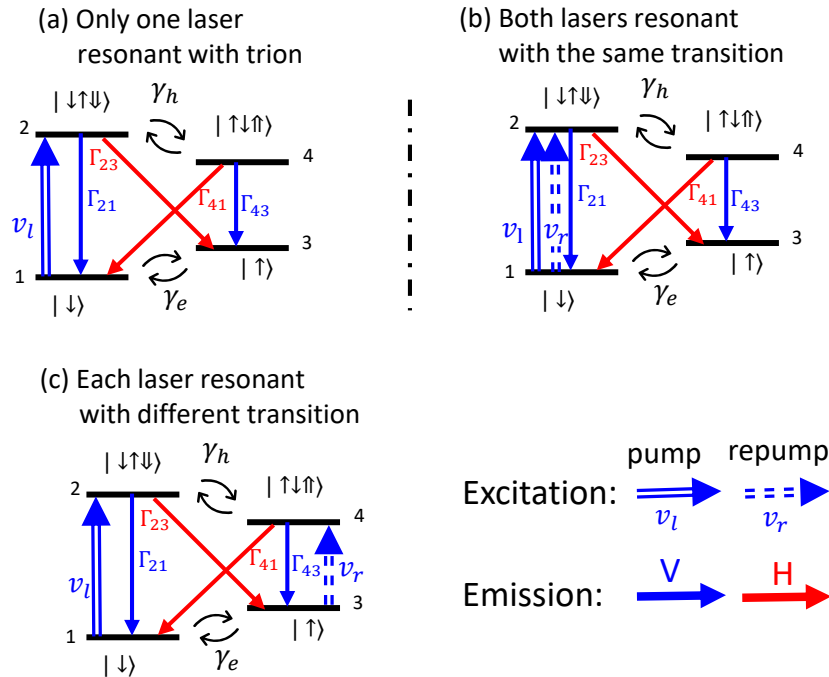


Figure 4.10: Resonant excitation schemes of trion: (a) a single excitation laser is resonant with a trion transition, (b) two lasers of identical polarization are resonant with the same transition, (c) two lasers are resonant with distinct trion transitions.

4.6.4.1 Spin population rate equations

The modeling of the scanning two-color resonant excitation of two coupled Λ systems can be split into three scenarios, depicted in Fig. 4.10, distinguished by which transitions are addressed with the excitation lasers. Additionally, in correspondence to our experiment, the model is developed only for V -polarization, reducing the complexity.

We start with a situation when only a single laser is resonant with the trion energy levels, as depicted in Fig. 4.10(a). For simplicity, we discuss here only resonant excitation of the $|\downarrow\rangle \rightarrow |\downarrow\uparrow\downarrow\rangle$ transition, $|\uparrow\rangle \rightarrow |\uparrow\downarrow\uparrow\rangle$ can be derived easily. Here, the population is brought from the ground state $|\downarrow\rangle$ to the excited state with a single resonant laser of excitation rate v_l . The excited state relaxes back to the $|\downarrow\rangle$ or $|\uparrow\rangle$ spin state by spontaneous emission of a V (emission rate Γ_{21}) and H (emission rate Γ_{23}) polarized single photon, or via a hole spin-flip transition to $|\uparrow\downarrow\uparrow\rangle$. We use the steady-state condition to solve the trion-state population described by the interaction matrix

$$M_{\text{pump}} = \begin{pmatrix} -(v_l + \gamma_e) & \Gamma_{21} & \gamma_e & \Gamma_{41} \\ v_l & -(\Gamma_2 + \gamma_h) & 0 & \gamma_h \\ \gamma_e & \Gamma_{23} & -\gamma_e & \Gamma_{43} \\ 0 & \gamma_h & 0 & -(\Gamma_4 + \gamma_h) \end{pmatrix}$$

and analytically find the state population $P_{|x\rangle}$ for each trion state involved in trion dynamics:

$$P_{|\downarrow\rangle} = \frac{\gamma_e \Gamma_2 \Gamma_4 + \gamma_e \gamma_h (\Gamma_2 + \Gamma_4)}{\alpha(v_l)}, \quad (4.1)$$

$$P_{|\downarrow\uparrow\downarrow\rangle} = \frac{\gamma_e (\Gamma_4 + \gamma_h)}{\alpha(v_l)} v_l, \quad (4.2)$$

$$P_{|\uparrow\rangle} = P_{|\downarrow\rangle} + \frac{\Gamma_{23}}{\gamma_e} P_{|\downarrow\uparrow\downarrow\rangle} + \frac{\Gamma_{43} \gamma_h}{\alpha(v_l)} v_l, \quad (4.3)$$

$$P_{|\uparrow\downarrow\uparrow\rangle} = \frac{\gamma_e \gamma_h}{\alpha(v_l)} v_l. \quad (4.4)$$

Here, we use the total emission rates $\Gamma_2 = \Gamma_{21} + \Gamma_{23}$ and $\Gamma_4 = \Gamma_{41} + \Gamma_{43}$ from excited states $|\downarrow\uparrow\downarrow\rangle$ and $|\uparrow\downarrow\uparrow\rangle$, together with $\alpha(x) = [\Gamma_{43} \gamma_h + \Gamma_{23} (\Gamma_4 + \gamma_h) + \gamma_e \Gamma_4 (2\Gamma_2 + 1) + 2\gamma_e \gamma_h (\Gamma_4 + \Gamma_2 + 1)]x$ to simplify the notation.

Now, we focus on two-laser excitation of the same transition, Fig. 4.10(b). Here, the two lasers have identical frequency and polarization and differ only in optical power, therefore we can model them as a single laser of optical power corresponding to $v_l + v_r$, where v_l and v_r are the excitation rates of pump and repump lasers. Then the state occupations have again form of Eqs. (4.1-4.4), with the only change in the excitation rate $v_l \rightarrow v_l + v_r$.

For the two-color excitation scheme, where each laser is in resonance with a distinct trion transition, as sketched in Fig. 4.10(c). Because the interaction matrix

$$M_{\text{pump\&repump}} = M_{\text{pump}} + \begin{pmatrix} 0 & 0 & 0 & 0 \\ 0 & 0 & 0 & 0 \\ 0 & 0 & -v_r & 0 \\ 0 & 0 & v_r & 0 \end{pmatrix}$$

does not have a steady-state analytical solution, we obtain the state occupations $P_{|x\rangle}$ numerically.

4.6.4.2 2D two-color resonant excitation model

Now we formulate a simple model interconnecting our two-color resonance fluorescence experiment with the steady-state trion occupations derived from the system rate equations. First, we assume that the emitted resonance fluorescence rate is proportional to excited state occupations and the radiative transition rates as

$$I = (f_V \Gamma_{21} + f_H \Gamma_{23}) P_{|\downarrow\uparrow\downarrow\rangle} + (f_V \Gamma_{43} + f_H \Gamma_{41}) P_{|\uparrow\downarrow\uparrow\rangle}.$$

Here we use a parameter f_x where the subscript indicates the emitted photon polarization allowing later implementation of the cross-polarization scheme by setting $f_V = 0$ and $f_H = 1$. We assume that the pair of the observed emission lines is resonantly excited with a laser of frequency f_1^{QD} and f_2^{QD} , and each of the lines has a Lorentzian shape characterized by an identical full width at half maximum Γ , in agreement with our previous experiments in Sec. 4.6.3. Using Γ , f_1^{QD} , and f_2^{QD} from single-laser resonance fluorescence experiments, we model the emission as 2D Lorentzian functions $L(x, x_0, y, y_0, \Gamma) = \frac{2}{\pi\Gamma} [(x - x_0)^2 + (y - y_0)^2 + (\Gamma/2)^2]^{-1}$ multiplied with photon rate I calculated from the rate equations. As discussed above, the rate equations and thus also the state occupations and I varies with specific resonant excitation configuration. The different conditions we label by $I^{(i,j)}$, where i, j indicate with which transitions the lasers are resonant with (f_x^{QD}) or 0 if the laser is not resonant with any trion transition. The final two-laser model is given by

$$\begin{aligned}
I_{\text{total}} = & \sum_{i \in \{1,2\}} I^{(i,0)} L(f_r, f_i^{\text{QD}}, 0, 0, \Gamma) + \sum_{i \in \{1,2\}} I^{(0,i)} L(0, 0, f_l, f_i^{\text{QD}}, \Gamma) \\
& - \sum_{i,j \in \{1,2\}} (I^{(i,0)} + I^{(0,j)}) L(f_r, f_i^{\text{QD}}, f_l, f_j^{\text{QD}}, \Gamma) \\
& + \sum_{i \in \{1,2\}} I^{(i,i)} L(f_r, f_i^{\text{QD}}, f_l, f_i^{\text{QD}}, \Gamma) + \sum_{i,j \in \{1,2\}, i \neq j} I^{(i,j)} L(f_r, f_i^{\text{QD}}, f_l, f_j^{\text{QD}}, \Gamma).
\end{aligned} \tag{4.5}$$

Here, the first two terms describe emission under single-laser excitation with separate lasers, the third term removes contributions of the individual lasers that would be counted twice otherwise. The fourth term accounts for emission by simultaneous two-resonant laser excitation of the identical transition, and the fifth term for concurrent two-color excitation of two distinct transitions.

4.6.4.3 Estimate of excitation and detection rates

To connect the theoretical model with our experiment, we need to estimate the trion driving power from optical power measured in the setup. It requires conversion of an optical power measured with a power meter to the individual laser excitation rates v_l and v_r . First, we determine the setup throughput as described in Sec. 4.6.2. As an example, the optical power is $P = 21$ nW, measured in our setup in front of BS. Using the measured transmission of the excitation path of our setup ($\eta_{\text{ex}} = T_{\text{cav}} \eta_{\text{obj}} \eta_{\text{BS,T}}$), and assuming unity QD quantum efficiency, we estimate that the QD is excited with an optical power corresponding to $\eta_{\text{ex}} P = 0.44$ pW. The excitation rate is then calculated from this power by multiplication with an experimentally determined conversion factor between power-meter readings and the single-photon rate measured with a single-photon detector.

Similarly, we correct the theoretical emission for the detection system optical throughput simply by its multiplication with experimentally determined throughput η_{det} .

4.6.4.4 Model rates estimation

We start the discussion with the radiative rates of our trion-cavity system. An isolated trion in Voigt geometry typically has all four radiative transitions of an identical rate around $\Gamma_0 = 1$ GHz [98]. The situation is different if a trion is coupled into a linearly polarized cavity mode leading to Purcell enhancement. Neglecting pure dephasing, we estimate the cavity-enhanced rates from the QD emission line width Γ of 1.5 GHz, giving $\Gamma_{21} = \Gamma_{43} = 3$ GHz. Assuming that the second pair of rates correspond to an isolated trion, we estimate these rates to be $\Gamma_{23} = \Gamma_{41} = 1$ GHz. Since these rates are very

sensitive to the specific condition, we keep them as free fit parameters for the two-color experiments show in the main text and below.

Now we discuss how we estimate the electron and hole-spin flip rates based on comparison of the power dependence of the single laser resonance fluorescence with our model for single laser excitation, i.e., using only the first term in Eq. (4.5). We model the trion level system with the radiative rates estimated above and vary only γ_e and γ_h .

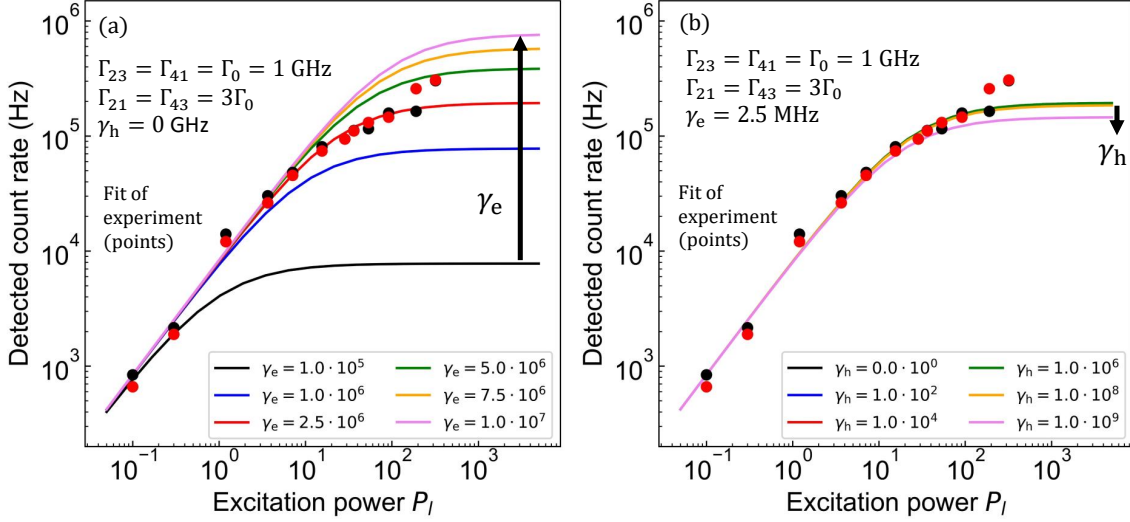


Figure 4.11: Spin-flip rate estimate from excitation power dependent trion emission under single resonant excitation. Lorentzian fits of experimental data (data points) are compared to our model with (a) varied γ_e and fixed $\gamma_h = 0$ to estimate γ_e value, and in (b) with varied γ_h and fixed $\gamma_e = 2.5$ MHz.

First, we estimate the electron spin-flip rate. Typically $\gamma_h \ll \gamma_e \ll \Gamma_0$, therefore we can neglect the hole spin-flip transition and set in our model $\gamma_h = 0$. Then, we determine the most likely value of γ_e by comparing a simulated power dependence of the detected rate for various γ_e with the experimentally observed rates, as shown in Fig. 4.11(a). In good agreement with $\gamma_e = 1.2$ MHz reported in [147], we achieved the best agreement between the model and experimental data for $\gamma_e = 2.5$ MHz. In Fig. 4.11(b), we present a similar simulation, now with fixed $\gamma_e = 2.5$ MHz and varied γ_h to reveal the model dependency on γ_h . In contrast to Fig. 4.11(a), we observe only weak dependence of the model on γ_h , so we set in all our simulations for simplicity $\gamma_h = 0$. This agrees with the fact that we can only observe hole-spin flips during the very short trion lifetime.

4.6.4.5 Excitation-power dependent two-color resonant excitation

Here we study the excitation power dependency of trion state occupations under different resonant excitation schemes and compare the model with the measured two-laser excitation resonance fluorescence. The parameters to model the trion steady-state population are estimated from a least-square fit (discussed below) of the experimental data with an optical power of $P_r = 2.0$ and $P_l = 2.1$ nW, and the best agreement is achieved for parameters $\Gamma_{21} = 2.1$ GHz, $\Gamma_{43} = 2.7$ GHz, $\Gamma_{23} = \Gamma_{41} = 0.8$ GHz, $\gamma_e = 2.5$ MHz, and $\gamma_h = 0$ Hz.

Assuming only minor power-induced rate changes for excitation below P_c , in Fig. 4.12 we study the state population of the individual trion levels as a function of the opti-

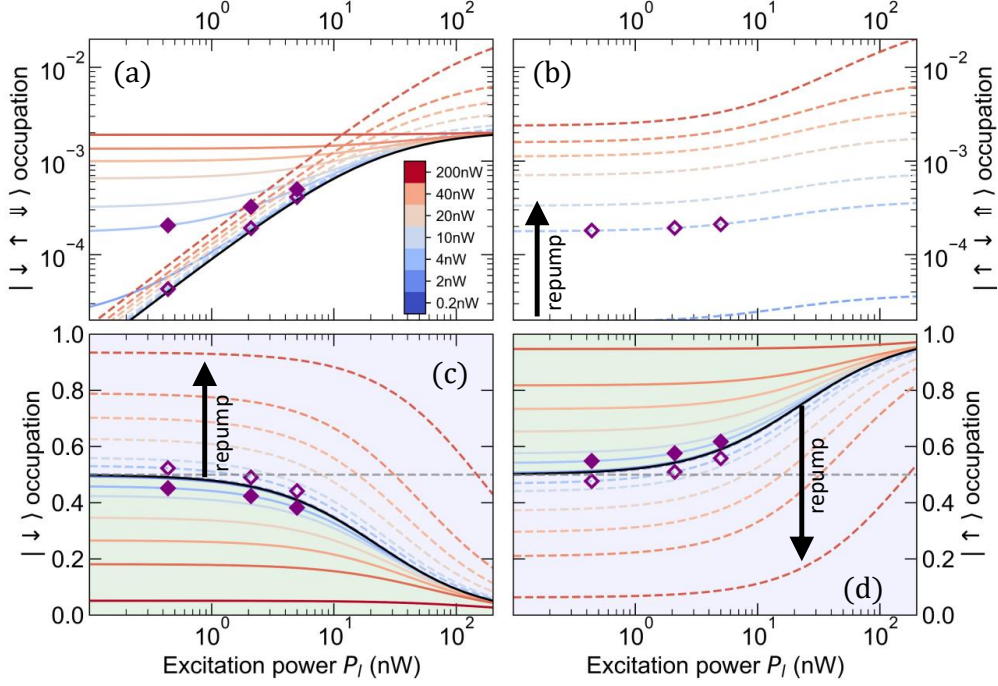


Figure 4.12: Simulation of the two-laser power dependency of trion state occupations. Three different excitation schemes are compared: single-laser excitation (1LRE, black solid line), two-laser excitation of an identical line (2LRE, colored solid lines), and two-color excitation of two distinct transitions (2CRE, colored dashed lines). The power of the second laser is encoded in the color scale. Two regions of ground state occupation are highlighted (c,d): the orange region is accessible only with two-laser excitation of an identical transition, and the blue one only if two distinct transitions are resonantly excited. Purple diamonds (filled if two lasers address the same transition, empty if different ones) correspond to experimental conditions.

cal power of both lasers. Under weak single-laser excitation where the excitation rate is much slower than the radiative rate of the transition, the radiative relaxation of the excited state into both ground states is much faster than the excitation. Therefore the dynamics is dominated by spontaneous emission. Since the radiative rates of the transitions are approximately equal, we observe in (c) and (d) an expected balanced ground state population of ~ 0.5 [147]. With increasing excitation power, repumping of the $|\downarrow\rangle$ population into the excited state becomes relevant, leading to a ground state population imbalance together with a rise of the excited state population, which saturates at high powers, see Fig. 4.12(a). As discussed also in the main text, the dynamics under two-laser excitation of a single transition is equivalent to single-laser excitation with higher excitation power. However, the dynamics changes under the two-color excitation of two distinct transitions shown as dashed lines in Fig. 4.12, where the second laser repumps the population from $|\uparrow\rangle$ to $|\uparrow\downarrow\rangle$. As our model predicts, this repumping is higher with a stronger repumping laser.

Since emission is a measure of the population of the excited states, we can gain insight about expected detected photon rates in different resonant excitation schemes from the total occupation of excited states, shown in Fig. 4.13. Interestingly, the total excited

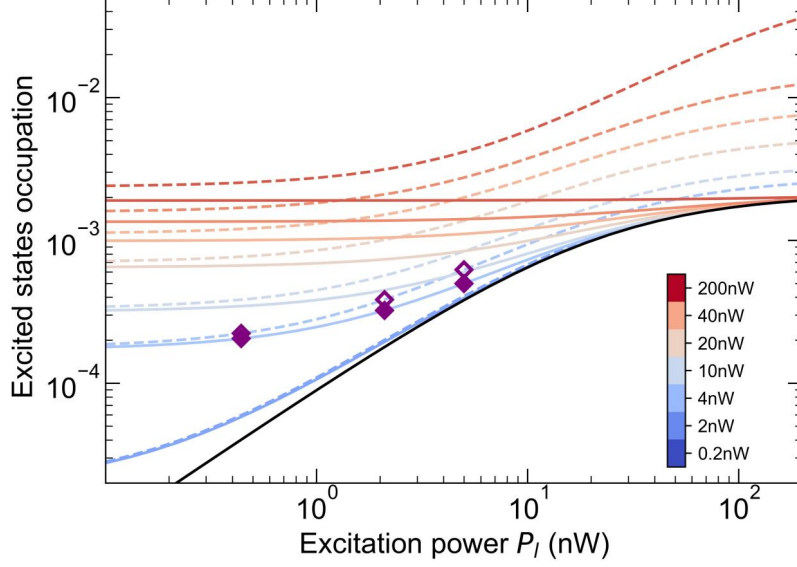


Figure 4.13: Simulated power dependency of the total excited states population. Color and line style encoding is identical to that in Fig. 4.12.

state population is always higher in the two-color excitation scheme. That is because the second laser populates the second excited state which was (due to negligible γ_h) not involved in dynamics if only a single transition was resonantly pumped. This shows that a repump laser can enhance the single-photon rate.

Finally, we discuss additional two-color experiments. In Fig. 4.14, we observe again a 'number sign' like structure, where horizontal and vertical lines represent the trion transitions probed with probe and pump laser, and at the intersections two-laser dynamics appears. Again, spin repumping is clearly visible. We fit the model with an extra term describing the background caused by imperfect cross-polarization filtering on three sets of experimental data measured with fixed pump laser power of $P_r = 2.0$ nW and we have varied optical power of probe laser P_l . We use the following steps to achieve the best agreement between the model and our experiment: First, we fit the experiment using the initial estimate of radiative and spin-flip rates, and QD linewidth and energies, as discussed above. We optimize Zeeman splitting together with the linewidths, therefore we keep all parameters (except $\gamma_h = 0$ Hz) free. In the next step, we fix the parameter describing the background, and QD's f_1^{QD} , f_2^{QD} , Γ , and optimize only radiative rates and γ_e . The best fits of the model are compared to the experiment in Fig. 4.14. Examination of the power-dependence of the parameters shows a power broadening (FWHM) from 1.52 GHz to 1.89 GHz and a small increase of the Zeeman splitting from 3.40 GHz to 3.65 GHz, as also shown in Fig. 4.9. The determined electron and hole spin-flip rates are $\gamma_e = 2.5$ MHz and $\gamma_h = 0$ Hz; radiative rates are increasing with excitation power and are $\Gamma_{21} = 1.1 - 4.9$ GHz, $\Gamma_{43} = 2.1 - 4.5$ GHz, $\Gamma_{23} = \Gamma_{41} = 0.7 - 0.8$ GHz, probably due to the Rabi effect.

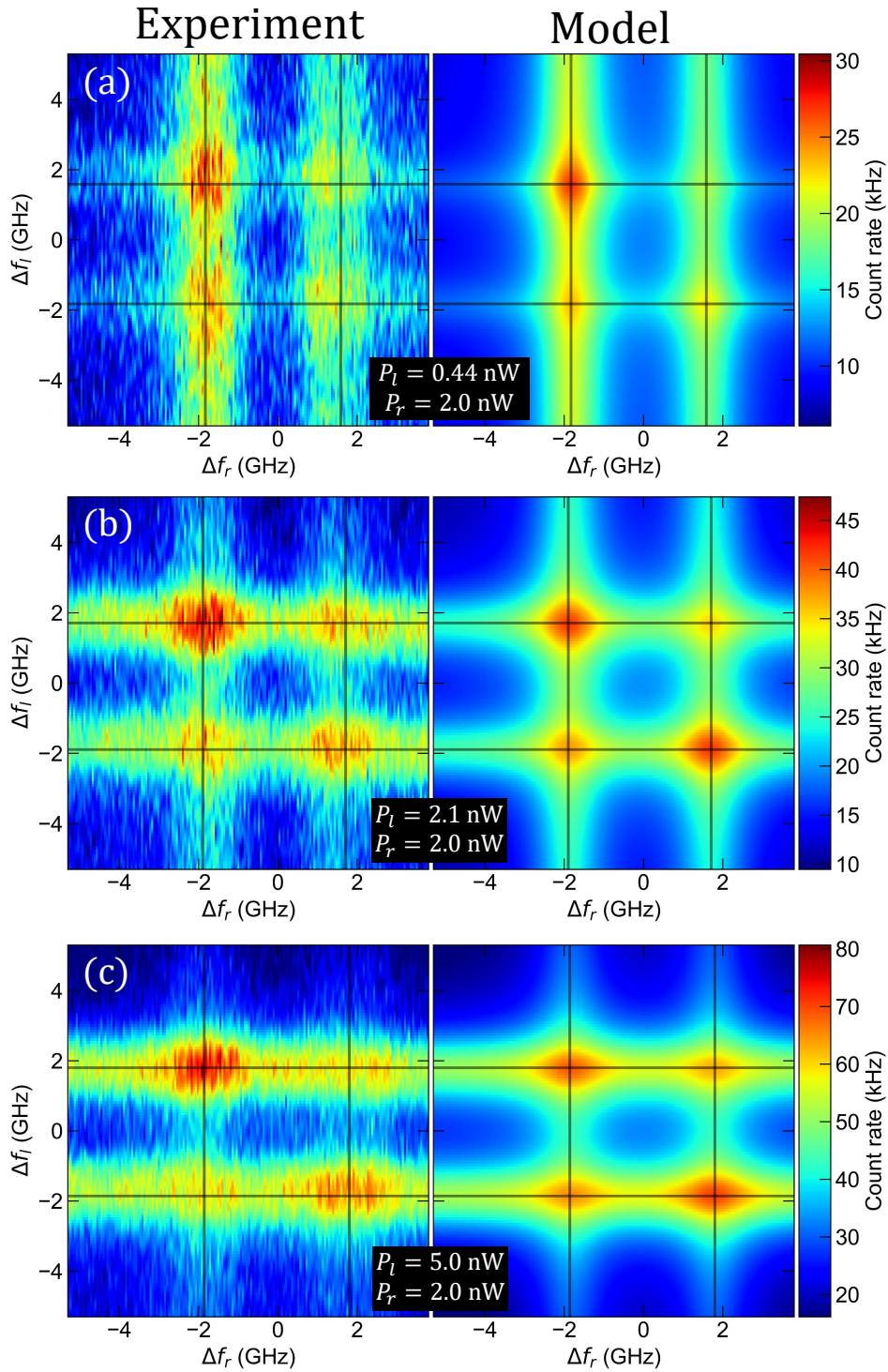


Figure 4.14: False-color plots of the resonant two-color laser scans and model results. Experimental data is shown in the left column, the model in the right column. The repump laser power is kept constant at $P_r = 2.0$ nW, while the pumplaser power P_l is varied: (a) $P_l = 0.44$ nW, (b) $P_l = 2.1$ nW, and (c) $P_l = 5.0$ nW. The transition frequencies of the QD are shown by solid black lines.

5 Single-photon addition and photon correlations

Non-Gaussian multi-photon states of light including displaced Fock states and single-photon-added coherent states are key for continuous-variable quantum information processing. Traditionally, these states are produced using heralded single-photon sources based on nonlinear optics, which relatively easily allows matching of the temporal-spectral properties of the single photon and the coherent state; but this method is intrinsically non-deterministic. Here we theoretically study single-photon addition using different sources of single photons including near-deterministic sources based on quantum dots, and investigate the influence of single-photon purity, brightness, and indistinguishability. We derive analytical results and find that the two-photon correlation function of the generated quantum light can be used to robustly characterize and optimize the fidelity of the generated states.

This chapter contributes to: P. Steindl, V. Tubío, W. Löffler, *Single-photon addition and photon correlations* (in preparation).

5.1 Introduction

In order to implement classically hard-to-simulate continuous variable (CV) photonic quantum circuits [175], Wigner negative [176, 177] resources such as non-Gaussian input states are necessary. These states are also interesting in other fields, for instance they promise improved security in quantum key distribution [178–181], and might find use in quantum metrology [62]. Despite several classes of non-Gaussian states have been identified over the past two decades [182–184], they remain notoriously challenging to produce [185]. The manipulation of light fields on the single-photon level using photon subtraction [186] or addition [187–189] allows for flexible engineering of the photon number statistics [85, 190–192], these operations are the experimental analogues of the application of the annihilation and creation operators a and a^\dagger on a well-defined optical mode [193].

Single-photon addition can be realized by emission of one photon of a photon pair into the classical input light field in a nonlinear crystal [187–189], using a three-level quantum system in an optical cavity [194, 195] or by interference of the input light (e.g. coherent light) with a single photon on an (unbalanced) beam splitter [196–199]. In all cases, the addition of the single photon alters the photon statistics of the input light dramatically [200] resulting in genuinely non-classical states of light [201] for both coherent light [202] or thermal light [203] used as the input.

In contrast to single-photon addition, the related process of single-photon subtraction produces non-classical non-Gaussian states only if performed on a non-classical input state [184, 204]. Single-photon subtraction can be realized in the simplest case using post-selection on single-photon detection at a beam splitter [186, 205].

To date, photon addition was realized mostly using heralded single-photon sources [206, 207] based on spontaneous parametric down-conversion (SPDC). Because the number of photon pairs produced by SPDC follows a thermal distribution [208, 209], heralded production of single photons suffers from a trade-off between single-photon brightness and purity, only recently extensive efforts have improved this to some extent [209, 210]. At the same time, there is fast progress with true single-photon sources (SPSs) [211] based on III-V semiconductor quantum dots in optical microcavities that would in-principle enable fully deterministic and pure single-photon production [13, 15, 17, 18, 28, 57, 102, 103], and with this also deterministic single-photon addition. Here, we investigate and compare single-photon addition for different photon sources including the effect of brightness, purity and indistinguishability. We calculate the second-order correlation function of the resulting quantum light, and find that photon correlation measurement of displaced Fock states is a robust method to optimize wave-function overlap such as mode-matching on the beam splitter.

5.2 Displaced Fock states from quantum interference

A non-polarizing beam splitter (BS) enables quantum interference of two incident optical fields. Based on the beam splitter input-output relations [208, 212], more complex photonic states can be synthesized, the prime example is the Hong-Ou-Mandel (HOM) effect, where two identical single photons “bunch” at the beam splitter [27]. This effect is used for the characterization of the photon indistinguishability of single-photon sources [28], to entangle photons [5, 213], prepare photon-number superposition [85, 214], and in boson sampling [215]. A beam splitter also enables implementing the displacement operator by mixing the input state with a strong coherent state [216]. This effect lies at the heart of

homodyne detection and also allows for state Wigner function tomography [185]. All these effects originate from quantum-state manipulation by interference at the beam splitter.

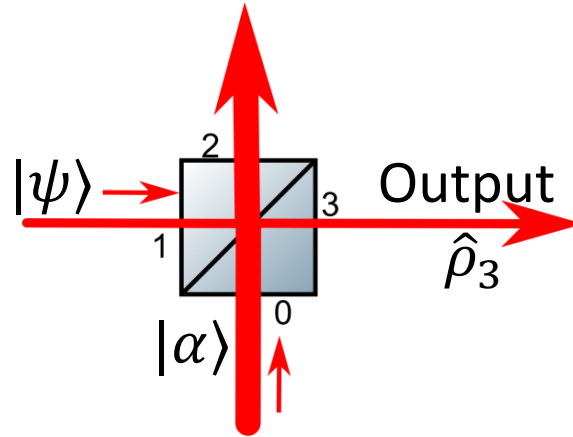


Figure 5.1: General scheme: In a possibly unbalanced beam splitter, the input state $|\psi\rangle$, e.g. a single-photon state, and a classical state of light, for instance the coherent state $|\alpha\rangle$, undergo quantum interference, resulting in possibly non-Gaussian output light.

We assume a loss-less low-reflectivity beam splitter ($R \ll 1$) sketched in Fig. 5.1 and study quantum interference of a coherent state $|\alpha\rangle$ and a state of the form $|\psi\rangle = \sqrt{p_0}|0\rangle + \sqrt{p_1}|1\rangle + \sqrt{p_2}|2\rangle$ by observing output mode 3, ignoring output mode 2. This situation is closely related but different from the conditional generation of single-photon added coherent states using heralding on zero [196, 197] or single-photon detection [217, 218] in mode 2. Our protocol does not rely on heralding and our form of $|\psi\rangle$ allows investigation of the relevant single-photon source properties, the single-photon brightness p_1 and purity $1 - p_2$. The structure of $|\psi\rangle$ has been chosen with the ambition to be able to compare SPDC-based sources (where $p_1 \ll 1$, $p_0 \approx 1 - p_1$, and $p_2 = p_1^2$ in the low-gain limit) and true single-photon sources with $p_1 \approx 1$ and $p_0, p_2 \approx 0$ [219].

Assuming for now that $|\alpha\rangle$ and $|\psi\rangle$ are perfectly indistinguishable in all degrees of freedom, we can calculate the quantum state emerging from the beam splitter in the low-reflection approximation and obtain [199, 216, 220]

$$|\psi_{\text{out}}\rangle \approx \sqrt{p_0}|\gamma\rangle_2|\beta\rangle_3 + \sqrt{p_1} \left(ir\hat{D}_2(\gamma)|1\rangle_2|\beta\rangle_3 + t\hat{D}_3(\beta)|\gamma\rangle_2|1\rangle_3 \right) \\ + \sqrt{p_2} \left(\sqrt{2}irt\hat{D}_2(\gamma)\hat{D}_3(\beta)|1\rangle_2|1\rangle_3 + t^2\hat{D}_3(\beta)|\gamma\rangle_2|2\rangle_3 - r^2\hat{D}_2(\gamma)|2\rangle_2|\beta\rangle_3 \right).$$

Here, $\hat{D}_x(\gamma) = e^{\gamma x^\dagger - \gamma^* x}$ is the displacement operator operating on mode x , and $\alpha = \gamma/t = -i\beta/r$.

We are only interested in the output mode 3, therefore we trace out mode 2 leading to (from now on, the subscript 3 is dropped)

$$\hat{\rho}_3 = \hat{D}(\beta) [A_0|0\rangle\langle 0| + A_1|1\rangle\langle 1| + A_2|2\rangle\langle 2|] \hat{D}(\beta). \quad (5.1)$$

The result is a mixture of displaced vacuum, single- and two-photon states, with the mixing probabilities $A_0 = p_0 + p_1 R + p_2 R^2$, $A_1 = T p_1 + 2RT p_2$, and $A_2 = T^2 p_2$. The mixing probabilities and displacement depend on the beam splitter reflectivity R and transmissivity T , which can be used to control the final state, next to changing the input state $|\psi\rangle$. Eq. (5.1) reduces to results of Windhager et al. [221] in the weak single-photon limit, $p_2 = 0$.

5.2.1 Influence of loss

To give a fair comparison between heralded and true single-photon sources, we implement photon loss in the optical channels. Because coherent states $|\alpha\rangle$, eigenstates of the annihilation operator, do not change their character under loss [222, 223], we model loss only in the $|\psi\rangle$ channel by an additional beam splitter of transmission η . Similar to above, we calculate the final state in mode 3 including photon loss. As expected, the structure of the state in Eq. (5.1) is not altered, only the mixing probabilities A_i are changed and now scale with \tilde{p}_i instead of p_i : $\tilde{p}_0 = \sum_{j=0}^2 [(1-\eta)^{j-1} p_j]$, $\tilde{p}_1 = \eta(p_1 + 2p_2 - 2\eta p_2)$, and $\tilde{p}_2 = \eta^2 p_2$.

5.3 Photon correlations

In experiments, the 2nd-order intensity or photon correlation function $g^{(2)}(\tau)$ is easily accessible because the required Hanbury-Brown & Twiss (HBT) setup [224] is simple, and since it is insensitive to detection efficiencies and loss; further it can be extended to higher-order photon correlations [225]. We can calculate the zero-delay correlation

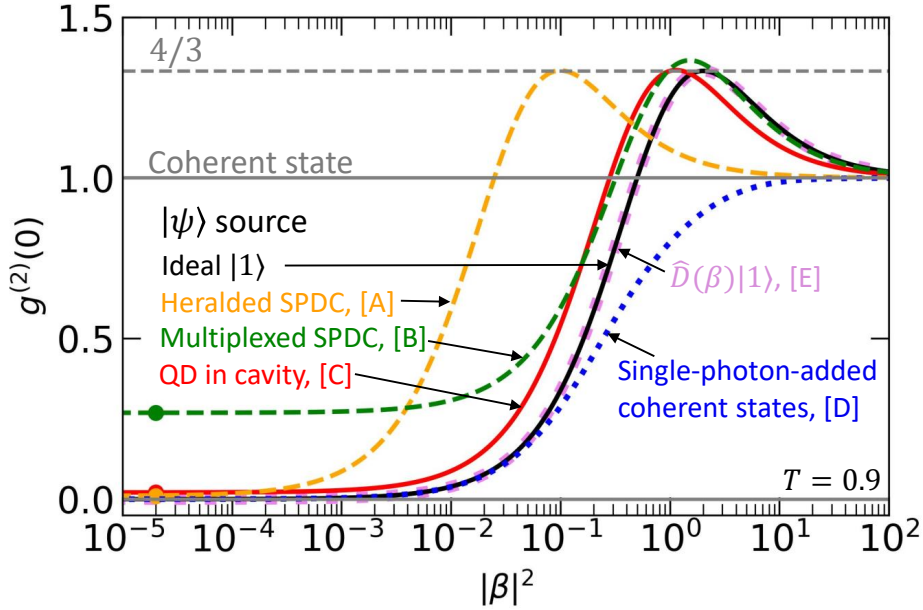


Figure 5.2: Comparison of $g^{(2)}(0)$ as a function of the reflected coherent state $|\beta|^2$ for photon addition at a beam splitter with transmission $T = 0.9$ by quantum interference of $|\alpha\rangle$ with $|\psi\rangle$ for different sources for $|\psi\rangle$: Heralded SPDC single-photon source (orange, A [207]), multiplexed SPDC source (green, B [209]), QD-based true single-photon source (red, C [15]) and an ideal single-photon Fock state (black). We also show $g^{(2)}(0)$ for the single-photon added coherent state (blue, D [187]) and for a displaced single photon state (purple, E [226]). Symbols represent experimentally reported $g^{(2)}(0)$.

function $g^{(2)}(0)$ from the state $\hat{\rho}_3$ using commutation relations between displacement and ladder operators [208, 227], after some steps shown in Appendix 5.7.1 we obtain

$$g^{(2)}(0) = \frac{|\beta|^4 + 4|\beta|^2 T \eta (p_1 + 2p_2) + 2T^2 \eta^2 p_2}{[|\beta|^2 + T \eta (p_1 + 2p_2)]^2}. \quad (5.2)$$

This expression is directly dependent on the photon statistics of $|\psi\rangle$ and allows easy comparison of $g^{(2)}(0)$ for various photon emitters as shown in Fig. 5.2, as a function of the strength of the reflected coherent state $|\beta|^2 = R|\alpha|^2$. In general, we observe a gradual transition from the correlation function of the input state $|\psi\rangle$ [$g_{|\psi\rangle}^{(2)}(0)$] to that of the coherent state [$g_{|\alpha\rangle}^{(2)}(0) = 1$] with increasing coherent state strength.

First, we assume a negligible multi-photon contribution in $|\psi\rangle$, which is a good approximation of current QD-based and weak heralded SPSs with purity exceeding 0.98. Under this condition, $g^{(2)}(0)$ reduces to the expression reported and experimentally confirmed by Shen et al. [228] with the (detected) single-photon brightness $\tilde{p}_1 = \eta p_1$:

$$g^{(2)}(0) = \frac{|\beta|^4 + 4|\beta|^2 T \tilde{p}_1}{[|\beta|^2 + T \tilde{p}_1]^2}. \quad (5.3)$$

Interestingly, this function has a global maximum of $4/3$ in the parameter space of $\{T, \tilde{p}_1, |\alpha|^2\}$ connecting all experimental parameters defining the problem, i.e., the splitting ratio of the BS, the strength of the coherent state given by its mean photon number $|\alpha|^2$, and the single-photon source brightness \tilde{p}_1 by $R|\alpha|^2 = 2\tilde{p}_1 T$.

Now, we focus on the evolution of the quantum state $\hat{\rho}_3$ prepared with an ideal single-photon state ($|\psi\rangle = |1\rangle$) while the coherent state strength gradually increases from zero. On top of the naturally expected quantum-to-classical state transition from the initially purely quantum state (the single-photon Fock state with $g_{|1\rangle}^{(2)}(0) = 0$) into a classical coherent state (with $g_{|\alpha\rangle}^{(2)}(0) = 1$), the theory also predicts a regime of photon bunching with $g^{(2)}(0) > 1$ with a maximal $g^{(2)}(0)$ of $4/3$. As expected, the photon correlation function converges to $g_{\hat{D}(\beta)|1}^{(2)}(0)$ for $T \rightarrow 1$ and $\tilde{p}_1 = 1$ as theoretically predicted for a pure displaced Fock state $g_{\hat{D}(\beta)|1}^{(2)}(0) = \frac{|\beta|^2(4+|\beta|^2)}{(1+|\beta|^2)^2}$ [226].

In Fig. 5.2, we compare $g^{(2)}(0)$ achieved with several experimentally available single-photon sources, and in Table 5.1, we show the relevant characteristics of these sources. For example, heralded SPDC sources with a high single-photon purity $g_{|\psi\rangle}^{(2)}(0) \approx 2\tilde{p}_2/\tilde{p}_1^2 \approx 0.01$ are typically operated in low photon number regime (mean photon number ~ 0.05) to minimize multi-photon contributions; which also results in the limited brightness $\tilde{p}_1 \approx 0.05$ [207]. As expected from Eq. (5.3), we observe the reduction in \tilde{p}_1 as a shift towards weaker coherent state strength for which $g^{(2)}(0)$ becomes maximal. The brightness \tilde{p}_1 of a heralded SPDC source can be artificially increased beyond the thermal statistics limit by time or spatial-bin multiplexing [229]. For example, Kaneda et al. [209] achieved $\tilde{p}_1 = 0.667$ by multiplexing 40 time bins at the cost of worsen single-photon purity to $g_{|\psi\rangle}^{(2)}(0) \approx 0.269$. For the parameters reported in Ref. [209] we find (i) a shift of the bunching regime towards higher $|\beta|^2$ due to higher \tilde{p}_1 , and (ii) $g^{(2)}(0)$ exceeding slightly $4/3$ (by ≈ 0.03) due to non-negligible multi-photon contributions in $|\psi\rangle$.

In contrast to SPDC sources, the single-photon purity of QD-based single-photon sources is, in principle, independent of the brightness. However, the purity can be compromised by QD re-excitation [230, 231] and/or non-ideal excitation-laser filtering [54, 101], contaminating the single photons with multi-photon components. Nevertheless, the purity often exceeds 0.98. Therefore, it is not surprising to expect with the best available QD-based sources [15] similar behavior of $g^{(2)}(0)$ as obtained for an ideal single-photon Fock state, again with its maximal value of $4/3$, at $|\beta|^2 = 2T\tilde{p}_1 = 1.026$.

Finally, we compare the photon correlations of $\hat{\rho}_3$ with correlations expected for theoretical single-photon-added coherent states $C a^\dagger |\beta\rangle$ with $C = 1/\sqrt{1+|\beta|^2}$ [187], which

	Heralded SPDC [207]	Multiplexed SPDC [209]	Quantum dot [15]
Purity $g_{ \psi\rangle}^{(2)}(0)$	0.01	0.269	0.021
Brightness \tilde{p}_1	0.045	0.667	0.566
\tilde{p}_0	0.953	0.231	0.43
\tilde{p}_2	0.002	0.102	0.003

Table 5.1: Single-photon purity, brightness (and \tilde{p}_0 and \tilde{p}_2) of several single photon sources used for the evaluation of $g^{(2)}(0)$ in Fig. 5.2.

can be easily calculated: $g_{C\alpha^\dagger|\beta}^{(2)}(0) = \frac{4|\beta|^2 + 5|\beta|^4 + |\beta|^6}{|1 + 3|\beta|^2 + |\beta|^4|^2} (1 + |\beta|^2)$. Notably, $g_{C\alpha^\dagger|\beta}^{(2)}(0)$ shows a monotonous transition from single-photon to coherent-state correlations without a region of photon bunching. This absence can be used for discriminating single-photon added coherent states from displaced Fock states, which are hard to distinguish otherwise [232].

5.4 Effect of photon indistinguishability

Up to now, we have assumed perfect indistinguishability, or wave-function overlap, of the interfering light fields, now we discuss fields with reduced overlap. First, we introduce an extra degree of freedom enabling us to define indistinguishability - we choose polarization for simplicity, where for linearly polarized input fields, the indistinguishability can easily be modified by polarization rotation with a half-waveplate (HWP). We introduce a HWP in the beam splitter input channel 0 and vary its polarization by adjusting the HWP angle $\theta/2$, as sketched in the inset of Fig. 5.3. For example, an incident H -polarized coherent state $|\alpha, 0\rangle$ is transformed by the HWP to $|\alpha \cos \theta, \alpha \sin \theta\rangle$; we use the two-entry ket notation representing H and V polarization, which allows full control over the mutual indistinguishability M between the input fields. The beam splitter transformation and final states are shown in Appendix 5.7.1, we obtain

$$g_\theta^{(2)}(0) = \frac{|\beta|^4 + 2|\beta|^2 T \eta (1 + M)(p_1 + 2p_2) + 2T^2 \eta^2 p_2}{[|\beta|^2 + T \eta (p_1 + 2p_2)]^2}.$$

In Fig. 5.3, these photon correlations are shown for varied indistinguishability. If the photons are maximally indistinguishable ($M = \cos^2 \theta = 1$), the model reduces to Eq. (5.2) and a prominent bunching region appears, which is absent for the fully distinguishable case with $M = 0$.

The strong dependency of the correlation function caused by the high sensitivity of multi-photon interference on the indistinguishability [233] is a remarkable quality enabling fidelity optimization of the prepared state. Moreover, the correlation measurement performed in the HBT interferometer is loss and imperfect-detection tolerant, in contrast to homodyne Wigner tomography requiring above 50% detection efficiency to successfully reconstruct Wigner negativity [234] and another phase-stabilized coherent state acting as the local oscillator. The combination of these facts makes the correlation-function method experimentally feasible for optimizing indistinguishability and mode-matching at the beam splitter.

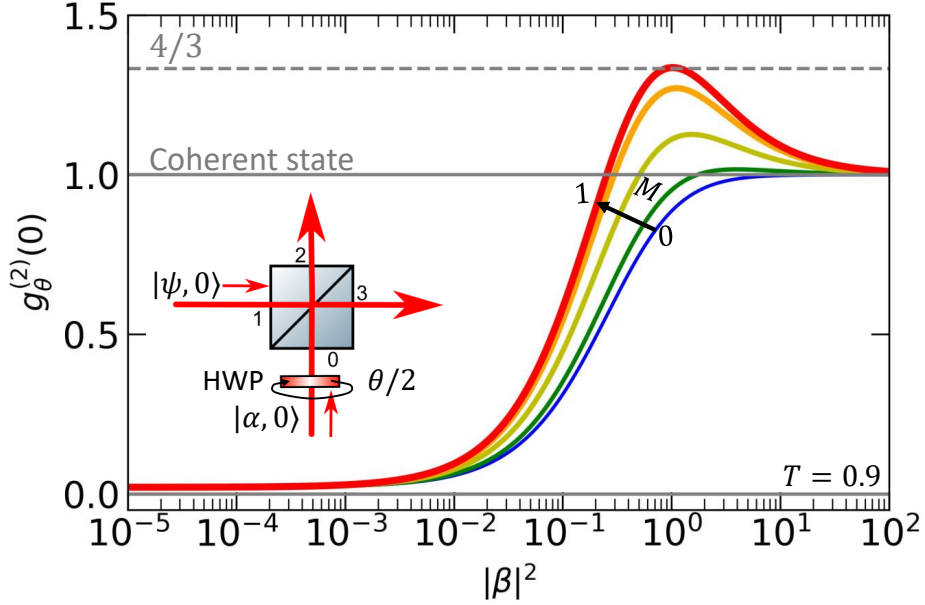


Figure 5.3: The effect of photon indistinguishability on displaced Fock states. The plot shows $g_{\theta}^{(2)}(0)$ as a function of the coherent-state brightness for different indistinguishability M between the coherent state and single photons produced by a quantum dot - cavity single photon source [15]. M is changed by rotating the polarization of one of the beam splitter inputs with a half-wave plate.

Despite the simplicity of the technique, achieving true indistinguishability and thus observation of a $4/3$ photon bunching requires fine optimization. To date, the maximal experimentally reported value is ~ 1.26 of Shen et al. [228], where the indistinguishability is limited to 0.86 by a non-ideal spectral-temporal overlap of the coherent state from attenuated laser pulses and heralded single photons.

5.5 Single-photon addition with quantum dot sources

Figure 5.4 shows an experimental setup for single-photon addition on a beam splitter: the coherent states are made by an attenuated laser, and a QD integrated into an optical microcavity operated at cryogenic temperatures is used as a single-photon source (SPS). For the generation of displaced Fock states, a single-mode fiber splitter is used instead of a free-space beam splitter. The fiber optic splitter (ratio R:T=10:90) enables (i) long-term stable spatial mode overlap between the input fields and (ii) flexible connectivity to fiber-based optical networks for possible applications.

First, we concentrate on the generation of single photons. The QD on-resonance with the optical cavity is excited with a few-10 picosecond long laser pulse. The pulse duration needs to be optimized to minimize QD re-excitation [230, 231] either by fast electro-optic modulation (EOM) of narrow-bandwidth continuous-wave laser (cw laser 1) [235] or using ultra-short duration pulsed laser together with grating-based pulse shaping [236]. The excitation polarization and laser power are chosen to reach the maximal QD population inversion, leading to maximal single-photon brightness p_1 [237]. Then, the emitted single photons are separated from the excitation laser and collected in a single-mode fiber attached to the fiber splitter. Depending on the excitation scheme, the reflected resonant

(non-resonant) laser light is filtered out using cross-polarization [54, 101], or spectral [17] filtering.

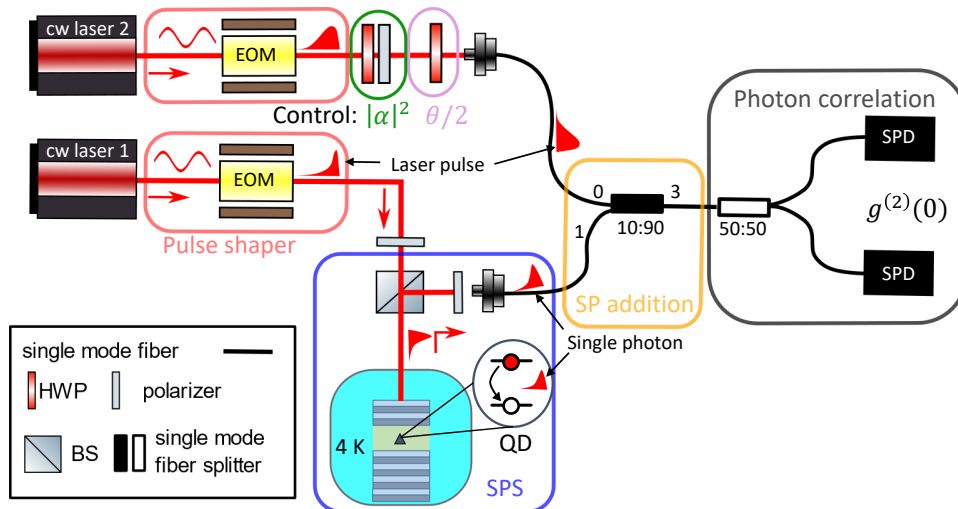


Figure 5.4: Experimental setup for single-photon addition with a QD-based single-photon source. A few-picosecond long laser pulse excites the QD-cavity device, spontaneously emitting a single photon upon relaxation. The single photon is separated from reflected laser light, collected in a polarization-maintaining fiber, and interfered with a coherent state from another laser source with control over all degrees of freedom on a polarization-maintaining fiber splitter.

Now, we discuss the preparation of coherent states $|\alpha\rangle$. Laser 2 is tuned to be resonant with the QD emission and the strength $|\alpha|^2$ of the coherent state can be tuned with by a half-wave plate (HWP) in combination with a linear polarizer before being coupled into a single-mode fiber connected to the fiber splitter (input port 0). To achieve maximal state overlap on the fiber splitter, we prepare the coherent states in the form of optical pulses. This, in contrast to the continuous-wave regime, enables us to control all degrees of freedom of the coherent state and engineer them for maximal interference with the single photons: (i) the spatial degrees are matched using a single-mode fiber splitter, (ii) the polarization of the coherent state is controlled by adjusting the angle $\theta/2$ of an extra half-wave plate placed in front of the fiber coupler, and finally (iii), the arrival time synchronization and spectral-temporal overlap can be optimized by pulse shaping of the coherent laser pulses. For example, perfect matching to the lifetime-limited trion emission with mono-exponential decay described by the trion lifetime T_1 [238] requires exponential coherent state pulses with duration T_1 .

This wave-function overlap optimization, requiring iterative fine-tuning of all modes of the light fields, becomes very challenging experimentally in the presence of photon loss and limited detection efficiencies. However, as also discussed above, the wave-function overlap can be maximized based on the photon-correlation $g^{(2)}(0)$ signal, which is insensitive to experimental imperfections.

Finally, we comment on the displaced Fock state generation rates achievable with current QD-based single-photon source technology. The rate is, in principle, limited only by the emission properties of the QD, i.e., its in-fiber brightness defining single-photon gain per pulse and T_1 limiting the excitation rate. In-fiber single-photon rates up to 1 GHz with an in-fiber brightness of $\tilde{p}_1 = 0.57$ at a lifetime of $T_1 \sim 50$ ps has been obtained [15].

In comparison, all currently available SPDC-based sources have more than one order of magnitude smaller single-photon rates due to heralding and necessary low \tilde{p}_1 , or limited multiplexing rates, a comparison is given in Ref. [209].

5.6 Conclusions

In conclusion, we have theoretically studied the second-order photon correlation function $g^{(2)}(0)$ of displaced Fock states generated by quantum interference of coherent and single-photon states. We have modelled the single photons to account for experimentally unavoidable imperfections, limited brightness and reduced purity, and have derived formulas directly connecting the resulting photon correlations to the single-photon source properties. We have shown that for the case of true single-photon sources, the correlations show universal photon bunching with $g^{(2)}(0)$ reaching $4/3$. This bunching is very sensitive to the indistinguishability of the single photons and the coherent state at the beam splitter, which can therefore be used for optimization of indistinguishability at the beam splitter including mode-matching and single-photon properties, and allows discrimination of single-photon added coherent states and displaced Fock states. Finally, we have evaluated an experiment with a realistic quantum-dot based true single-photon source, which will allow production of GHz-rate displaced Fock states that might be useful for quantum key distribution [178–181] and photon boson sampling [232, 239].

5.7 Appendix

5.7.1 Derivation of $g_\theta^{(2)}(0)$

Here we discuss essential steps in the derivation of $g_\theta^{(2)}(0)$ presented in the main text. As shown in Fig. 5.3, the HWP enables continuous variation of the polarization by adjusting its angle $\theta/2$. We use two-component ket notation to represent the HWP transformation; the initially H -polarized coherent state is transformed as $|\alpha, 0\rangle \xrightarrow{\text{HWP}(\theta/2)} |\alpha \cos \theta, \alpha \sin \theta\rangle$. Under this transformation in the low-reflection approximation, the state emerging from the BS in mode 3 after a partial trace over mode 2 is

$$\hat{\rho}_3 = \hat{D}_V(\beta_V) \hat{D}_H(\beta_H) [A_0|0, 0\rangle\langle 0, 0| + A_1|1, 0\rangle\langle 0, 1| + A_2|2, 0\rangle\langle 0, 2|] \hat{D}_H^\dagger(\beta_H) \hat{D}_V^\dagger(\beta_V).$$

This state is a two-mode mixture of displaced Fock states with displacement $\beta_V = \beta \sin \theta$, $\beta_H = \beta \cos \theta$. The second-order photon correlation function can be calculated from $g_\theta^{(2)}(0) = \frac{\text{Tr}(\hat{\rho}_3 a^\dagger a^\dagger a a)}{[\text{Tr}(\hat{\rho}_3 a^\dagger a)]^2}$. In the following derivation, we have used: (i) the cyclic properties of the trace, (ii) the commutation relations between ladder and displacement operators [227], (iii) unitarity of the displacement operator, and (iv) the relation $\hat{n} = \hat{n}_H + \hat{n}_V$ connecting the polarization modes to non-polarized detection. For simplification, we define $\hat{\rho}_{3,H} = A_0|0\rangle\langle 0| + A_1|1\rangle\langle 1| + A_2|2\rangle\langle 2|$, and evaluate the numerator and denominator separately.

The numerator:

$$\begin{aligned} \text{Tr}_{\text{V,H}}[\hat{\rho}_3 a_H^\dagger a_H] &= \text{Tr}_H[(a_H^\dagger + \beta_H^*)(a_H + \beta_H)\hat{\rho}_{3,H}] = A_1 + 2A_2 + |\beta_H|^2 \\ \text{Tr}_{\text{V,H}}[\hat{\rho}_3 a_V^\dagger a_V] &= \text{Tr}_{\text{H,V}}[(a_V^\dagger + \beta_V^*)(a_V + \beta_V)\hat{\rho}_{3,H}] = |\beta_V|^2 \\ \text{Tr}_{\text{V,H}}(\hat{\rho}_3 a^\dagger a) &= \text{Tr}_{\text{V,H}}[\hat{\rho}_3 (a_H^\dagger a_H + a_V^\dagger a_V)] = A_1 + 2A_2 + |\beta|^2 \end{aligned}$$

The denominator:

$$\begin{aligned} \text{Tr}_{\text{V,H}}[\hat{\rho}_3 \hat{n}_H^2] &= \text{Tr}_H\{[(a_H^\dagger + \beta_H^*)(a_H + \beta_H)]^2 \hat{\rho}_{3,H}\} = \text{Tr}_H\{[(a_H^\dagger + \beta_H^*)(a_H + \beta_H)]^2 \hat{\rho}_{3,H}\} \\ &= \text{Tr}_H[\hat{n}_H^2 + 4|\beta_H|^2 \hat{n}_H + |\beta_H|^2 + |\beta_H|^4] \hat{\rho}_{3,H} \\ &= A_1 + 4A_2 + 4|\beta_H|^2(A_1 + 2A_2) + |\beta_H|^2 + |\beta_H|^4 \\ \text{Tr}_{\text{V,H}}[\hat{\rho}_3 \hat{n}_V^2] &= \text{Tr}_H\{[(a_V^\dagger + \beta_V^*)(a_V + \beta_V)]^2 \hat{\rho}_{3,H}\} = |\beta_V|^2 + |\beta_V|^4 \\ \text{Tr}_{\text{V,H}}[\hat{\rho}_3 \hat{n}_H \hat{n}_V] &= |\beta_V|^2 \text{Tr}_H\{(a_H^\dagger + \beta_H^*)(a_H + \beta_H)\hat{\rho}_{3,H}\} = |\beta_V|^2(A_1 + 2A_2 + |\beta_H|^2) \\ \text{Tr}_{\text{V,H}}(\hat{\rho}_3 a^\dagger a^\dagger a a) &= \text{Tr}_{\text{V,H}}[\hat{\rho}_3 (\hat{n}_H^2 + 2\hat{n}_H \hat{n}_V + \hat{n}_V^2 - \hat{n}_H - \hat{n}_V)] \\ &= |\beta|^4 + 2|\beta|^2[1 + \cos^2 \theta](A_1 + 2A_2) + 2A_2 \end{aligned}$$

With this, the photon correlations can be expressed as

$$\begin{aligned} g_\theta^{(2)}(0) &= \frac{|\beta|^4 + 2|\beta|^2[1 + \cos^2 \theta](A_1 + 2A_2) + 2A_2}{[|\beta|^2 + A_1 + 2A_2]^2} \\ &= \frac{|\beta|^4 + 2|\beta|^2 T\eta(1 + \cos^2 \theta)(p_1 + 2p_2) + 2T^2\eta^2 p_2}{[|\beta|^2 + T\eta(p_1 + 2p_2)]^2} \end{aligned} \quad (5.4)$$

where the correlations in the last step are represented directly in terms of the photon number probabilities of the single-photon source. For the case of fully indistinguishable photonic fields, this reduces to

$$g^{(2)}(0) = \frac{|\beta|^4 + |\beta|^2 T\eta(p_1 + 2p_2) + 2T^2\eta^2 p_2}{[|\beta|^2 + T\eta(p_1 + 2p_2)]^2}. \quad (5.5)$$

This function is maximized for $|\beta|^2 = 2T\eta[p_1 + 2p_2 - p_2/(p_1 + 2p_2)]$. Assuming negligible multi-photon contributions (simply by setting $p_2 = 0$) which is a good approximation of state of the art single-photon sources, the expression in Eq. (5.5) can be further simplified to

$$g^{(2)}(0) = \frac{|\beta|^4 + 4|\beta|^2 T \tilde{p}_1}{[|\beta|^2 + T \tilde{p}_1]^2}$$

where we used the definition of detected single-photon brightness $\tilde{p}_1 = \eta p_1$. Interestingly, this function has a global maximum of $4/3$.

5.7.2 Photon correlations: single-photon-added coherent states vs displaced Fock states

Shen et al. [228] studied photon correlations before, in a notation consistent with our work they have obtained

$$g^{(2)}(0) = \frac{|\beta|^4 + 4|\beta|^2 T \tilde{p}_1 + 4\tilde{p}_1 T |\beta|^4 + \tilde{p}_1 T |\beta|^6}{[\tilde{p}_1 T + |\beta|^2 + 2\tilde{p}_1 T |\beta|^2 + \tilde{p}_1 T |\beta|^4]^2} (1 + \tilde{p}_1 T |\beta|^2).$$

This formula, appearing also in other works [240], is based on a somewhat unconventional ordering of non-commuting operators after the beam splitter transformation, which is inconsistent with literature (e.g. [199, 217, 241, 242]). Nevertheless, for a weak attenuated laser with $|\beta|^2 \ll 1$ and a weak heralded single-photon source ($\tilde{p}_1 \ll 1$) results in the approximate expression

$$g^{(2)}(0) = \frac{|\beta|^4 + 4|\beta|^2 T \tilde{p}_1}{[\tilde{p}_1 T + |\beta|^2]^2},$$

which described well experimental data. Our formalism results in the same result for $p_2 = 0$ and the same approximations. This agreement is not surprising, since the difference arises only from the commutation relation $[\hat{a}, \hat{D}(\beta)] = \beta \hat{D}(\beta)$ [227] which vanishes for weak coherent states.

6 Artificial coherent states of light by multi-photon interference in a single-photon stream

Coherent optical states consist of a quantum superposition of different photon number (Fock) states, but because they do not form an orthogonal basis, no photon number states can be obtained from it by linear optics. Here we demonstrate the reverse, by manipulating a random continuous single-photon stream using quantum interference in an optical Sagnac loop, we create engineered quantum states of light with tunable photon statistics, including approximate weak coherent states. We demonstrate this experimentally using a true single-photon stream produced by a semiconductor quantum dot in an optical microcavity, and show that we can obtain light with $g^{(2)}(0) \rightarrow 1$ in agreement with our theory, which can only be explained by quantum interference of at least 3 photons. The produced artificial light states are, however, much more complex than coherent states, containing quantum entanglement of photons, making them a resource for multi-photon entanglement.

This chapter has been published: P. Steindl, H. Snijders, G. Westra, E. Hissink, K. Iakovlev, S. Polla, J.A. Frey, J. Norman, A.C. Gossard, J.E. Bowers, D. Bouwmeester, W. Löffler, *Artificial coherent states of light by multi-photon interference in a single-photon stream*, Phys. Rev. Lett. **126**, 143601 (2021) [85].

6.1 Introduction

Coherent states of light are considered to be the most classical form of light, but expressed in photon number (Fock) space, they consist of a complex superposition of a number of photon number (Fock) states. Because coherent states are non-orthogonal, it is not possible with linear-optical manipulation and superposition of coherent states to obtain pure photon number (Fock) states. The opposite is possible in principle, for instance by attenuating high- N photon number states one could synthesize coherent states. However, high- N Fock states are not readily available, but recently high-quality sources of single-photon ($N = 1$) states became accessible based on optical nonlinearities on the single-photon level. In particular, by using semiconductor quantum dots in optical microcavities [28], single-photon sources with high brightness, purity, and photon indistinguishability were realized [13, 18, 102, 103]. Under loss, in contrast to higher- N Fock states, single-photon streams never lose their quantum character since single photons cannot be split, loss reduces only the brightness. Single photons are an important resource for quantum information applications [5].

In order to synthesize more complex quantum states of light, multiple identical single-photon streams can be combined using beam splitters, where unavoidably quantum interference appears, the well-known Hong-Ou-Mandel (HOM) effect [27]. This effect leads to photon bunching if the incident photons are indistinguishable, therefore enables the production of higher photon number states but only probabilistically. HOM interference is also used for characterization of the photon indistinguishability of single-photon sources [28], which is done mostly in the pulsed regime where detector time resolution is not an issue. The regime of a continuous but random stream of single photons has been explored much less in this aspect, HOM interference with continuous random stream of true single photons has been observed in Refs. [243] and [244]. The HOM effect can also be used to entangle photons; in combination with single-photon detection and post-selection, it also can act as a probabilistic CNOT gate [5, 213, 245].

Here we make use of HOM interference in a Sagnac-type delay loop with a polarizing beam splitter (Fig. 6.1), where HOM interference happens at a half-wave plate in polarization space¹. Similar setups are proposed for boson sampling [41, 246] and used for producing linear photonic cluster states [40, 42, 247], an emerging resource for universal quantum computation [5, 8, 10]. Since we operate with a random but continuous single-photon stream, the repeated quantum interference and enlargement of the spatio-temporal superposition leads to an infinitely long quantum superposition. By tuning the photon indistinguishability we observe, in agreement with our theoretical model, photon correlations approaching that of coherent light ($g^{(2)}(0) \rightarrow 1$), and from our theoretical model, we deduce that the photon number distribution indeed corresponds to coherent light, more precisely weak coherent light with a mean photon number $\bar{n} \approx 0.2$.

6.2 Single-photon source

Experimentally, as an efficient single-photon source, we use a self-assembled InGaAs/GaAs quantum dot (QD) embedded in polarization-split micropillar cavity grown by molecular beam epitaxy [18, 90]. The QD layer is embedded in a p - i - n junction, separated by a

¹A half-wave plate with its optical axis at 22.5° acting on the two polarization modes is equivalent to the action of a beam splitter on the two spatial input modes.

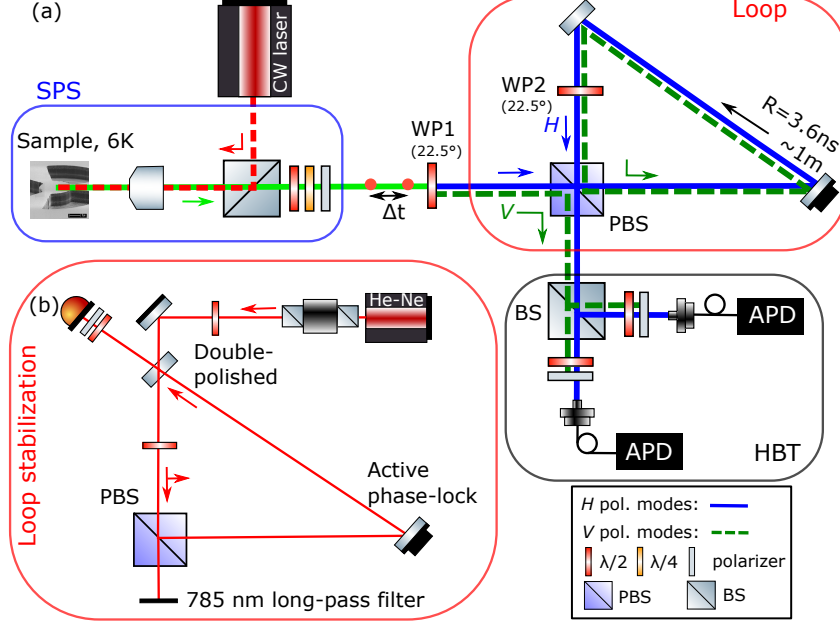


Figure 6.1: Experimental setup - (a) Photons from the single-photon source (SPS) are diagonally polarized by WP1 before sent to the loop setup consisting of a polarizing beam splitter and half-wave plate WP2 at 22.5° . Light from the loop setup is analyzed with the polarization-resolved HBT setup. Panel (b) shows the interferometric loop length stabilization.

27 nm-thick tunnel barrier from the electron reservoir, to enable tuning of the QD resonance around 935 nm by the quantum-confined Stark effect. The QD transition with a cavity-enhanced lifetime of $\tau_r = 130 \pm 15$ ps is resonantly excited with a continuous-wave laser, which is separated by a cross-polarization scheme [90] from the single photons that are collected in a single-mode fiber. This linearly (H) polarized single-photon stream Ψ_{in} is then brought by WP1 (22.5°) in a superposition of two polarization modes; H -polarized photons enter the 1 m long free-space delay-loop wherein WP2 (22.5°) brings them again in a superposition, only H -polarized photons are transmitted from the loop towards the detection part. Detection is done with a standard Hanbury Brown and Twiss (HBT) setup with a non-polarizing beam splitter, after which the photons are coupled into multi-mode fibers (coupling efficiency $\sim 90\%$) and detected with silicon avalanche photon detectors (APDs, 25% efficiency) and analyzed with a time-correlated single-photon counting computer card. With motorized half-wave plates followed by a fixed linear polarizer before each multi-mode fiber coupler, the setup allows to distinguish correlations between photons from the loop ($g_{HH}^{(2)}(\tau)$), only directly from the source ($g_{VV}^{(2)}(\tau)$), and to analyze cross-correlations between photons from the loop and source $g_{VH}^{(2)}(\tau)$. Note that measurement in VV polarization is equivalent to a standard $g^{(2)}(\tau)$ measurement of the single-photon source and can be used to obtain a reference without changing the experimental setup. We have chosen a beam waist of 0.50 mm inside the loop in order to reduce diffraction loss; the total round-trip transmission η_L is $\sim 90\%$. Further, we use active phase-stabilization of the loop length by using a mirror on a piezoelectric actuator (Fig. 6.1(b)) and a frequency-stabilized He-Ne laser entering the loop through a doubly polished mirror, this is needed because weak pure single-photon states interfere phase-sensitively [214].

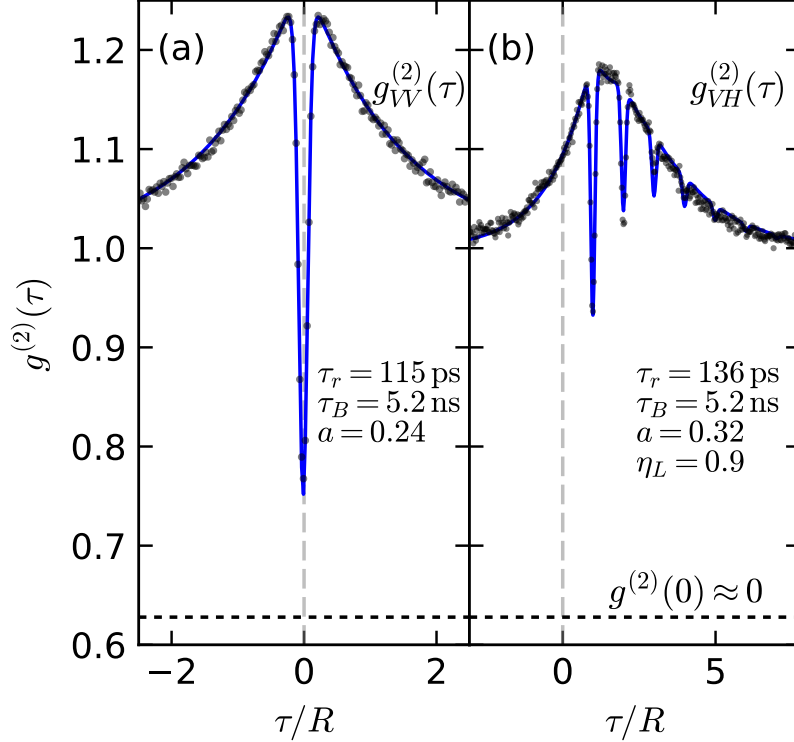


Figure 6.2: Characterization of the single-photon source (a) and loop setup (b), experimental data has been accumulated over 3 hours; solid lines show the model calculations. In (a) the three-level model is fitted to the experimental $g_{VV}^{(2)}(\tau)$ data to obtain the single-photon source and detector parameters used throughout the paper. Panel (b) shows VH correlations between photons directly from the source and from the loop, confirming the validity of our model.

We operate the QD single-photon source with relatively high excitation power (~ 50 nW) to obtain a bright single-photon stream (detected single-photon detection rate of 200 kHz), with the consequence that unwanted effects produce a broad correlation peak superimposed to $g^{(2)}(\tau)$. In order to correctly take this into account in our model, we first measure in VV detector configuration the source correlations (Fig. 6.2(a)) and model it using a three-level system [248, 249], where τ_B is the lifetime of the additional dark state:

$$g_{3L}^{(2)}(\tau) = 1 - (1 + a) \exp(-|\tau|/\tau_r) + a \exp(-|\tau|/\tau_B). \quad (6.1)$$

Further, for comparison to experimental results with expected $g^{(2)}(0)$ below 0.1 [18], the theoretical data are convolved with a Gaussian instrument response function (IRF) of our single-photon detectors with FWHM = 0.523 ns [195], limiting the smallest detectable $g^{(2)}(0) \approx 0.63$. From fitting the model to the experimental data, we obtain a bunching strength $a = 0.24 \pm 0.03$ and $\tau_B = 5.2 \pm 0.3$ ns, similar time scales were observed before [250].

6.3 Photon correlations between source and delay loop

To start building up a theoretical model and to characterize the delay loop, we now measure in VH detection configuration the cross-correlation function between photons directly from source and photons from the delay loop $g_{VH}^{(2)}(\tau)$, shown in Fig. 6.2(b). The V detector is connected to the start trigger input of a correlation card and the H detector to the stop channel, therefore the measured correlation $g_{VH}^{(2)}(\tau)$ is as expected asymmetric around $\tau = 0$. Considering an H -polarized photon entering the loop, WP2 transforms it into an $\frac{1}{\sqrt{2}}(|H\rangle + |V\rangle)$ diagonally polarized state. The H -polarized part of the state leaves the loop via the polarizing beam splitter, while the V part remains in the loop and is transformed by WP2 into $\frac{1}{\sqrt{2}}(|H\rangle - |V\rangle)$, this process is repeating itself infinitely. In the case of a limited amount of photons in well-defined time bins, the output can easily be described, the chance that a photon leaves the loop after r round trips is $(\eta_L/2)^r$ [251]. In our case of a random single-photon stream, the case is more complex as we describe the light stream by correlation functions which we also measure experimentally.

In order to predict $g_{VH}^{(2)}(\tau)$ theoretically, we use as an approximation that maximally two photons are in the system, which we prove later to be appropriate here. We obtain for the detected state for two incident photons with delay $\Delta t \neq 0$ (it is a single-photon source) a weighted superposition of single-photon streams shifted by time $r \cdot R$, where r is the round-trip number and R the round-trip delay (see Appendix, Sec. 6.6.1):

$$|\Psi_{VH}\rangle = \sum_{\Delta t \neq 0} V^\dagger \left[\sqrt{\frac{\eta_L}{2}} H_{R+\Delta t}^\dagger + \sum_{r \geq 2} \left(-\sqrt{\frac{\eta_L}{2}} \right)^r H_{r \cdot R + \Delta t}^\dagger \right] |0\rangle. \quad (6.2)$$

The state is written in terms of photon creation operators V_t^\dagger and H_t^\dagger , where the polarization mode is represented by the capital letter, the detection time is given in the subscript. Assuming a source continuously emitting perfect single photons, we can derive from the two-photon state an analytical expression for $g_{VH}^{(2)}(\tau)$:

$$g_{VH}^{(2)}(\tau) = 1 - \sum_{m > 0} \left(\frac{\eta_L}{2} \right)^m \left(1 - g_{3L}^{(2)}(\tau - m \cdot R) \right). \quad (6.3)$$

Here, photons with $\Delta t = z \cdot R, z \in \mathbb{Z}$ are correlated by the loop and create dips in $g_{VH}^{(2)}(\tau)$ for $\tau = m \cdot R$ where $m \in \mathbb{N}$ iterates over round-trips. We observe good agreement between theory and experimental data in Fig. 6.2(b). Note that also the shifted broad peak originating from strong driving is correctly reproduced.

6.4 Building artificial coherent states

Finally, we investigate the correlations of photons emerging from the loop by measuring $g_{HH}^{(2)}(\tau)$, shown in Fig. 6.3. We find that $g_{HH}^{(2)}(\tau = 0)$ is now highly sensitive to the indistinguishability or wave function overlap M of consecutive photons produced by the quantum dot, which we can tune experimentally simply by changing the spatial alignment of the delay loop. Assuming a perfect single-photon source, the wave function overlap M is equal to the interferometric visibility V , see Appendix 6.6.3 for details. The model for the case of distinguishable photons, shown in Fig. 6.3(a), can be calculated again in the

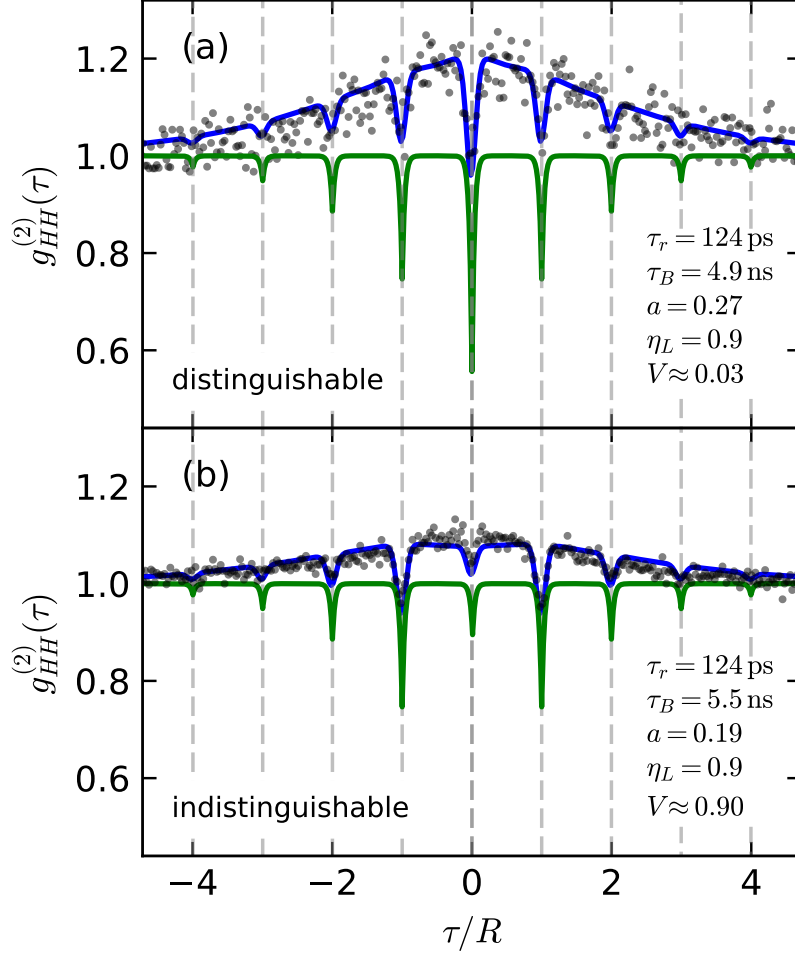


Figure 6.3: Photon correlations $g_{HH}^{(2)}(\tau)$ (symbols) for misaligned loop (a, $V \approx 0.03$, distinguishable photons) and aligned loop (b, $V \approx 0.9$, indistinguishable photons) compared to the model predictions (blue curves). Raw coincidence counts corresponding to $g_{HH}^{(2)}(\tau) = 1$ were 880 (a) and 9700 (b). The green curves show the model results for the case without spectral diffusion.

two-photon picture, and we obtain

$$g_{HH}^{(2)}(\tau) = 1 - \frac{2\eta_L}{4 - \eta_L^2} \sum_{m \in \mathbb{Z} \setminus \{0\}} \left(\frac{\eta_L}{2}\right)^{|m|} \left(1 - g_{3L}^{(2)}(\tau - m \cdot R)\right) - \left(1 - g_{HH}^{(2)}(0)\right) \left(1 - g_{3L}^{(2)}(\tau)\right), \quad (6.4)$$

where the value of $g_{HH}^{(2)}(0)$ has to be calculated using full quantum state propagation which we describe now.

The delay loop leads to quantum interference of photons at different times in the incident single-photon stream, and HOM photon bunching occurring at WP2 produces higher photon number states in a complex quantum superposition. We have developed a computer algorithm that can simulate $g_{HH}^{(2)}(0)$, see Appendix 6.6.2 for details. For the results shown here, we take up to 20 photons or loop iterations into account to approximate the experiment with a continuous photon stream. For completely distinguishable photons we

obtain $g_{HH}^{(2)}(0) = 0.49$ (corrected for dark state dynamics), which agrees well with the experimentally observed correlations in Fig. 6.3(a).

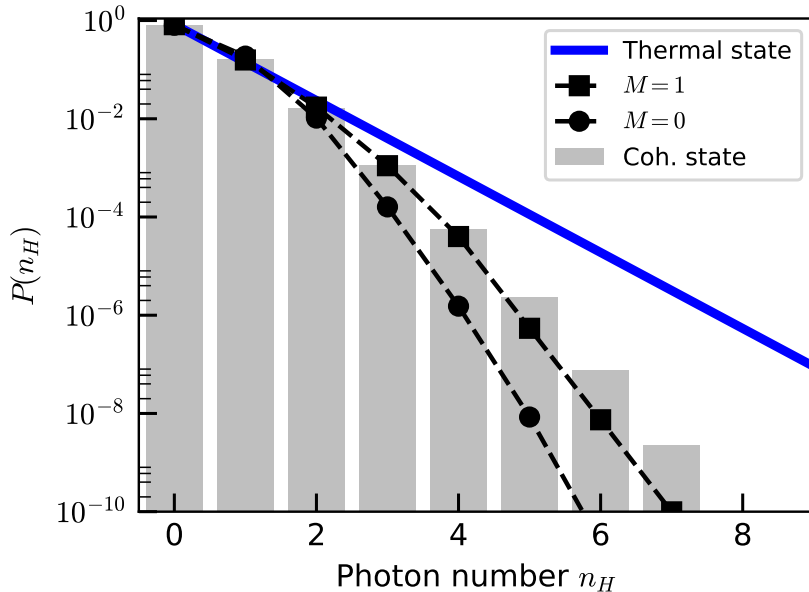


Figure 6.4: Comparison of the photon number distribution of a weak coherent state (bars) and thermal state (through blue line) with same mean photon number $\bar{n} \approx 0.2$, to the results from our theoretical model (squares for the case of indistinguishable photons, $M = 1$, and circles for the case of distinguishable photons, $M = 0$). A fixed round-trip loss of 0.1 is included in both cases. The artificial state matches best to the weak coherent light state.

For the case of indistinguishable photons with maximal wave-function overlap $M \approx 0.9$, we observe in Fig. 6.3(b) that the dip at $\tau = 0$ almost disappears. This is because the (multi-)photon bunching increases the weight of higher photon number states, and, as we show now, produces quasi-coherent states of light with $g^{(2)}(0) \approx 1$. Based on our computer simulation, we investigate the photon number distribution $P(n)$, which is shown in Fig. 6.4. We see very good agreement of the artificial coherent state (indistinguishable photons, $M = 1$, experimentally we achieve $M = 0.9$) to an exact weak coherent light state with the same mean photon number ($\bar{n} = 0.2$). In Appendix 6.6.5, we show that the artificial coherent state is also very close to being an eigenstate of the annihilation operator, as expected. Now, using the full simulated quantum state, we calculate the quantum fidelity F to the exact coherent state and obtain $1 - F \approx 10^{-3}$ for both $M = 1$ and $M = 0.9$. We also calculate the l_1 -norm of coherence [252] C_{l_1} , also here the deviation from the exact coherent state is very small, smaller than 10^{-3} relatively. From comparison of the density matrices, we see that deviations occur mainly in the higher photon number components, those are weak and do not contribute much to the aforementioned measures. These small deviations are also visible in the Wigner function of the artificial coherent state.

In the model, we can ignore a round-trip dependent decrease of M due to beam diffraction since the effect is only $\sim 2\%$, see Section 6.6.2.2, and from Fig. 6.4 we also see why it was justified above to ignore $N > 2$ states for prediction of $g_{VH}^{(2)}(\tau)$ and $g_{HH}^{(2)}(\tau \neq 0)$, their contribution is negligible (Appendix 6.6.4). In our experiment, we can also observe the transition to an artificial coherent state by tuning the photon indistinguishability M to intermediate values, which is shown in Fig. 6.5, again in good agreement with our

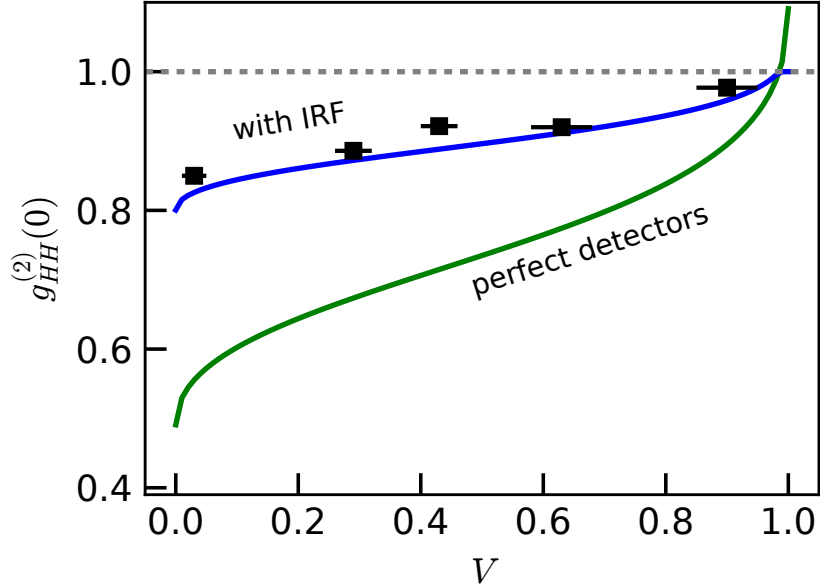


Figure 6.5: Experimental $g_{HH}^{(2)}(0)$ (black squares), corrected for dark state dynamics, compared to our theoretical expectations (blue line, convolved with IRF) as a function of the photon indistinguishability or wave-function overlap, expressed by the visibility V . Light with coherent photon statistics is obtained for $V \rightarrow 1$. The green line shows the expected results for detectors with perfect timing resolution. Results include a fixed round-trip loss of 0.1.

model. Compared to a weak thermal state of light which can be produced by spontaneous emission of many single-photon emitters coupled to the same cavity mode [253], although having similar $P(n)$ for low \bar{n} , as shown in Fig. 6.4, $g^{(2)}(0)$ would show a peak which is not the case here. The simple characterization method based only on two-photon correlations measurement presented here could also be useful for characterization of photonic cluster states demonstrated recently [42, 247]. In order to determine how many photons are contributing to the quasi-coherent states here, by comparing our experimental results to a photon-truncated theoretical model, we see that at least 3 photons are needed to explain our results. We estimate that these three-photon states occur with a rate of about 5 kHz in our experiment.

6.5 Conclusions

We have shown approximate synthesis of continuous-wave coherent states of light from a quantum dot-based single-photon source, using a simple optical setup with a free-space delay loop. The underlying mechanism is repetitive single-photon addition [191, 202, 204] to an ever-growing number-state superposition, and can be tuned by changing photon distinguishability. A difference of the artificial coherent states here to conventional coherent light is that the photons of the artificial coherent state are correlated with others separated by multiples of the loop delay, this is typical for systems with time-delayed feedback [254] including lasers [255, 256]. This quantum entanglement becomes accessible if an ordered (pulsed) stream of single photons is used, and enables production of linear cluster states which has been realized recently [42, 247], and feed-forward or fast modula-

tors [246,257–259] can be used to produce even more complex quantum states. We want to add that also lasers produce only approximately coherent states with entanglement of the stimulated photons via the gain medium [260–263] which is in practice inaccessible due to the impossibility of monitoring every quantum interaction in the system [264]. From this quantum entanglement arises complexity, therefore we had to use algorithmic modelling in order to produce a theoretical prediction of the output state; this is not surprising because it is known to be computationally hard to calculate quantum interference with many beam splitters (including loop setups such as the one investigated here) and many photons in Fock states, possibly lying beyond the P complexity class [36,41]. It would be an interesting goal to develop rigorous entanglement (length) witnesses that can also be applied to continuous and random photon streams such as here, explore possibilities for time-bin encoded tensor networks [265,266] or quantum metrology [267], or to entangle the photons in a $d > 1$ -dimensional topology [268,269]. A natural question is if other quantum states of light, in particular quadrature squeezed light, can be produced in a similar way, unfortunately, those light states are not resilient against loss compared to coherent states, rendering this far more challenging.

6.6 Appendix

6.6.1 The two-photon picture

In this section, we derive expressions for $g_{VH}^{(2)}(\tau)$ and $g_{HH}^{(2)}(\tau)$ presented in the main text. Limiting the description to two distinguishable photons (see main text), we first describe the full two-photon state created from the single-photon stream by the delay loop. Later, we derive the polarization-postselected correlation functions. Finally, we describe how we include the finite lifetime of the single-photon source, as well as imperfections such as quantum dot blinking and photon loss in the delay loop. Later, in section 6.6.2 we will discuss indistinguishable photons and the effect of photon bunching by the Hong-Ou-Mandel effect.

A single photon entering the loop setup (with the round-trip delay R) shown in Fig. 6.1 at time t is brought into a quantum superposition which becomes increasingly complex with the number of round-trips r . The single-photon state $|\Psi_1\rangle$ can be written in terms of photon creation operators Q^\dagger acting on the vacuum as $|\Psi_1\rangle = Q^\dagger(r, t)|0\rangle$, where $Q^\dagger(r, t)$ depends on the number of round-trips:

$$Q^\dagger(r, t) = \begin{cases} \frac{1}{\sqrt{2}}V_{D,t}^\dagger + \frac{1}{\sqrt{2}}H_{B,t}^\dagger, & r = 0, \\ \frac{1}{\sqrt{2}}V_{D,t}^\dagger + \frac{1}{2}(H_{D,t+R}^\dagger + V_{B,t+R}^\dagger), & r = 1, \\ \frac{1}{\sqrt{2}}V_{D,t}^\dagger + \frac{1}{2}H_{D,t+R}^\dagger \\ + \frac{1}{\sqrt{2}} \left[\sum_{s \geq 2}^r \left(\frac{-1}{\sqrt{2}} \right)^s H_{D,t+s \cdot R}^\dagger - \left(\frac{-1}{\sqrt{2}} \right)^r V_{B,t+r \cdot R}^\dagger \right], & r \geq 2. \end{cases} \quad (6.5)$$

Here, for instance, $V_{D,t}^\dagger$ is the photon creation operator for a V -polarized photon in mode D at time t . In each round trip, a photon at position B is brought into quantum superposition by WP2, and the H -polarized component is transmitted from the loop by the polarizing beam splitter (PBS) to the HBT detection setup, this results in an infinite tree-like structure indicated in Fig. 6.6 below.

We assume that the input light is a perfect but random single-photon stream, where the delay between two photons is $\Delta t \neq 0$, and the HBT setup post-selects two-photon detection events from this stream. In general, this (detected) two-photon state can be written as

$$|\Psi_2\rangle = \sum_{\Delta t \neq 0} Q^\dagger(r_1, t) \otimes Q^\dagger(r_2, t + \Delta t)|0\rangle. \quad (6.6)$$

Since only photons in spatial mode D are detected, we ignore other photons and leave out the spatial label from now on. In this section, we assume a perfect single-photon source and no loss in the delay loop.

6.6.1.1 Detection of VH correlations

Working out Eq. (6.6) explicitly and post-selecting on terms containing one V and one H photon, we obtain

$$|\Psi_{VH}\rangle = \frac{1}{2} \sum_{\Delta t \neq 0} \left[\frac{1}{\sqrt{2}}V_t^\dagger H_{t+\Delta t+R}^\dagger + V_t^\dagger \sum_{r_2 \geq 2} \left(\frac{-1}{\sqrt{2}} \right)^{r_2} H_{t+\Delta t+r_2 \cdot R}^\dagger \right. \\ \left. + \frac{1}{\sqrt{2}}V_{t+\Delta t}^\dagger H_{t+R}^\dagger + V_{t+\Delta t}^\dagger \sum_{r_1 \geq 2} \left(\frac{-1}{\sqrt{2}} \right)^{r_1} H_{t+r_1 \cdot R}^\dagger \right] |0\rangle. \quad (6.7)$$

Now, we consider that V photons start the time-correlated single-photon counting apparatus at time $t = 0$, therefore we require that in the first two terms $t = 0$ and in the last two terms $t + \Delta t = 0$. Obviously, only photons with $\Delta t = z \cdot R, z \in \mathbb{Z}$ are correlated by the loop, the rest is uncorrelated and contributes to the correlation function as $g_{VH}^{(2)}(\tau \neq z \cdot R) = 1$. Due to symmetry between r_1 and r_2 , we see that the final state is just a weighted superposition of single-photon streams shifted with respect to each other by a time $r_2 \cdot R, r_2 \in \mathbb{N}$:

$$|\Psi_{VH}\rangle = \sum_{\Delta t \neq 0} V^\dagger \left[\frac{1}{\sqrt{2}} H_{R+\Delta t}^\dagger + \sum_{r_2 \geq 2} \left(\frac{-1}{\sqrt{2}} \right)^{r_2} H_{r_2 \cdot R + \Delta t}^\dagger \right] |0\rangle. \quad (6.8)$$

Evaluating the state for individual data points of $g_{VH}^{(2)}(\tau)$ for fixed $\tau = \mu \cdot R$, we obtain for each μ an analytical expression (normalized by $g_{VH}^{(2)}(\pm\infty) = 1$), depending on whether the photons are correlated by the loop:

$$g_{VH}^{(2)}(\tau = \mu \cdot R) = \begin{cases} \sum_{z=1} 2^{-z} - 2^{-\mu} = 1 - 2^{-\mu} & \text{for } \mu = m \in \mathbb{N}, \\ \sum_{z=1} 2^{-z} = 1 & \text{else.} \end{cases} \quad (6.9)$$

By summation over time we obtain the full form for $g_{VH}^{(2)}(\tau)$

$$g_{VH}^{(2)}(\tau) = \sum_{\mu} g_{VH}^{(2)}(\tau = \mu \cdot R) \delta(\tau - \mu \cdot R) = 1 - \sum_{m \in \mathbb{N}} 2^{-m} \delta(\tau - m \cdot R). \quad (6.10)$$

6.6.1.2 Detection of HH correlations

If both detectors detect H -polarized photons, all detected photons must have come from the loop. We can post-select H -polarized photons from Eq. (6.6) and write the two-photon (not normalized) state using $t' = t + R$ as

$$|\Psi_{HH}\rangle = \frac{1}{2} \sum_{\Delta t \neq 0} \sum_{r_1 \geq 1} \sum_{r_2 \geq 1} \left(\frac{-1}{\sqrt{2}} \right)^{r_1+r_2} H_{t'+(r_1-1) \cdot R}^\dagger H_{t'+\Delta t+R(r_2-1)}^\dagger |0\rangle. \quad (6.11)$$

We again consider that photons from the single-photon stream separated by $\Delta t = z \cdot R$ are correlated by the loop, and coincidence clicks are recorded with time delay $\tau = m \cdot R, m \in \mathbb{Z}$. This leads to the condition $z = r_1 + r_2 \pm m$. For normalization of the second-order correlation function, we require the coincidence probability for photon delays different than the loop delay. We define $0 < \epsilon < 1$ and $z' = z + \epsilon$ and $m' = m + \epsilon$ and assume the conditions as before. We start the calculation of $g^{(2)}(\tau)$ by considering correlations at $\tau = \mu \cdot R$ for loop-correlated photons ($\mu = m$), which results in

$$g_{\text{cor}}^{(2)}(\tau = \mu \cdot R) = \sum_{z \neq 0} \sum_{r_1 \geq 1} \sum_{r_2 \geq 1} \frac{\langle \Psi_{HH}(r_1, r_2, \Delta t) | \Psi_{HH} \rangle}{\langle \Psi_{HH} | \Psi_{HH} \rangle} \cdot \delta(z - r_1 + r_2 \pm \mu). \quad (6.12)$$

The state $|\Psi_{HH}(r_1, r_2, \Delta t)\rangle$ is a superposition of two photons with fixed roundtrips r_1 and r_2 and fixed Δt (summand in Eq. (6.11)). Similarly, uncorrelated photons contribute to the correlations only if $\mu = m' \neq m$ (i.e. $\epsilon \neq 0$):

$$g_{\text{uncor}}^{(2)}(\tau = \mu \cdot R) = \sum_{z \in \mathbb{Z}} \sum_{r_1 \geq 1} \sum_{r_2 \geq 1} \frac{\langle \Psi_{HH}(r_1, r_2, \Delta t) | \Psi_{HH} \rangle}{\langle \Psi_{HH} | \Psi_{HH} \rangle} \cdot \delta(z - r_1 + r_2 \pm \mu). \quad (6.13)$$

The only difference between the equations above is in the summation over z . Since we deal with a single-photon source which implies $\Delta t \neq 0$, the sum in Eq. (6.12) must not include $z = 0$, while this is naturally satisfied in Eq. (6.13) where we can sum over all integer numbers \mathbb{Z} .

Polarization post-selection is a non-unitary operation, therefore the state and also the resulting correlations are not normalized. Hence, we follow the usual normalization procedure, i.e., we normalize by the uncorrelated correlations $g_{\text{uncor}}^{(2)}(\tau = \mu \cdot R) = 1$. Moreover, this choice also helps to simplify the infinite series, where the double summation over r_1 and r_2 can be evaluated and we obtain for fixed μ

$$g_{HH}^{(2)}(\tau = \mu \cdot R) = \begin{cases} \frac{g_{\text{cor}}^{(2)}(\tau = \mu \cdot R)}{g_{\text{uncor}}^{(2)}(\tau = \mu \cdot R)} = 1 - 2 \left(\frac{1}{2}\right)^{|\mu|} \sum_{r_1 \geq 1} 2^{-2r_1} & \text{for } \mu = m \\ = 1 - \frac{2}{3} \left(\frac{1}{2}\right)^{|\mu|} & \\ \frac{g_{\text{uncor}}^{(2)}(\tau = \mu \cdot R)}{g_{\text{uncor}}^{(2)}(\tau = \mu \cdot R)} = 1, & \text{for } \mu \neq m, \end{cases} \quad (6.14)$$

where the sum gives a factor of $1/3$. We then obtain the full, loop-loss free ideal correlation function

$$g_{HH}^{(2)}(\tau) = \sum_{\mu} g_{HH}^{(2)}(\tau = \mu \cdot R) \delta(\tau - \mu \cdot R) = 1 - \frac{2}{3} \sum_{m \in \mathbb{Z}} \left(\frac{1}{2}\right)^{|m|} \delta(\tau - m \cdot R). \quad (6.15)$$

6.6.1.3 Relation to source correlations

As written in the main text, we take the finite quantum dot lifetime and blinking into account by the single-photon source correlation function $g_{3L}^{(2)}(\tau)$ [249] in Eq. (6.1). In order to include this in the model, we replace the δ -function in Eqs. (6.10) and (6.15) by the source correlation function like

$$\delta(\tau - m \cdot R) \rightarrow \exp\left(-\frac{|\tau - m \cdot R|}{\tau_r}\right) \rightarrow \left(1 - g_{3L}^{(2)}(\tau - m \cdot R)\right).$$

The first replacement would include only the finite lifetime, while the second includes also blinking. We obtain (note that we here and in the following re-define $g_{VH}^{(2)}(\tau)$ and $g_{HH}^{(2)}(\tau)$ as we develop the model):

$$g_{VH}^{(2)}(\tau) = 1 - \frac{1}{2} \sum_{m > 0} \left(\frac{1}{2}\right)^m \left(1 - g_{3L}^{(2)}(\tau - m \cdot R)\right) \quad (6.16)$$

and

$$g_{HH}^{(2)}(\tau) = 1 - \frac{2}{3} \sum_{m \in \mathbb{Z}} \left(\frac{1}{2}\right)^{|m|} \left(1 - g_{3L}^{(2)}(\tau - m \cdot R)\right). \quad (6.17)$$

6.6.1.4 Loss in the delay loop

Understanding the effects of optical loss in the delay loop is essential for correct modelling of the produced quantum state of light. In order to achieve this, we define the loop transmission as η_L and incorporate it in the two-photon state of Eq. (6.8) for each round trip simply by replacing $\sqrt{1/2}$ by $\sqrt{\eta_L/2}$:

$$|\Psi_{VH}\rangle = \sum_{\Delta t \neq 0} V^\dagger \left[\sqrt{\eta_L/2} H_{R+\Delta t}^\dagger + \sum_{r_2 \geq 2} \left(-\sqrt{\eta_L/2}\right)^{r_2} H_{r_2 \cdot R + \Delta t}^\dagger \right] |0\rangle. \quad (6.18)$$

After this, the correlation function $g_{VH}^{(2)}(\tau = \mu \cdot R)$ in Eq. (6.9) has to be re-normalized for each μ

$$g_{VH}^{(2)}(\tau = \mu \cdot R) = \begin{cases} 1 - \left(\frac{\eta_L}{2}\right)^\mu = 1 - \left(\frac{\eta_L}{2}\right)^\mu & \text{for } \mu = m \in \mathbb{N}, \\ 1 & \text{else.} \end{cases} \quad (6.19)$$

Similar as before, we obtain the full $g_{VH}^{(2)}(\tau)$ by adding it up for all μ , and, after inserting $g_{3L}^{(2)}(\tau)$ we obtain

$$g_{VH}^{(2)}(\tau) = 1 - \sum_{m>0} \left(\frac{\eta_L}{2}\right)^m \left(1 - g_{3L}^{(2)}(\tau - m \cdot R)\right). \quad (6.20)$$

Analogously, in order to include loop loss in $g_{HH}^{(2)}(\tau)$, we first replace in $|\Psi_{HH}\rangle$ (Eq. (6.11)) $\sqrt{1/2}$ by $\sqrt{\eta_L/2}$. This change equally affects $g_{\text{cor}}^{(2)}(\tau = \mu \cdot R)$ and $g_{\text{uncor}}^{(2)}(\tau = \mu \cdot R)$, allowing us to again normalize by $g_{\text{uncor}}^{(2)}(\tau = \mu \cdot R)$. In analogy to Eq. (6.14) we obtain

$$g_{HH}^{(2)}(\tau = \mu \cdot R) = \begin{cases} \frac{g_{\text{cor}}^{(2)}(\tau = \mu \cdot R)}{g_{\text{uncor}}^{(2)}(\tau = \mu \cdot R)} = 1 - 2 \left(\frac{\eta_L}{2}\right)^{|\mu|} \sum_{r_1 \geq 1} \left(\frac{\eta_L}{2}\right)^{2r_1} \\ = 1 - \frac{2\eta_L}{4 - \eta_L^2} \left(\frac{\eta_L}{2}\right)^{|\mu|}, & \text{for } \mu = m \\ \frac{g_{\text{uncor}}^{(2)}(\tau = \mu \cdot R)}{g_{\text{uncor}}^{(2)}(\tau = \mu \cdot R)} = 1, & \text{for } \mu \neq m, \end{cases} \quad (6.21)$$

and finally complete expression for $g_{HH}^{(2)}(\tau)$ including loop loss:

$$g_{HH}^{(2)}(\tau) = 1 - \frac{2\eta_L}{4 - \eta_L^2} \sum_{m \in \mathbb{Z}} \left(\frac{\eta_L}{2}\right)^{|m|} \left(1 - g_{3L}^{(2)}(\tau - m \cdot R)\right). \quad (6.22)$$

Finally, based on the experimental observation that $g_{HH}^{(2)}(\tau)$ is only for $\tau = 0$ sensitive to multi-photon quantum interference, we explicitly include $g_{HH}^{(2)}(0)$ and arrive at Eq. (6.4) of the main text. We explain the numeric calculation of $g_{HH}^{(2)}(0)$ in the next section.

6.6.2 Simulation details

Calculation of $g_{HH}^{(2)}(0)$ for indistinguishable photons is complex due to multi-photon quantum interference, we accomplish this by a computer simulation that iteratively calculates the evolution of H -polarized photons in the experiment in Fig. 6.1. Because we aim to simulate and tune quantum interference at WP2 by misaligning the delay loop, we introduce two spatial bases for the description of spatially separated photons on WP2. The first basis $\{H, V\}_S$ describes the incident photons and, because H -polarized photons are only detected after at least one round-trip, also after the first round trip; while $\{H, V\}_L$ is the basis used to represent the state after the second round trip. Below, the spatial mode of polarized photons is stressed by its subscript.

In the simulation, we assume a perfect single-photon source continuously emitting H -polarized photons with mutual delay of $\Delta t = R$, each photon corresponds to $|\Psi\rangle_{\text{in}}$ in the flow chart of the algorithm in Fig. 6.6. WP1 set to 22.5° transforms each H -polarized photon to $\frac{1}{\sqrt{2}}(|H_S\rangle + |V_S\rangle)$, the V_S mode is then erased, while the H_S mode is transformed by the PBS from input A to output B and enters the (initially empty) optical loop. The

H mode in the loop is then transformed on WP2 (22.5°) into $\frac{1}{\sqrt{2}}(|H_S\rangle + |V_S\rangle)$, arrives at time R at port C of the PBS and is transformed from the $\{H, V\}_S$ to the $\{H, V\}_L$ basis. At the same time, the next photon from input A arrives at the PBS and its H -polarized part is sent to the loop, while outgoing photons in port D are sent to the HBT detection setup (Fig. 6.1 in the main text), where different ports D in Fig. 6.6 correspond to different time bins.

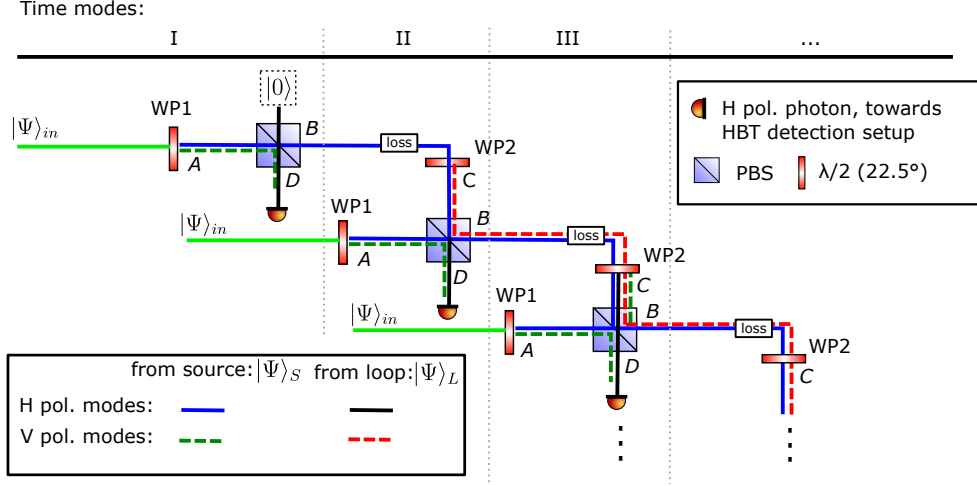


Figure 6.6: Flow chart of the computer algorithm to calculate $g_{HH}^{(2)}(0)$. It is an unfolded version of the real experiment where photons in mode D are sent to the HBT detection setup, each of these ports corresponds to a different time mode.

In order to model the continuous time-averaged measurements, we have to create a stable photonic field in the initially empty delay loop. In Fig. 6.7 we show how the average photon number \bar{n} and $g_{HH}^{(2)}(0)$ evolve with the number of round trips. We observe initial fluctuations in both parameters and very good convergence from 20 round trips on, which we use for all calculations in this paper.

6.6.2.1 Quantum interference at waveplate WP2 in the delay loop

As explained in the main text, this waveplate leads to quantum interference and Hong-Ou-Mandel photon bunching, not only of two photons but also of higher photon number states. In particular to also model partially distinguishable photons, the effects of WP2 has to be modelled carefully in the computer simulation. We define an h -photon Fock state of H -polarized photons in spatial mode S by $|0, h\rangle_S$ and an v -photon Fock state of V -polarized photons in the L -mode by $|v, 0\rangle_L$. If the photons are completely *distinguishable* (wave-function overlap $M = 0$), the general WP2 transformation is

$$\begin{aligned}
 |0, h\rangle_S \otimes |v, 0\rangle_L \xrightarrow[M=0]{\text{WP2}(22.5^\circ)} & \frac{1}{\sqrt{v!}\sqrt{h!}} \left(\frac{1}{\sqrt{2}}\right)^{v+h} \sum_{j=0}^h \binom{h}{j} (V_S^\dagger)^j (H_S^\dagger)^{h-j} |0\rangle \\
 & \otimes \sum_{k=0}^v \binom{v}{k} (-V_L^\dagger)^k (H_L^\dagger)^{v-k} |0\rangle.
 \end{aligned} \tag{6.23}$$

The photons are individually transformed in 2-dimensional subspaces of Hilbert space and do not interfere.

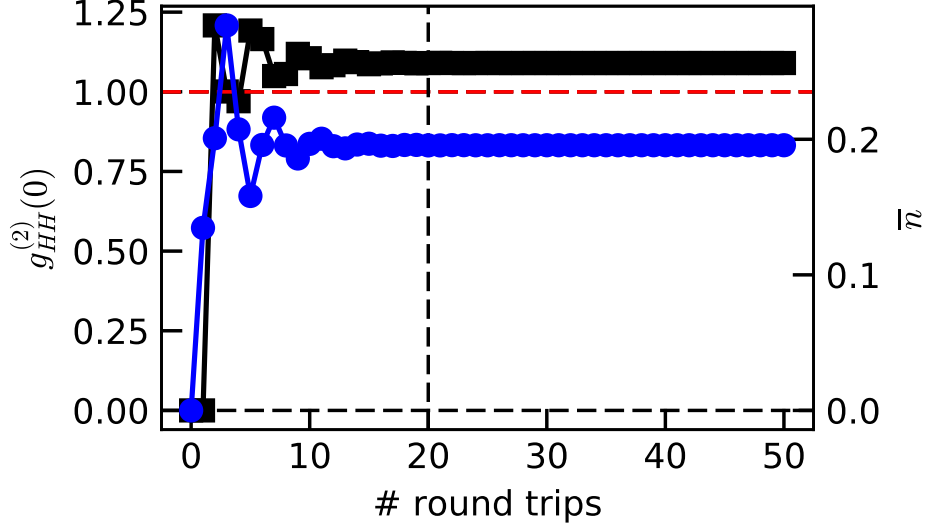


Figure 6.7: Correlation $g_{HH}^{(2)}(0)$ (black) and average photon number \bar{n} (blue) as a function of the number of round trips for perfectly indistinguishable photons ($M = 1$) and experimental round-trip loss $\eta_L = 0.9$. The vertical line shows our choice of 20 round trips where the field is sufficiently converged.

On the other hand, quantum interference of completely indistinguishable photons ($M = 1$ and $\{H, V\}_S = \{H, V\}_L$) will lead to photon bunching:

$$|v, h\rangle_L \xrightarrow[M=1]{\text{WP2}(22.5^\circ)} \frac{1}{\sqrt{v!}\sqrt{h!}} \left(\frac{1}{\sqrt{2}}\right)^{v+h} \sum_{k=0}^v \sum_{j=0}^h \binom{v}{k} \binom{h}{j} (-1)^k (V_L^\dagger)^{k+j} |0\rangle \otimes (H_L^\dagger)^{h+v-k-j} |0\rangle \quad (6.24)$$

In general, WP2 transforms a partially indistinguishable state like

$$\sqrt{M} \cdot |v, h\rangle_L + \sqrt{1-M} \cdot |0, h\rangle_S \otimes |v, 0\rangle_L. \quad (6.25)$$

6.6.2.2 Delay loop: Round-trip loss and diffraction

As usual in quantum optics, we model loss in the delay loop by a beam splitter, before WP2, with transmission t and reflection r . Ignoring the empty input port and the dumped output port, this transforms an n -photon input state (single polarization) as

$$|n\rangle \rightarrow \frac{1}{\sqrt{n!}} \sum_{k=0}^n (ir)^{n-k} t^k (a^\dagger)^k |0\rangle. \quad (6.26)$$

Figure 6.8(a) shows simulation results of $g_{HH}^{(2)}(0)$ for distinguishable and indistinguishable photons, as a function of round-trip loss. Both curves approach single-photon correlations for high loss, which is understandable because in this case the delay loop can be neglected. For low loss, $g_{HH}^{(2)}(0)$ depends strongly on distinguishability, this is why we can use this as a measure of quantum interference.

We do not use relay lenses in the free-space delay loop setup, here we investigate diffraction between round trips. In order to estimate the decrease of mode overlap with the number of round trips, we calculate the propagation-dependent M to be $M(z) =$

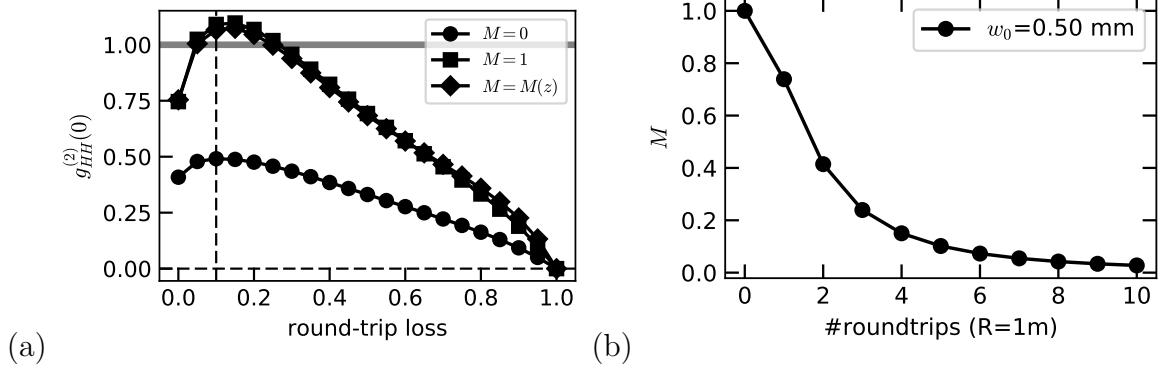


Figure 6.8: Effects of round-trip loss and diffraction. (a) Dependence of $g_{HH}^{(2)}(0)$ on round-trip loss, for the case of fully distinguishable ($M = 0$), indistinguishable ($M = 1$) photons, as well as round-trip dependent indistinguishability due to diffraction. The vertical dashed line points to our experimental round trip loss of ~ 0.1 . (b) Effect of gaussian mode diffraction on the distinguishability or wave function overlap M .

$|\frac{kw_0^2}{kw_0^2+iz}|^2$, where k is the wave number, z the propagation length, and the beam waist $w_0 = 0.50 \pm 0.02$ mm. This leads to considerably reduced distinguishability already after 3 round trips as shown in 6.8(b), however, in combination with the experimental round-trip loss, its effect on $g_{HH}^{(2)}(0)$ is negligible as shown in Fig. 6.8(a).

6.6.3 Visibility measurement

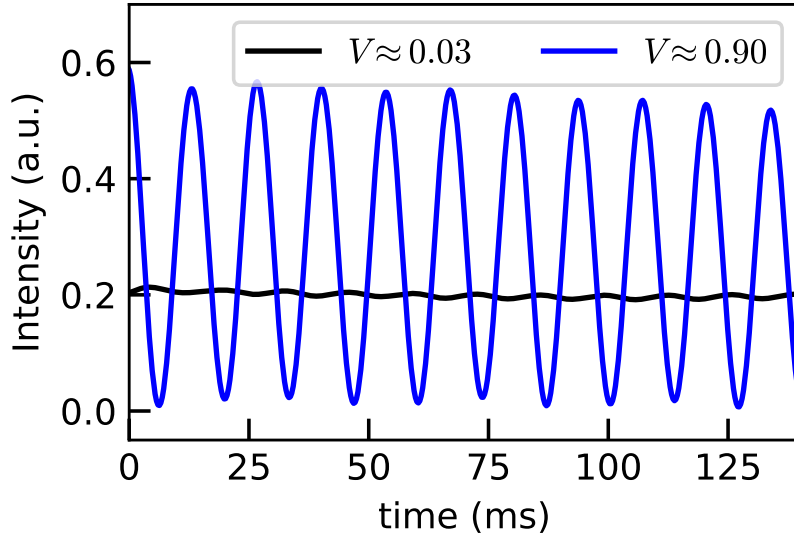


Figure 6.9: Background-noise corrected interference measurements for misaligned (black) and aligned (blue) delay loop, the obtained visibility V is indicated in the legend.

We determine the wave-function overlap M on WP2 by measuring the classical interference visibility $V = \frac{I_{\max} - I_{\min}}{I_{\max} + I_{\min}}$ of laser light sent to the delay loop [97], where I_{\max} and I_{\min}

are maximal and minimal intensity. The relative phase is changed simply by scanning the laser frequency in this unbalanced interferometer. The change in V corresponds directly to the wave-function overlap M at WP2. We repeat this measurement before and after the long correlation measurements in order to determine errors caused by thermal drift of the delay loop during collecting data, which determines the error bars in Fig. 6.5 in the main text. Fig. 6.9 shows examples for visibility measurements with misaligned and aligned delay loop.

6.6.4 How many photons do interfere?

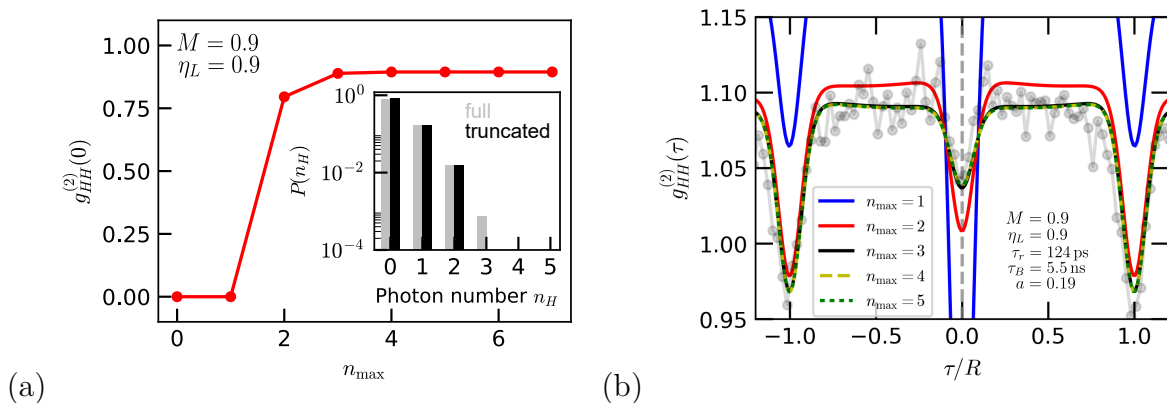


Figure 6.10: Influence of higher photon number states based on truncated computer simulations. (a) Dependence of $g_{HH}^{(2)}(0)$ on the maximum photon number, the inset shows the full (gray) and truncated (black) simulated photon number distribution ($M = 0.9$, $\eta_L = 0.9$). (b) Comparison of differently truncated simulations to the experimental $g_{HH}^{(2)}(\tau)$ data. At least 3 photons are needed to explain the experimental data.

A coherent state contains contributions from a large number of different photon number states, a natural question about our artificial coherent states is therefore: What is the highest photon number state that is required to explain our experimental data? Here we explore this by truncating out computer simulation and comparing to experimental data. Figure 6.10(a) shows simulated $g_{HH}^{(2)}(0)$ for loop transmission $\eta_L = 0.9$ and ideal alignment with $M = 0.9$. This state is now truncated to n_{\max} photons and $g_{HH}^{(2)}(0)$ is calculated, see Fig. 6.10(a). In Fig. 6.10(b) we show the predicted $g_{HH}^{(2)}(\tau)$ based on Eq. (6.4). We clearly see that at least 3 photons are needed to explain our experimental data, but also that discriminating detection of higher number states is impossible with this method because of the differences in $g_{HH}^{(2)}(0)$ become negligible.

This claim is supported by counting simply the number of dips in $g_{HH}^{(2)}(\tau)$ in Fig. 6.3(b), where clearly dips can be observed at $\tau/R = \pm 1$ (corresponding to two photons), $\tau/R = \pm 2$ (three photons), and less clear for four photons.

Finally, we estimate the rate R_n with which n -photon states are produced in our setup. We detect single photons with approximately $R = 150$ kHz, which corresponds to a single-photon rate entering the HBT setup of approximately $R \cdot 2/\eta_d$, where η_d is the single-photon detection efficiency. From our simulation, we derive the n -photon probability $P(n)$, with which we obtain a three-photon rate of ≈ 4.8 kHz, a four-photon rate of ≈ 140 Hz and a 5-photon rate of ≈ 1 Hz.

6.6.5 Properties of the artificial coherent state

In the main text, we showed that the artificial coherent state for $M \approx 1$ approaches the photon number distribution of a weak coherent state and reaches $g^{(2)}(0) \approx 1$. In Fig. 6.11(a), we compare the same states by means of their Wigner function $W(q, p)$, where q and p are dimensionless conjugate variables corresponding to electric field quadratures. Both, the position and the value of the maximum of $W(q, p)$ show that the artificial states are very close to a coherent state. The presence of negative regions in the Wigner function evidences nonclassicality, connected to the ability to create multi-photon entangled states with a delay-loop setup [42].

Coherent states have the unique property of being eigenstates of the annihilation operator \hat{a} . We test this and show the result in Fig. 6.11(b), this shows that the artificial coherent states are very close to being an eigenstate of the annihilation operator, it is almost unchanged by several applications of \hat{a} . On the other hand, performing the same procedure with a thermal state leads to pronounced changes, where the vacuum-state probability decreases strongly and higher number probabilities are increased.

In Fig. 6.11(c) and (d), we compare the density matrices of the exact weak coherent and artificial coherent states. The similarity in the density matrix magnitude, Fig. 6.11(c), supports again the closeness of the states; the difference between both states appears mostly in the phase and only for the higher photon number states with low magnitude, see Fig. 6.11(d).

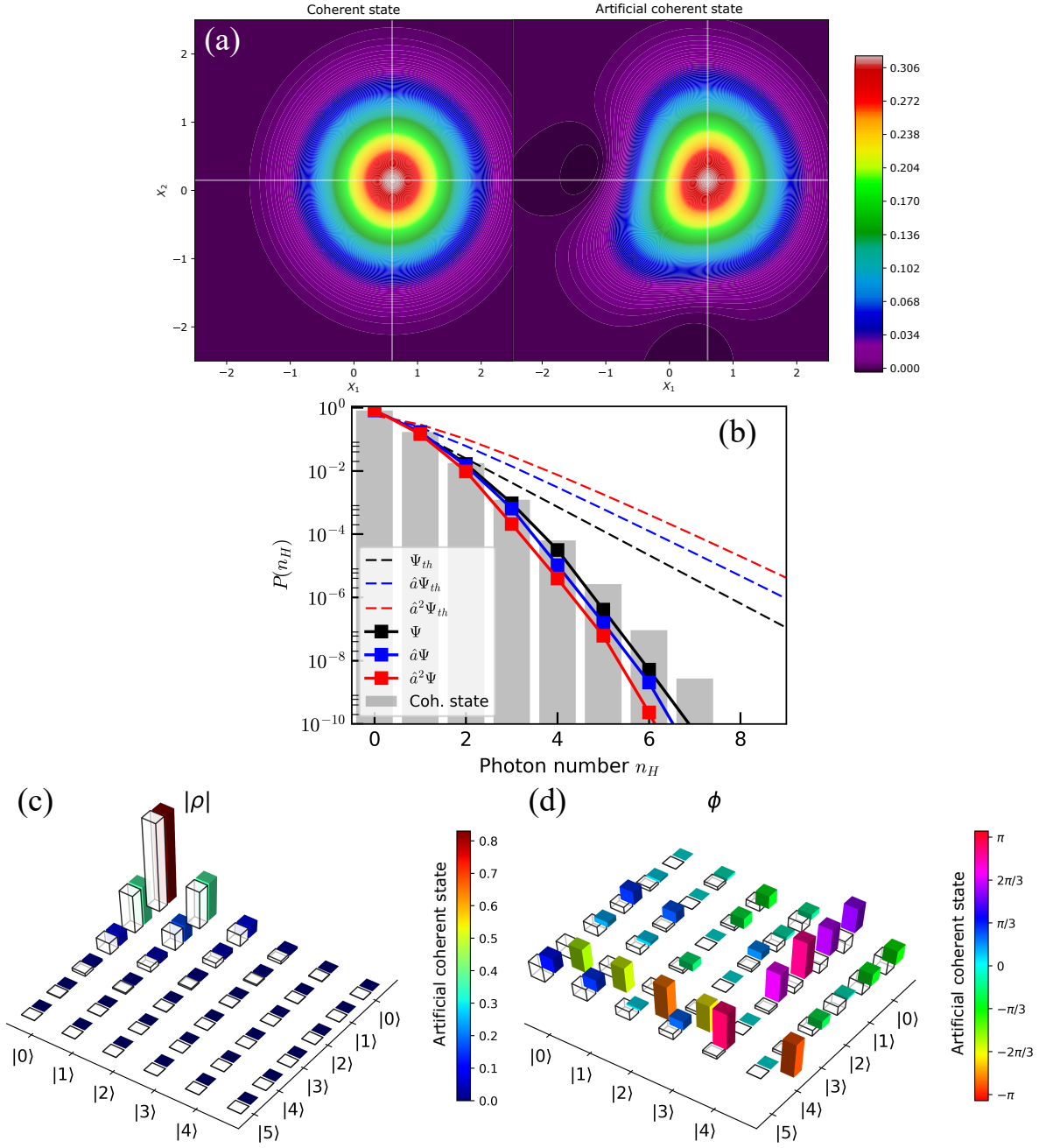


Figure 6.11: Comparison of our artificial coherent state to a weak coherent state with identical mean photon number ($\bar{n} \approx 0.2$). (a) False-color plots of the Wigner function $W(q, p)$ of the artificial coherent state (left panel; $M = 1$, round-trip loss 0.1) and of the weak coherent state (right panel). Both $W(q, p)$ share the position of their maximum (intersection of white lines) as expected. (b) Probability distribution after repeated application of the annihilation operator \hat{a} on the artificial coherent state (Ψ , squares) and a weak thermal state (Ψ_{th} , dashed lines). Bars show the exact coherent state which is an eigenstate of \hat{a} . (c) Magnitude and (d) phase of density matrix elements of the coherent (wireframe boxes) and the artificial coherent states (colored bars).

Bibliography

- [1] Tinsley, J. N., Molodtsov, M. I., Prevedel, R., Wartmann, D., Espigulé-Pons, J., Lauwers, M. & Vaziri, A. Direct detection of a single photon by humans. *Nature Communications* **7**, 12172 (2016).
- [2] Aspect, A., Dalibard, J. & Roger, G. Experimental Test of Bell's Inequalities Using Time-Varying Analyzers. *Phys. Rev. Lett.* **49**, 1804 (1982).
- [3] Bouwmeester, D., Pan, J.-W., Mattle, K., Eibl, M., Weinfurter, H. & Zeilinger, A. Experimental quantum teleportation. *Nature* **390**, 575 (1997).
- [4] Zhong, H.-S., Wang, H., Deng, Y.-H., Chen, M.-C., Peng, L.-C., Luo, Y.-H., Qin, J., Wu, D., Ding, X., Hu, Y., Hu, P., Yang, X.-Y., Zhang, W.-J., Li, H., Li, Y., Jiang, X., Gan, L., Yang, G., You, L., Wang, Z., Li, L., Liu, N.-L., Lu, C.-Y. & Pan, J.-W. Quantum computational advantage using photons. *Science* **370**, 1460 (2020).
- [5] Knill, E., Laflamme, R. & Milburn, G. J. A scheme for efficient quantum computation with linear optics. *Nature* **409**, 46 (2001).
- [6] O'Brien, J. L., Pryde, G. J., White, A. G., Ralph, T. C. & Branning, D. Demonstration of an all-optical quantum controlled-NOT gate. *Nature* **426**, 264 (2003).
- [7] Gasparoni, S., Pan, J. W., Walther, P., Rudolph, T. & Zeilinger, A. Realization of a photonic controlled-NOT gate sufficient for quantum computation. *Phys. Rev. Lett.* **93**, 020504 (2004).
- [8] Raussendorf, R. & Briegel, H. J. A one-way quantum computer. *Phys. Rev. Lett.* **86**, 5188 (2001).
- [9] Nielsen, M. A. Optical quantum computation using cluster states. *Phys. Rev. Lett.* **93**, 040503 (2004).
- [10] Walther, P., Resch, K. J., Rudolph, T., Schenck, E., Weinfurter, H., Vedral, V., Aspelmeyer, M. & Zeilinger, A. Experimental one-way quantum computing. *Nature* **434**, 169 (2005).
- [11] Prevedel, R., Walther, P., Tiefenbacher, F., Böhi, P., Kaltenbaek, R., Jennewein, T. & Zeilinger, A. High-speed linear optics quantum computing using active feed-forward. *Nature* **445**, 65 (2007).
- [12] Rudolph, T. Why i am optimistic about the silicon-photonics route to quantum computing. *APL Photonics* **2**, 030901 (2017).

- [13] Somaschi, N., Giesz, V., De Santis, L., Loredo, J. C., Almeida, M. P., Hornecker, G., Portalupi, S. L., Grange, T., Antón, C., Demory, J., Gómez, C., Sagnes, I., Lanzillotti-Kimura, N. D., Lemaître, A., Auffeves, A., White, A. G., Lanco, L. & Senellart, P. Near-optimal single-photon sources in the solid state. *Nature Photonics* **10**, 340 (2016).
- [14] Senellart, P., Solomon, G. & White, A. High-performance semiconductor quantum-dot single-photon sources. *Nature Nanotechnology* **12**, 1026 (2017).
- [15] Tomm, N., Javadi, A., Antoniadis, N. O., Najer, D., Löbl, M. C., Korsch, A. R., Schott, R., Valentin, S. R., Wieck, A. D., Ludwig, A. & Warburton, R. J. A bright and fast source of coherent single photons. *Nat. Nanotechnol.* **16**, 399 (2021).
- [16] Thomas, S. & Senellart, P. The race for the ideal single-photon source is on. *Nat. Nanotechnol.* **16**, 367 (2021).
- [17] Thomas, S. E., Billard, M., Coste, N., Wein, S. C., Priya, Ollivier, H., Krebs, O., Tazaïrt, L., Harouri, A., Lemaitre, A., Sagnes, I., Anton, C., Lanco, L., Somaschi, N., Loredo, J. C. & Senellart, P. Bright Polarized Single-Photon Source Based on a Linear Dipole. *Phys. Rev. Lett.* **126**, 233601 (2021).
- [18] Snijders, H., Frey, J. A., Norman, J., Post, V. P., Gossard, A. C., Bowers, J. E., Van Exter, M. P., Löffler, W. & Bouwmeester, D. Fiber-Coupled Cavity-QED Source of Identical Single Photons. *Phys. Rev. Appl.* **9**, 031002 (2018).
- [19] Pastier, F., Giesz, V. & Somaschi, N. High-precision method for coupling an optical fiber with a photonic device and implementation microstructure (2022).
- [20] Holewa, P., Sakanas, A., Gür, U. M., Mrowiński, P., Huck, A., Wang, B.-Y., Musiał, A., Yvind, K., Gregersen, N., Syperek, M. & Semenova, E. Bright Quantum Dot Single-Photon Emitters at Telecom Bands Heterogeneously Integrated on Si. *ACS Photonics* **9**, 2273 (2022).
- [21] Laferrière, P., Haffouz, S., Northeast, D. B., Poole, P. J., Williams, R. L. & Dalacu, D. Position-Controlled Telecom Single Photon Emitters Operating at Elevated Temperatures. *Nano Letters* **23**, 962 (2023).
- [22] Morrison, C. L., Rambach, M., Koong, Z. X., Graffitti, F., Thorburn, F., Kar, A. K., Ma, Y., Park, S.-I., Song, J. D., Stoltz, N. G., Bouwmeester, D., Fedrizzi, A. & Gerardot, B. D. A bright source of telecom single photons based on quantum frequency conversion. *Applied Physics Letters* **118**, 174003 (2021).
- [23] Zhou, X., Zhai, L. & Liu, J. Epitaxial quantum dots : a semiconductor launchpad for photonic quantum technologies. *Photonics Insights* **1**, 1 (2023).
- [24] Heyn, C., Stemann, A., Köppen, T., Strelow, C., Kipp, T., Grave, M., Mendach, S. & Hansen, W. Highly uniform and strain-free GaAs quantum dots fabricated by filling of self-assembled nanoholes. *Applied Physics Letters* **94**, 183113 (2009).
- [25] Schweickert, L., Jöns, K. D., Zeuner, K. D., da Silva, S. F. C., Huang, H., Lettner, T., Reindl, M., Zichi, J., Trotta, R., Rastelli, A. & Zwiller, V. On-demand generation of background-free single photons from a solid-state source. *Applied Physics Letters* **112**, 093106 (2018).

- [26] Zhai, L., Nguyen, G. N., Spinnler, C., Ritzmann, J., Löbl, M. C., Wieck, A. D., Ludwig, A., Javadi, A. & Warburton, R. J. Quantum interference of identical photons from remote GaAs quantum dots. *Nature Nanotechnology* **17**, 829 (2022).
- [27] Hong, C. K., Ou, Z. Y. & Mandel, L. Measurement of subpicosecond time intervals between two photons by interference. *Physical Review Letters* **59**, 2044 (1987).
- [28] Santori, C., Fattal, D., Vučković, J., Solomon, G. S. & Yamamoto, Y. Indistinguishable photons from a single-photon device. *Nature* **419**, 594 (2002).
- [29] Lim, C. C. W., Xu, F., Siopsis, G., Chitambar, E., Evans, P. G. & Qi, B. Loss-tolerant quantum secure positioning with weak laser sources. *Phys. Rev. A* **94**, 032315 (2016).
- [30] Reck, M., Zeilinger, A., Bernstein, H. J. & Bertani, P. Experimental realization of any discrete unitary operator. *Phys. Rev. Lett.* **73**, 58 (1994).
- [31] Clements, W. R., Humphreys, P. C., Metcalf, B. J., Kolthammer, W. S. & Walsmley, I. A. Optimal design for universal multiport interferometers. *Optica* **3**, 1460 (2016).
- [32] Aaronson, S. & Arkhipov, A. The Computational Complexity of Linear Optics. *Theory of Computing* **9**, 143 (2013).
- [33] Spring, J. B., Metcalf, B. J., Humphreys, P. C., Kolthammer, W. S., Jin, X.-M., Barbieri, M., Datta, A., Thomas-Peter, N., Langford, N. K., Kundys, D., Gates, J. C., Smith, B. J., Smith, P. G. R. & Walmsley, I. A. Boson Sampling on a Photonic Chip. *Science* **339**, 798 (2012).
- [34] Loredó, J. C., Broome, M. A., Hilaire, P., Gazzano, O., Sagnes, I., Lemaitre, A., Almeida, M. P., Senellart, P. & White, A. G. Boson Sampling with Single-Photon Fock States from a Bright Solid-State Source. *Phys. Rev. Lett.* **118**, 130503 (2017).
- [35] Wang, H., Li, W., Jiang, X., He, Y.-M., Li, Y.-H., Ding, X., Chen, M.-C., Qin, J., Peng, C.-Z., Schneider, C., Kamp, M., Zhang, W.-J., Li, H., You, L.-X., Wang, Z., Dowling, J. P., Höfling, S., Lu, C.-Y. & Pan, J.-W. Toward Scalable Boson Sampling with Photon Loss. *Phys. Rev. Lett.* **120**, 230502 (2018).
- [36] Gard, B. T., Olson, J. P., Cross, R. M., Kim, M. B., Lee, H. & Dowling, J. P. Inefficiency of classically simulating linear optical quantum computing with Fock-state inputs. *Phys. Rev. A* **89**, 022328 (2014).
- [37] Wang, H., Qin, J., Ding, X., Chen, M.-C., Chen, S., You, X., He, Y.-M., Jiang, X., You, L., Wang, Z., Schneider, C., Renema, J. J., Höfling, S., Lu, C.-Y. & Pan, J.-W. Boson Sampling with 20 Input Photons and a 60-Mode Interferometer in a 10^{14} -Dimensional Hilbert Space. *Phys. Rev. Lett.* **123**, 250503 (2019).
- [38] Taballione, C., Correa Anguita, M., de Goede, M., Venderbosch, P., Kassenberg, B., Snijders, H., Kannan, N., Smith, D., Epping, J. P., van der Meer, R., Pinkse, P. W. H., van den Vlekkert, H. & Renema, J. J. 20-Mode Universal Quantum Photonic Processor. *arXiv e-prints* arXiv:2203.01801 (2022). 2203.01801.

- [39] Pont, M., Corrielli, G., Fyrrillas, A., Agresti, I., Carvacho, G., Maring, N., Emeriau, P.-E., Ceccarelli, F., Albiero, R., Ferreira, P. H. D., Somaschi, N., Senellart, J., Sagnes, I., Morassi, M., Lemaitre, A., Senellart, P., Sciarrino, F., Liscidini, M., Belabas, N. & Osellame, R. High-fidelity generation of four-photon GHZ states on-chip. *arXiv e-prints* arXiv:2211.15626 (2022).
- [40] Megidish, E., Shacham, T., Halevy, A., Dovrat, L. & Eisenberg, H. S. Resource Efficient Source of Multiphoton Polarization Entanglement. *Phys. Rev. Lett.* **109**, 080504 (2012).
- [41] Motes, K. R., Gilchrist, A., Dowling, J. P. & Rohde, P. P. Scalable Boson Sampling with Time-Bin Encoding Using a Loop-Based Architecture. *Phys. Rev. Lett.* **113**, 120501 (2014).
- [42] Istrati, D., Pilnyak, Y., Loredó, J. C., Antón, C., Somaschi, N., Hilaire, P., Ollivier, H., Esmann, M., Cohen, L., Vidro, L., Millet, C., Lemaître, A., Sagnes, I., Harouri, A., Lanco, L., Senellart, P. & Eisenberg, H. S. Sequential generation of linear cluster states from a single photon emitter. *Nature Communications* **11**, 5501 (2020).
- [43] Warburton, R. J. Single spins in self-assembled quantum dots. *Nat. Mater.* **12**, 483 (2013).
- [44] Mrowiński, P., Schnauber, P., Gutsche, P., Kaganskiy, A., Schall, J., Burger, S., Rodt, S. & Reitzenstein, S. Directional Emission of a Deterministically Fabricated Quantum Dot–Bragg Reflection Multimode Waveguide System. *ACS Photonics* **6**, 2231 (2019).
- [45] Xu, X., Wu, Y., Sun, B., Huang, Q., Cheng, J., Steel, D. G., Bracker, A. S., Gammon, D., Emary, C. & Sham, L. J. Fast spin state initialization in a singly charged InAs-GaAs quantum dot by optical cooling. *Phys. Rev. Lett.* **99**, 097401 (2007).
- [46] Emary, C., Xu, X., Steel, D. G., Saikin, S. & Sham, L. J. Fast initialization of the spin state of an electron in a quantum dot in the voigt configuration. *Phys. Rev. Lett.* **98**, 047401 (2007).
- [47] Kroner, M., Weiss, K. M., Biedermann, B., Seidl, S., Manus, S., Holleitner, A. W., Badolato, A., Petroff, P. M., Gerardot, B. D., Warburton, R. J. & Karrai, K. Optical detection of single-electron spin resonance in a quantum dot. *Phys. Rev. Lett.* **100**, 156803 (2008).
- [48] Zaporski, L., Shofer, N., Bodey, J. H., Manna, S., Gillard, G., Appel, M. H., Schimpf, C., da Silva, S. F. C., Jarman, J., Delamare, G., Park, G., Haeusler, U., Chekhovich, E. A., Rastelli, A., Gangloff, D. A., Atatüre, M. & Gall, C. L. Ideal refocusing of an optically active spin qubit under strong hyperfine interactions. *Nature Nanotechnology* **18**, 257 (2023).
- [49] Cabrillo, C., Cirac, J. I., García-Fernández, P. & Zoller, P. Creation of entangled states of distant atoms by interference. *Phys. Rev. A* **59**, 1025 (1999).
- [50] Lindner, N. H. & Rudolph, T. Proposal for pulsed On-demand sources of photonic cluster state strings. *Phys. Rev. Lett.* **103**, 113602 (2009).

- [51] Schwartz, I., Cogan, D., Schmidgall, E. R., Don, Y., Gantz, L., Kenneth, O., Lindner, N. H. & Gershoni, D. Deterministic generation of a cluster state of entangled photons. *Science* **354**, 434 (2016).
- [52] Cogan, D., Su, Z.-E., Kenneth, O. & Gershoni, D. Deterministic generation of indistinguishable photons in a cluster state. *Nature Photonics* (2023).
- [53] Coste, N., Fioretto, D., Belabas, N., Wein, S. C., Hilaire, P., Frantzeskakis, R., Gundin, M., Goes, B., Somaschi, N., Morassi, M., Lemaître, A., Sagnes, I., Harouri, A., Economou, S. E., Auffeves, A., Krebs, O., Lanco, L. & Senellart, P. High-rate entanglement between a semiconductor spin and indistinguishable photons arXiv:2207.09881 (2022).
- [54] Kuhlmann, A. V., Houel, J., Brunner, D., Ludwig, A., Reuter, D., Wieck, A. D. & Warburton, R. J. A dark-field microscope for background-free detection of resonance fluorescence from single semiconductor quantum dots operating in a set-and-forget mode. *Rev. Sci. Instrum.* **84**, 073905 (2013).
- [55] Benelajla, M., Kammann, E., Urbaszek, B. & Karrai, K. Physical Origins of Extreme Cross-Polarization Extinction in Confocal Microscopy. *Phys. Rev. X* **11**, 021007 (2021).
- [56] Stoltz, N. G., Rakher, M., Strauf, S., Badolato, A., Lofgreen, D. D., Petroff, P. M., Coldren, L. A. & Bouwmeester, D. High-quality factor optical microcavities using oxide apertured micropillars. *Applied Physics Letters* **87**, 031105 (2005).
- [57] Strauf, S., Stoltz, N. G., Rakher, M. T., Coldren, L. A., Petroff, P. M. & Bouwmeester, D. High-frequency single-photon source with polarization control. *Nat. Photonics* **1**, 704 (2007).
- [58] Bakker, M. P., Barve, A. V., Ruytenberg, T., Löffler, W., Coldren, L. A., Bouwmeester, D. & Van Exter, M. P. Polarization degenerate solid-state cavity quantum electrodynamics. *Phys. Rev. B* **91**, 115319 (2015).
- [59] Bakker, M. P. *Cavity quantum electrodynamics with quantum dots in microcavities*. Ph.D. thesis, Leiden University (2014).
- [60] Norman, J. *Quantum Dot Lasers for Silicon Photonics*. Ph.D. thesis, University of California Santa Barbara (2016).
- [61] Frey, J. *Cavity Polarization Tuning for Enhanced Quantum Dot Interactions*. Ph.D. thesis, University of California Santa Barbara (2019).
- [62] Braun, T., Schneider, C., Maier, S., Igusa, R., Iwamoto, S., Forchel, A., Höfling, S., Arakawa, Y. & Kamp, M. Temperature dependency of the emission properties from positioned In(Ga)As/GaAs quantum dots. *AIP Advances* **4**, 097128 (2014).
- [63] Bakker, M. P., Suntrup, D. J., Snijders, H., Truong, T.-A., Petroff, P. M., van Exter, M. P. & Bouwmeester, D. Monitoring the formation of oxide apertures in micropillar cavities. *Applied Physics Letters* **102**, 101109 (2013).

- [64] Bakker, M. P., Barve, A. V., Zhan, A., Coldren, L. A., van Exter, M. P. & Bouwmeester, D. Polarization degenerate micropillars fabricated by designing elliptical oxide apertures. *Applied Physics Letters* **104**, 151109 (2014).
- [65] Bonato, C., Gudat, J., de Vries, K., Thon, S. M., Kim, H., Petroff, P. M., van Exter, M. P. & Bouwmeester, D. Optical modes in oxide-apertured micropillar cavities. *Optics Letters* **37**, 4678 (2012).
- [66] Adachi, S. *Journal of Applied Physics* **66**, 6030 (1989).
- [67] Vurgaftman, I., Meyer, J. R. & Ram-Mohan, L. R. Band parameters for III–V compound semiconductors and their alloys. *Journal of Applied Physics* **89**, 5815 (2001).
- [68] Sun, Y., Thompson, S. E. & Nishida, T. Physics of strain effects in semiconductors and metal-oxide-semiconductor field-effect transistors. *Journal of Applied Physics* **101**, 104503 (2007).
- [69] Leonard, D., Krishnamurthy, M., Reaves, C. M., Denbaars, S. P. & Petroff, P. M. Direct formation of quantum-sized dots from uniform coherent islands of InGaAs on GaAs surfaces. *Applied Physics Letters* **63**, 3203 (1993).
- [70] Shchukin, V. A., Ledentsov, N. N., Kop'ev, P. S. & Bimberg, D. Spontaneous Ordering of Arrays of Coherent Strained Islands. *Phys. Rev. Lett.* **75**, 2968 (1995).
- [71] Leonard, D., Pond, K. & Petroff, P. M. Critical layer thickness for self-assembled InAs islands on GaAs. *Phys. Rev. B* **50**, 11687 (1994).
- [72] Heinrichsdorff, F., Krost, A., Bimberg, D., Kosogov, A. O. & Werner, P. Self organized defect free InAs/GaAs and InAs/InGaAs/GaAs quantum dots with high lateral density grown by MOCVD. *Applied Surface Science* **123–124**, 725 (1998).
- [73] Kastner, M. A. Artificial Atoms. *Phys. Today* **46**, 24 (1993).
- [74] Klenovský, P., Munzar, D., Křápek, V. & Humlíček, J. Electronic structure of InAs quantum dots with GaAsSb strain reducing layer: Localization of holes and its effect on the optical properties. *Applied Physics Letters* **97**, 203107 (2010).
- [75] Klenovský, P., Hemzal, D., Steindl, P., Zíková, M., Křápek, V. & Humlíček, J. Polarization anisotropy of the emission from type-II quantum dots. *Phys. Rev. B* **92**, 241302 (2015).
- [76] Petrov, M. Y., Ignatiev, I. V., Poltavtsev, S. V., Grelich, A., Bauschulte, A., Yakovlev, D. R. & Bayer, M. Effect of thermal annealing on the hyperfine interaction in InAs/GaAs quantum dots. *Phys. Rev. B* **78**, 045315 (2008).
- [77] Miller, D. A., Chemla, D. S., Damen, T. C., Gossard, A. C., Wiegmann, W., Wood, T. H. & Burrus, C. A. Band-edge electroabsorption in quantum well structures: The quantum-confined stark effect. *Phys. Rev. Lett.* **53**, 2173 (1984).
- [78] Heller, W. & Bockelmann, U. Electric-field effects on excitons in quantum dots. *Phys. Rev. B - Condens. Matter Mater. Phys.* **57**, 6270 (1998).

- [79] Bennett, A. J., Patel, R. B., Skiba-Szymanska, J., Nicoll, C. A., Farrer, I., Ritchie, D. A. & Shields, A. J. Giant Stark effect in the emission of single semiconductor quantum dots. *Appl. Phys. Lett.* **97**, 031104 (2010).
- [80] Finley, J. J., Sabathil, M., Vogl, P., Abstreiter, G., Oulton, R., Tartakovskii, A. I., Mowbray, D. J., Skolnick, M. S., Liew, S. L., Cullis, A. G. & Hopkinson, M. Quantum-confined Stark shifts of charged exciton complexes in quantum dots. *Phys. Rev. B* **70**, 201308(R) (2004).
- [81] Sheng, W. & Leburton, J. P. Anomalous Quantum-Confined Stark Effects in Stacked InAs/GaAs Self-Assembled Quantum Dots. *Phys. Rev. Lett.* **88**, 167401 (2002).
- [82] Huang, H., Csontosová, D., Manna, S., Huo, Y., Trotta, R., Rastelli, A. & Klenovský, P. Electric field induced tuning of electronic correlation in weakly confining quantum dots. *Phys. Rev. B* **104**, 165401 (2021).
- [83] Fry, P. W., Itskevich, I. E., Mowbray, D. J., Skolnick, M. S., Finley, J. J., Barker, J. A., O'Reilly, E. P., Wilson, L. R., Larkin, I. A., Maksym, P. A., Hopkinson, M., Al-Khafaji, M., David, J. P. R., Cullis, A. G., Hill, G. & Clark, J. C. Inverted Electron-Hole Alignment in InAs-GaAs Self-Assembled Quantum Dots. *Phys. Rev. Lett.* **84**, 733 (2000).
- [84] Aberl, J., Klenovský, P., Wildmann, J. S., Martín-Sánchez, J., Fromherz, T., Zallo, E., Humlíček, J., Rastelli, A. & Trotta, R. Inversion of the exciton built-in dipole moment in In(Ga)As quantum dots via nonlinear piezoelectric effect. *Phys. Rev. B* **96**, 045414 (2017).
- [85] Steindl, P., Snijders, H., Westra, G., Hissink, E., Iakovlev, K., Polla, S., Frey, J. A., Norman, J., Gossard, A. C., Bowers, J. E., Bouwmeester, D. & Löffler, W. Artificial coherent states of light by multi-photon interference in a single-photon stream. *Phys. Rev. Lett.* **126**, 143601 (2021).
- [86] Reindl, M., Jöns, K. D., Huber, D., Schimpf, C., Huo, Y., Zwiller, V., Rastelli, A. & Trotta, R. Phonon-Assisted Two-Photon Interference from Remote Quantum Emitters. *Nano Lett.* **17**, 4090 (2017).
- [87] Weber, J. H., Kambs, B., Kettler, J., Kern, S., Maisch, J., Vural, H., Jetter, M., Portalupi, S. L., Becher, C. & Michler, P. Two-photon interference in the telecom C-band after frequency conversion of photons from remote quantum emitters. *Nat. Nanotechnol.* **14**, 23 (2019).
- [88] Schliwa, A., Winkelkemper, M. & Bimberg, D. Few-particle energies versus geometry and composition of $\text{In}_x\text{Ga}_{1-x}\text{As}/\text{GaAs}$ self-organized quantum dots. *Phys. Rev. B* **79**, 075443 (2009).
- [89] Klenovský, P., Steindl, P. & Geffroy, D. Excitonic structure and pumping power dependent emission blue-shift of type-II quantum dots. *Sci. Rep.* **7**, 45568 (2017).
- [90] Snijders, H. J., Kok, D. N., Van De Stolpe, M. F., Frey, J. A., Norman, J., Gossard, A. C., Bowers, J. E., Van Exter, M. P., Bouwmeester, D. & Löffler, W. Extended polarized semiclassical model for quantum-dot cavity QED and its application to single-photon sources. *Phys. Rev. A* **101**, 053811 (2020).

- [91] Heiss, D., Jovanov, V., Bichler, M., Abstreiter, G. & Finley, J. J. Charge and spin readout scheme for single self-assembled quantum dots. *Phys. Rev. B* **77**, 235442 (2008).
- [92] Heiss, D., Jovanov, V., Klotz, F., Rudolph, D., Bichler, M., Abstreiter, G., Brandt, M. S. & Finley, J. J. Optically monitoring electron spin relaxation in a single quantum dot using a spin memory device. *Phys. Rev. B* **82**, 245316 (2010).
- [93] Warburton, R. J., Schäfflein, C., Haft, D., Bickel, F., Lorke, A., Karrai, K., Garcia, J. M., Schoenfeld, W. & Petroff, P. M. Optical emission from a charge-tunable quantum ring. *Nature* **405**, 926 (2000).
- [94] Klenovský, P., Steindl, P., Aberl, J., Zallo, E., Trotta, R., Rastelli, A. & Fromherz, T. Effect of second-order piezoelectricity on the excitonic structure of stress-tuned In(Ga)As/GaAs quantum dots. *Phys. Rev. B* **97**, 245314 (2018). 1805.06825.
- [95] Steindl, P. & Klenovský, P. Dimension-Dependent Phenomenological Model of Excitonic Electric Dipole in InGaAs Quantum Dots. *Nanomaterials* **12**, 719 (2022).
- [96] Ediger, M., Bester, G., Badolato, A., Petroff, P. M., Karrai, K., Zunger, A. & Warburton, R. J. Peculiar many-body effects revealed in the spectroscopy of highly charged quantum dots. *Nature Physics* **3**, 774 (2007).
- [97] Ollivier, H., de Buy Wenniger, I. M., Thomas, S., Wein, S. C., Harouri, A., Coppola, G., Hilaire, P., Millet, C., Lemaître, A., Sagnes, I., Krebs, O., Lanco, L., Loredó, J. C., Antón, C., Somaschi, N. & Senellart, P. Reproducibility of High-Performance Quantum Dot Single-Photon Sources. *ACS Photonics* **7**, 1050 (2020).
- [98] Bayer, M., Ortner, G., Stern, O., Kuther, A., Gorbunov, A. A., Forchel, A., Hawrylak, P., Fafard, S., Hinzer, K., Reinecke, T. L., Walck, S. N., Reithmaier, J. P., Klopff, F. & Schafer, F. Fine structure of neutral and charged excitons in self-assembled In(Ga)As/(Al)GaAs quantum dots. *Phys. Rev. B* **65**, 195315 (2002).
- [99] Huber, D., Lehner, B. U., Csontosová, D., Reindl, M., Schuler, S., Covre Da Silva, S. F., Klenovský, P. & Rastelli, A. Single-particle-picture breakdown in laterally weakly confining GaAs quantum dots. *Phys. Rev. B* **100**, 235425 (2019).
- [100] Bakker, M. P., Snijders, H., Löffler, W., Barve, A. V., Coldren, L. A., Bouwmeester, D. & van Exter, M. P. Homodyne detection of coherence and phase shift of a quantum dot in a cavity. *Optics Letters* **40**, 3173 (2015).
- [101] Steindl, P., Frey, J. A., Norman, J., Bowers, J. E., Bouwmeester, D. & Löffler, W. Cross-polarization extinction enhancement and spin-orbit coupling of light for quantum-dot cavity-QED spectroscopy. *arXiv e-prints* arXiv:2302.05359 (2023).
- [102] Ding, X., He, Y., Duan, Z.-C., Gregersen, N., Chen, M.-C., Unsleber, S., Maier, S., Schneider, C., Kamp, M., Höfling, S., Lu, C.-Y. & Pan, J.-W. On-Demand Single Photons with High Extraction Efficiency and Near-Unity Indistinguishability from a Resonantly Driven Quantum Dot in a Micropillar. *Phys. Rev. Lett.* **116**, 020401 (2016).

- [103] He, Y. M., He, Y., Wei, Y. J., Wu, D., Atatüre, M., Schneider, C., Höfling, S., Kamp, M., Lu, C. Y. & Pan, J. W. On-demand semiconductor single-photon source with near-unity indistinguishability. *Nature Nanotechnology* **8**, 213 (2013).
- [104] Latta, C., Högele, A., Zhao, Y., Vamivakas, A. N., Maletinsky, P., Kroner, M., Dreiser, J., Carusotto, I., Badolato, A., Schuh, D., Wegscheider, W., Atatüre, M. & Imamoglu, A. Confluence of resonant laser excitation and bidirectional quantum-dot nuclear-spin polarization. *Nat. Phys.* **5**, 758 (2009).
- [105] Vamivakas, A. N., Zhao, Y., Lu, C. Y. & Atatüre, M. Spin-resolved quantum-dot resonance fluorescence. *Nat. Phys.* **5**, 198 (2009).
- [106] Kaldewey, T., Kuhlmann, A. V., Valentin, S. R., Ludwig, A., Wieck, A. D. & Warburton, R. J. Far-field nanoscopy on a semiconductor quantum dot via a rapid-adiabatic-passage-based switch. *Nat. Photonics* **12**, 68 (2018).
- [107] Rudakova, N. V., Timofeev, I. V., Vetrov, S. Y. & Lee, W. All-dielectric polarization-preserving anisotropic mirror. *OSA Continuum* **1**, 682 (2018).
- [108] Götte, J. B. & Dennis, M. R. Generalized shifts and weak values for polarization components of reflected light beams. *New J. Phys.* **14**, 073016 (2012).
- [109] Bliokh, K. Y. & Aiello, A. Goos-Hänchen and Imbert-Fedorov beam shifts: An overview. *J. Opt.* **15**, 014001 (2013).
- [110] Töppel, F., Ornigotti, M. & Aiello, A. Goos-Hänchen and Imbert-Fedorov shifts from a quantum-mechanical perspective. *New J. Phys.* **15**, 113059 (2013).
- [111] Merano, M., Aiello, A., Van Exter, M. P. & Woerdman, J. P. Observing angular deviations in the specular reflection of a light beam. *Nat. Photonics* **3**, 337 (2009).
- [112] Aiello, A., Merano, M. & Woerdman, J. P. Duality between spatial and angular shift in optical reflection. *Phys. Rev. A* **80**, 061801(R) (2009).
- [113] Goos, F. & Hänchen, H. Ein neuer und fundamentaler Versuch zur Totalreflexion. *Annalen der Physik* **436**, 333 (1947).
- [114] Imbert, C. Calculation and experimental proof of the transverse shift induced by total internal reflection of a circularly polarized light beam. *Phys. Rev. D* **5**, 787 (1972).
- [115] Fedorov, F. I. To the theory of total reflection. *J. Opt.* **15**, 014002 (2013).
- [116] Hosten, O. & Kwiat, P. Observation of the Spin Hall Effect of Light via Weak Measurements. *Science* **319**, 5864 (2008).
- [117] Bliokh, K. Y., Rodríguez-Fortuño, F. J., Nori, F. & Zayats, A. V. Spin-orbit interactions of light. *Nat. Photonics* **9**, 796 (2015).
- [118] Götte, J. B., Löffler, W. & Dennis, M. R. Eigenpolarizations for giant transverse optical beam shifts. *Phys. Rev. Lett.* **112**, 233901 (2014).

- [119] Bliokh, K. Y. & Bliokh, Y. P. Conservation of angular momentum, transverse shift, and spin hall effect in reflection and refraction of an electromagnetic wave packet. *Phys. Rev. Lett.* **96**, 073903 (2006).
- [120] Xiao, P. Beam reshaping in the occurrence of the Goos-Hänchen shift. *J. Opt. Soc. Am. B* **28**, 1895 (2011).
- [121] Jayaswal, G., Mistura, G. & Merano, M. Observation of the Imbert-Fedorov effect via weak value amplification. *Front. Opt. FiO 2014* **39**, 2266 (2014).
- [122] Yin, X. & Hesselink, L. Goos-Hänchen shift surface plasmon resonance sensor. *Appl. Phys. Lett.* **89**, 261108 (2006).
- [123] Ling, X., Zhou, X., Huang, K., Liu, Y., Qiu, C. W., Luo, H. & Wen, S. Recent advances in the spin Hall effect of light. *Reports Prog. Phys.* **80**, 066401 (2017).
- [124] Schmid, H. M. *et al.* SPHERE/ZIMPOL high resolution polarimetric imager. *Astron. Astrophys.* **619**, A9 (2018).
- [125] Moeller, C. E. & Grieser, D. R. The Observations of Defects in Crossed Glan-Thompson Polarizers. *Appl. Opt.* **8**, 206 (1969).
- [126] King, R. J. & Talim, S. P. Some aspects of polarizer performance. *J. Phys. E*, **4**, 93 (1971).
- [127] Cox, A. J., DeWeerd, A. J. & Linden, J. An experiment to measure Mie and Rayleigh total scattering cross sections. *Am. J. Phys.* **70**, 620 (2002).
- [128] Takubo, Y., Takeda, N., Huang, J. H., Muroo, K. & Yamamoto, M. Precise measurement of the extinction ratio of a polarization analyser. *Meas. Sci. Technol.* **9**, 20 (1998).
- [129] Mei, H. H., Chen, S. J. & Ni, W. T. Suspension of the fiber mode-cleaner launcher and measurement of the high extinction-ratio (10-9) ellipsometer for the Q & A experiment. *J. Phys. Conf. Ser.* **32**, 236 (2006).
- [130] He, D., Xie, B. & Feng, S. Null polarimetry near shot noise limit at 1 Hz. *Rev. Sci. Instrum.* **87**, 043102 (2016).
- [131] Aiello, A. & Woerdman, H. The reflection of a Maxwell-Gaussian beam by a planar surface. *arXiv e-prints* arXiv:0710.1643 (2007).
- [132] Aiello, A. & Woerdman, J. P. Role of beam propagation in Goos-Hänchen and Imbert-Fedorov shifts. *Opt. Lett.* **33**, 1437 (2008).
- [133] Frey, J. A., Snijders, H. J., Norman, J., Gossard, A. C., Bowers, J. E., Löffler, W., Bouwmeester, D., Loer, W. & Bouwmeester, D. Electro-optic polarization tuning of microcavities with a single quantum dot. *Opt. Lett.* **43**, 4280 (2018).
- [134] Phillips, C. L., Brash, A. J., McCutcheon, D. P., Iles-Smith, J., Clarke, E., Royall, B., Skolnick, M. S., Fox, A. M. & Nazir, A. Photon Statistics of Filtered Resonance Fluorescence. *Phys. Rev. Lett.* **125**, 043603 (2020). 2002.08192.

- [135] Bliokh, K. Y., Samlan, C. T., Prajapati, C., Puentes, G., Viswanathan, N. K. & Nori, F. Spin-Hall effect and circular birefringence of a uniaxial crystal plate. *Optica* **3**, 1039 (2016).
- [136] Steindl, P., van der Ent, T., van der Meer, H., Frey, J. A., Norman, J., Bowers, J. E., Bouwmeester, D. & Löffler, W. Resonant two-laser spin-state spectroscopy of a negatively charged quantum dot-microcavity system with a cold permanent magnet. *arXiv e-prints* arXiv:2303.02763 (2023).
- [137] Awschalom, D. D., Hanson, R., Wrachtrup, J. & Zhou, B. B. Quantum technologies with optically interfaced solid-state spins. *Nat. Photonics* **12**, 516 (2018).
- [138] Kimble, H. J. The quantum internet. *Nature* **453**, 1023 (2008).
- [139] Koshino, K., Ishizaka, S. & Nakamura, Y. Deterministic photon-photon $\sqrt{\text{SWAP}}$ gate using a Λ system. *Phys. Rev. A* **82**, 010301(R) (2010).
- [140] Rosenblum, S., Parkins, S. & Dayan, B. Photon routing in cavity QED: Beyond the fundamental limit of photon blockade. *Phys. Rev. A* **84**, 033854 (2011).
- [141] Favero, I., Cassabois, G., Ferreira, R., Darson, D., Voisin, C., Tignon, J., Delalande, C., Bastard, G., Roussignol, P. & Gérard, J. M. Acoustic phonon sidebands in the emission line of single InAs/GaAs quantum dots. *Phys. Rev. B* **68**, 233301 (2003).
- [142] Kuhlmann, A. V., Prechtel, J. H., Houel, J., Ludwig, A., Reuter, D., Wieck, A. D. & Warburton, R. J. Transform-limited single photons from a single quantum dot. *Nat. Commun.* **6**, 8204 (2015).
- [143] Hilaire, P., Millet, C., Loredó, J. C., Antón, C., Harouri, A., Lemaître, A., Sagnes, I., Somaschi, N., Krebs, O., Senellart, P. & Lanco, L. Deterministic assembly of a charged-quantum-dot-micropillar cavity device. *Phys. Rev. B* **102**, 195402 (2020).
- [144] Stockill, R., Stanley, M. J., Huthmacher, L., Clarke, E., Hugues, M., Miller, A. J., Matthiesen, C., Le Gall, C. & Atatüre, M. Phase-Tuned Entangled State Generation between Distant Spin Qubits. *Phys. Rev. Lett.* **119**, 010503 (2017).
- [145] Xu, X., Sun, B., Berman, P. R., Steel, D. G., Bracker, A. S., Gammon, D. & Sham, L. J. Coherent population trapping of an electron spin in a single negatively charged quantum dot. *Nat. Phys.* **4**, 692 (2008).
- [146] Xu, X., Yao, W., Sun, B., Steel, D. G., Bracker, A. S., Gammon, D. & Sham, L. J. Optically controlled locking of the nuclear field via coherent dark-state spectroscopy. *Nature* **459**, 1105 (2009).
- [147] Kroner, M., Weiss, K. M., Biedermann, B., Seidl, S., Holleitner, A. W., Badolato, A., Petroff, P. M., Öhberg, P., Warburton, R. J. & Karrai, K. Resonant two-color high-resolution spectroscopy of a negatively charged exciton in a self-assembled quantum dot. *Phys. Rev. B* **78**, 075429 (2008).
- [148] Androvitsaneas, P., Young, A. B., Schneider, C., Maier, S., Kamp, M., Höfling, S., Knauer, S., Harbord, E., Hu, C. Y., Rarity, J. G. & Oulton, R. Charged quantum dot micropillar system for deterministic light-matter interactions. *Phys. Rev. B* **93**, 241409(R) (2016).

- [149] Androvitsaneas, P., Young, A. B., Lennon, J. M., Schneider, C., Maier, S., Hinchliff, J. J., Atkinson, G. S., Harbord, E., Kamp, M., Höfling, S., Rarity, J. G. & Oulton, R. Efficient Quantum Photonic Phase Shift in a Low Q-Factor Regime. *ACS Photonics* **6**, 429 (2019).
- [150] Adambukulam, C., Sewani, V. K., Stemp, H. G., Asaad, S., Mądzik, M. T., Morello, A. & Laucht, A. An ultra-stable 1.5 T permanent magnet assembly for qubit experiments at cryogenic temperatures. *Rev. Sci. Instrum.* **92**, 085106 (2021).
- [151] Fredricksen, C. J., Nelson, E. W., Muravjov, A. V. & Peale, R. E. High field p-Ge laser operation in permanent magnet assembly. *Infrared Phys. Technol.* **44**, 79 (2003).
- [152] Tokuhara, K., Ohtsu, Y., Ono, F., Yamada, O., Sagawa, M. & Matsuura, Y. Magnetization and torque measurements on Nd₂Fe₁₄B single crystals. *Solid State Commun.* **56**, 333 (1985).
- [153] He, Y. Z. Experimental research on the residual magnetization of a rare-earth permanent magnet for a cryogenic undulator. *Chinese Phys. B* **22**, 074101 (2013).
- [154] Hara, T., Tanaka, T., Kitamura, H., Bizen, T., Maréchal, X., Seike, T., Kohda, T. & Matsuura, Y. Cryogenic permanent magnet undulators. *Phys. Rev. Spec. Top. - Accel. Beams* **7**, 050702 (2004).
- [155] Bayer, M., Stern, O., Kuther, A. & Forchel, A. Spectroscopic study of dark excitons in InGaAs self-assembled quantum dots by a magnetic-field-induced symmetry breaking. *Phys. Rev. B* **61**, 7273 (2000).
- [156] Miyake, T. & Akai, H. Quantum theory of rare-earth magnets. *J. Phys. Soc. Japan* **87**, 041009 (2018).
- [157] Wang, C. & Zhu, M. G. Overview of composition and technique process study on 2:17-type Sm-Co high-temperature permanent magnet. *Rare Met.* **40**, 790 (2021).
- [158] Zhou, J., Skomski, R., Chen, C., Hadjipanayis, G. & Sellmyer, D. Sm-Co-Cu-Ti high-temperature permanent magnets. *Appl. Phys. Lett.* **77**, 1514 (2000).
- [159] Gutfleisch, O. Controlling the properties of high energy density permanent magnetic materials by different processing routes. *J. Phys. D. Appl. Phys.* **33**, R157 (2000).
- [160] Gutfleisch, O., Willard, M. A., Brück, E., Chen, C. H., Sankar, S. G. & Liu, J. P. Magnetic materials and devices for the 21st century: Stronger, lighter, and more energy efficient. *Adv. Mater.* **23**, 821 (2011).
- [161] Duerrschnabel, M., Yi, M., Uestuener, K., Liesegang, M., Katter, M., Kleebe, H. J., Xu, B., Gutfleisch, O. & Molina-Luna, L. Atomic structure and domain wall pinning in samarium-cobalt-based permanent magnets. *Nat. Commun.* **8**, 54 (2017).
- [162] Guo, K., Lu, H., Xu, G. J., Liu, D., Wang, H. B., Liu, X. M. & Song, X. Y. Recent progress in nanocrystalline Sm-Co based magnets. *Mater. Today Chem.* **25**, 100983 (2022).

- [163] Durst, K., Kronmüller, H., Parker, F. T. & Oesterreicher, H. Temperature dependence of coercivity of cellular Sm₂Co₁₇-SmCo₅ permanent magnets. *Phys. Status Solidi* **95**, 213 (1986).
- [164] Liu, L., Liu, Z., Zhang, X., Zhang, C., Li, T., Lee, D. & Yan, A. 2:17 type SmCo magnets with low temperature coefficients of remanence and coercivity. *J. Magn. Magn. Mater.* **473**, 376 (2019).
- [165] Bennett, A. J., Pooley, M. A., Cao, Y., Sköld, N., Farrer, I., Ritchie, D. A. & Shields, A. J. Voltage tunability of single-spin states in a quantum dot. *Nat. Commun.* **4**, 1522 (2013).
- [166] Nakaoka, T., Saito, T., Tatebayashi, J. & Arakawa, Y. Size, shape, and strain dependence of the g factor in self-assembled In(Ga)As quantum dots. *Phys. Rev. B* **70**, 235337 (2004).
- [167] Kaniber, M., Laucht, A., Neumann, A., Villas-Bôas, J. M., Bichler, M., Amann, M. C. & Finley, J. J. Investigation of the nonresonant dot-cavity coupling in two-dimensional photonic crystal nanocavities. *Phys. Rev. B - Condens. Matter Mater. Phys.* **77**, 161303(R) (2008). 0802.2008.
- [168] Suffczyński, J., Dousse, A., Gauthron, K., Lemaître, A., Sagnes, I., Lanco, L., Bloch, J., Voisin, P. & Senellart, P. Origin of the Optical Emission within the Cavity Mode of Coupled Quantum Dot-Cavity Systems. *Phys. Rev. Lett.* **103**, 027401 (2009).
- [169] Atatüre, M., Dreiser, J., Badolato, A., Hoge, A., Karrai, K. & Imamoglu, A. Quantum-Dot Spin-State Preparation with Near-Unity Fidelity. *Science* **312**, 551 (2006).
- [170] Loudon, R. *The Quantum Theory of Light (Oxford Science publications)* (Oxford University Press, USA, 1973), 3rd ed edn.
- [171] Ortner, M. & Coliando Bandeira, L. G. Magpylib: A free Python package for magnetic field computation. *SoftwareX* **11**, 100466 (2020).
- [172] Bowers, R. Magnetic Susceptibility of Copper Metal at Low Temperatures. *Phys. Rev.* **102**, 1486 (1956).
- [173] Sauncy, T., Holtz, M., Brafman, O., Fekete, D. & Finkelstein, Y. Excitation intensity dependence of photoluminescence from narrow <100> and <111> grown In(x)Ga(1-x)As Single Quantum Wells. *Phys. Rev. B* **59**, 5049 (1999).
- [174] Huang, S. & Ling, Y. Photoluminescence of self-assembled InAs/GaAs quantum dots excited by ultraintensive femtosecond laser. *J. Appl. Phys.* **106**, 103522 (2009).
- [175] Lloyd, S. & Braunstein, S. L. Quantum computation over continuous variables. *Phys. Rev. Lett.* **82**, 1784 (1999).
- [176] Bartlett, S. D., Sanders, B. C., Braunstein, S. L. & Nemoto, K. Efficient Classical Simulation of Continuous Variable Quantum Information Processes. *Phys. Rev. Lett.* **88**, 097904 (2002).

- [177] Mari, A. & Eisert, J. Positive wigner functions render classical simulation of quantum computation efficient. *Phys. Rev. Lett.* **109**, 230503 (2012).
- [178] Wang, D., Li, M., Zhu, F., Yin, Z. Q., Chen, W., Han, Z. F., Guo, G. C. & Wang, Q. Quantum key distribution with the single-photon-added coherent source. *Phys. Rev. A* **90**, 062315 (2014).
- [179] Wang, D., Li, M., Guo, G. C. & Wang, Q. An improved scheme on decoy-state method for measurement-device-independent quantum key distribution. *Sci. Rep.* **5**, 15130 (2015).
- [180] Zhu, J. R., Wang, C. Y., Liu, K., Zhang, C. M. & Wang, Q. Decoy-state reference-frame-independent quantum key distribution with the single-photon-added coherent source. *Quantum Inf. Process.* **17**, 294 (2018).
- [181] Chen, J. J., Zhang, C. H., Chen, J. M., Zhang, C. M. & Wang, Q. Improving the performance of decoy-state quantum digital signature with single-photon-added coherent sources. *Quantum Inf. Process.* **19**, 198 (2020).
- [182] Lachman, L., Straka, I., Hloušek, J., Ježek, M. & Filip, R. Faithful Hierarchy of Genuine n -Photon Quantum Non-Gaussian Light. *Phys. Rev. Lett.* **123**, 043601 (2019).
- [183] Chabaud, U., Markham, D. & Grosshans, F. Stellar Representation of Non-Gaussian Quantum States. *Phys. Rev. Lett.* **124**, 063605 (2020).
- [184] Walschaers, M. Non-Gaussian Quantum States and Where to Find Them. *PRX Quantum* **2**, 030204 (2021).
- [185] Lvovsky, A. I., Grangier, P., Ourjoumtsev, A., Parigi, V., Sasaki, M. & Tualle-Brouri, R. Production and applications of non-Gaussian quantum states of light. *arXiv e-prints* arXiv:2006.16985 (2020).
- [186] Wenger, J., Tualle-Brouri, R. & Grangier, P. Non-Gaussian statistics from individual pulses of squeezed light. *Phys. Rev. Lett.* **92**, 153601 (2004).
- [187] Zavatta, A., Viciani, S. & Bellini, M. Quantum-to-classical transition with single-photon-added coherent states of light. *Science* **306**, 660 (2004).
- [188] Zavatta, A., Viciani, S. & Bellini, M. Single-photon excitation of a coherent state: Catching the elementary step of stimulated light emission. *Phys. Rev. A* **72**, 023820 (2005).
- [189] Barbieri, M., Spagnolo, N., Genoni, M. G., Ferreyrol, F., Blandino, R., Paris, M. G., Grangier, P. & Tualle-Brouri, R. Non-Gaussianity of quantum states: An experimental test on single-photon-added coherent states. *Phys. Rev. A* **82**, 063833 (2010).
- [190] Kim, M. S. Recent developments in photon-level operations on travelling light fields. *J. Phys. B At. Mol. Opt. Phys.* **41**, 133001 (2008).
- [191] Marco, B. & Alessandro, Z. Manipulating light states by single-photon addition and subtraction. *Prog. Opt.* **55**, 41 (2010).

- [192] Biagi, N., Francesconi, S., Zavatta, A. & Bellini, M. Photon-by-photon quantum light state engineering. *Prog. Quantum Electron.* **84**, 100414 (2022).
- [193] Parigi, V., Zavatta, A., Kim, M. & Bellini, M. Probing quantum commutation rules by addition and subtraction of single photons to/from a light field. *Science* **317**, 1890 (2007).
- [194] Gea-Banacloche, J. & Wilson, W. Photon subtraction and addition by a three-level atom in an optical cavity. *Phys. Rev. A* **88**, 033832 (2013).
- [195] Snijders, H., Frey, J. A., Norman, J., Bakker, M. P., Langman, E. C., Gossard, A., Bowers, J. E., Van Exter, M. P., Bouwmeester, D. & Löffler, W. Purification of a single-photon nonlinearity. *Nature Communications* **7**, 12578 (2016).
- [196] Dakna, M., Knöll, L. & Welsch, D. G. Quantum state engineering using conditional measurement on a beam splitter. *Eur. Phys. J. D* **3**, 295 (1998).
- [197] Dakna, M., Knöll, L. & Welsch, D. G. Photon-added state preparation via conditional measurement on a beam splitter. *Opt. Commun.* **145**, 309 (1998).
- [198] Nunn, C. M., Franson, J. D. & Pittman, T. B. Heralding on the detection of zero photons. *Phys. Rev. A* **104**, 033717 (2021).
- [199] Lvovsky, A. I. & Babichev, S. A. Synthesis and tomographic characterization of the displaced Fock state of light. *Phys. Rev. A* **66**, 011801 (2002).
- [200] Agarwal, G. S. & Tara, K. Nonclassical properties of states generated by the excitations on a coherent state. *Phys. Rev. A* **43**, 492 (1991).
- [201] Lee, C. T. Theorem on nonclassical states. *Phys. Rev. A* **52**, 3374 (1995).
- [202] Barnett, S. M., Ferenczi, G., Gilson, C. R. & Speirits, F. C. Statistics of photon-subtracted and photon-added states. *Phys. Rev. A* **98**, 013809 (2018).
- [203] Zavatta, A., Parigi, V. & Bellini, M. Experimental nonclassicality of single-photon-added thermal light states. *Phys. Rev. A* **75**, 052106 (2007).
- [204] Kim, M. S., Park, E., Knight, P. L. & Jeong, H. Nonclassicality of a photon-subtracted Gaussian field. *Phys. Rev. A* **71**, 043805 (2005).
- [205] Dakna, M., Anhut, T., Opatrný, T., Knöll, L. & Welsch, D. G. Generating Schrödinger-cat-like states by means of conditional measurements on a beam splitter. *Phys. Rev. A - At. Mol. Opt. Phys.* **55**, 3184 (1997).
- [206] Hong, C. K. & Mandel, L. Experimental realization of a localized one-photon state. *Phys. Rev. Lett.* **56**, 58 (1986).
- [207] Zhong, H. S., Li, Y., Li, W., Peng, L. C., Su, Z. E., Hu, Y., He, Y. M., Ding, X., Zhang, W., Li, H., Zhang, L., Wang, Z., You, L., Wang, X. L., Jiang, X., Li, L., Chen, Y. A., Liu, N. L., Lu, C. Y. & Pan, J. W. 12-Photon Entanglement and Scalable Scattershot Boson Sampling with Optimal Entangled-Photon Pairs from Parametric Down-Conversion. *Physical Review Letters* **121**, 250505 (2018).

- [208] Gerry, C. C. & Knight Peter L. *Introductory Quantum Optics* (Cambridge University Press, 2005), 3rd edition edn.
- [209] Kaneda, F. & Kwiat, P. G. High-efficiency single-photon generation via large-scale active time multiplexing. *Science Advances* **5**, eaaw8586 (2019).
- [210] Meyer-Scott, E., Prasanna, N., Dhand, I., Eigner, C., Quiring, V., Barkhofen, S., Brecht, B., Plenio, M. B. & Silberhorn, C. Scalable Generation of Multiphoton Entangled States by Active Feed-Forward and Multiplexing. *Phys. Rev. Lett.* **129**, 150501 (2022).
- [211] Arakawa, Y. & Holmes, M. J. Progress in quantum-dot single photon sources for quantum information technologies: A broad spectrum overview. *Appl. Phys. Rev.* **7**, 021309 (2020).
- [212] Ou, Z., Hong, C. & Mandel, L. Relation between input and output states for a beam splitter. *Opt. Commun.* **63**, 118 (1987).
- [213] Larqué, M., Beveratos, A. & Robert-Philip, I. Entangling single photons on a beamsplitter. *European Physical Journal D* **47**, 119 (2008).
- [214] Loredó, J. C., Antón, C., Reznichenko, B., Hilaire, P., Harouri, A., Millet, C., Olivier, H., Somaschi, N., De Santis, L., Lemaître, A., Sagnes, I., Lanco, L., Auffèves, A., Krebs, O. & Senellart, P. Generation of non-classical light in a photon-number superposition. *Nature Photonics* **13**, 803 (2019).
- [215] Crespi, A., Osellame, R., Ramponi, R., Brod, D. J., Galvão, E. F., Spagnolo, N., Vitelli, C., Maiorino, E., Mataloni, P. & Sciarrino, F. Integrated multimode interferometers with arbitrary designs for photonic boson sampling. *Nature Photonics* **7**, 545 (2013).
- [216] Paris, M. G. Displacement operator by beam splitter. *Phys. Lett. A* **217**, 78 (1996).
- [217] Lvovsky, A. I. & Mlynek, J. Quantum-Optical Catalysis: Generating Nonclassical States of Light by Means of Linear Optics. *Phys. Rev. Lett.* **88**, 250401 (2002).
- [218] Bartley, T. J., Donati, G., Spring, J. B., Jin, X. M., Barbieri, M., Datta, A., Smith, B. J. & Walmsley, I. A. Multiphoton state engineering by heralded interference between single photons and coherent states. *Phys. Rev. A* **86**, 043820 (2012).
- [219] Bozzio, M., Vyvlecka, M., Cosacchi, M., Nawrath, C., Seidelmann, T., Loredó, J. C., Portalupi, S. L., Axt, V. M., Michler, P. & Walther, P. Enhancing quantum cryptography with quantum dot single-photon sources. *npj Quantum Inf.* **8**, 104 (2022).
- [220] Dastidar, M. G. & Sarbicki, G. Detecting entanglement between modes of light. *Phys. Rev. A* **105**, 062459 (2022).
- [221] Windhager, A., Suda, M., Pacher, C., Peev, M. & Poppe, A. Quantum interference between a single-photon Fock state and a coherent state. *Opt. Commun.* **284**, 1907 (2011).

- [222] Glauber, R. J. Coherent and incoherent states of the radiation field. *Phys. Rev.* **131**, 2766 (1963).
- [223] Zavatta, A., Parigi, V., Kim, M. S. & Bellini, M. Subtracting photons from arbitrary light fields: Experimental test of coherent state invariance by single-photon annihilation. *New J. Phys.* **10**, 123006 (2008).
- [224] Hanbury Brown, R. & Twiss, R. Q. Correlation between photons in two coherent beams of light. *Nature* **177**, 27 (1956).
- [225] Laiho, K., Dirmeier, T., Schmidt, M., Reitzenstein, S. & Marquardt, C. Measuring higher-order photon correlations of faint quantum light: A short review. *Phys. Lett. A* **435**, 128059 (2022).
- [226] Laiho, K., Avenhaus, M. & Silberhorn, C. Characteristics of displaced single photons attained via higher order factorial moments. *New J. Phys.* **14**, 105011 (2012).
- [227] de Oliveira, F. A. M., Kim, M. S., Knight, P. L. & Buek, V. Properties of displaced number states. *Phys. Rev. A* **41**, 2645 (1990).
- [228] Shen, A., Du, B., Wang, Z. H., Dong, Y., Chen, X. D., Guo, G. C. & Sun, F. W. Indistinguishability-induced classical-to-nonclassical transition of photon statistics. *Phys. Rev. A* **95**, 053851 (2017).
- [229] Meyer-Scott, E., Silberhorn, C. & Migdall, A. Single-photon sources: Approaching the ideal through multiplexing. *Rev. Sci. Instrum.* **91**, 041101 (2020).
- [230] Fischer, K. A., Müller, K., Lagoudakis, K. G. & Vučković, J. Dynamical modeling of pulsed two-photon interference. *New J. Phys.* **18**, 113053 (2016).
- [231] Hanschke, L., Fischer, K. A., Appel, S., Lukin, D., Wierzbowski, J., Sun, S., Trivedi, R., Vučković, J., Finley, J. J. & Müller, K. Quantum dot single-photon sources with ultra-low multi-photon probability. *npj Quantum Inf.* **4**, 43 (2018).
- [232] Seshadreesan, K. P., Olson, J. P., Motes, K. R., Rohde, P. P. & Dowling, J. P. Boson sampling with displaced single-photon Fock states versus single-photon-added coherent states: The quantum-classical divide and computational-complexity transitions in linear optics. *Phys. Rev. A* **91**, 022334 (2015).
- [233] Sun, F. W., Shen, A., Dong, Y., Chen, X. D. & Guo, G. C. Bunching effect and quantum statistics of partially indistinguishable photons. *Phys. Rev. A* **96**, 023823 (2017).
- [234] Parigi, V., Zavatta, A. & Bellini, M. Manipulating thermal light states by the controlled addition and subtraction of single photons. *Laser Phys. Lett.* **5**, 246 (2008).
- [235] Dada, A. C., Santana, T. S., Malein, R. N. E., Koutroumanis, A., Ma, Y., Zajac, J. M., Lim, J. Y., Song, J. D. & Gerardot, B. D. Indistinguishable single photons with flexible electronic triggering. *Optica* **3**, 493 (2016).

- [236] Giesz, V., Somaschi, N., Hornecker, G., Grange, T., Reznichenko, B., De Santis, L., Demory, J., Gomez, C., Sagnes, I., Lemaître, A., Krebs, O., Lanzillotti-Kimura, N. D., Lanco, L., Auffeves, A. & Senellart, P. Coherent manipulation of a solid-state artificial atom with few photons. *Nat. Commun.* **7**, 11986 (2016).
- [237] Javadi, A., Tomm, N., Antoniadis, N. O., Brash, A. J., Schott, R., Valentin, S. R., Wieck, A. D., Ludwig, A. & Warburton, R. J. Cavity-enhanced excitation of a quantum dot in the picosecond regime. *arXiv e-prints* arXiv:2301.13806 (2023).
- [238] Ollivier, H., de Buy Wenniger, I. M., Thomas, S., Wein, S. C., Harouri, A., Coppola, G., Hilaire, P., Millet, C., Lemaître, A., Sagnes, I., Krebs, O., Lanco, L., Loredó, J. C., Antón, C., Somaschi, N. & Senellart, P. Reproducibility of High-Performance Quantum Dot Single-Photon Sources. *ACS Photonics* **7**, 1050 (2020).
- [239] Olson, J. P., Seshadreesan, K. P., Motes, K. R., Rohde, P. P. & Dowling, J. P. Sampling arbitrary photon-added or photon-subtracted squeezed states is in the same complexity class as boson sampling. *Phys. Rev. A* **91**, 022317 (2015).
- [240] Hu, Q., Yusufu, T. & Turek, Y. Quantum state engineering using weak measurements. *Phys. Rev. A* **105**, 022608 (2022).
- [241] Sekatski, P., Sangouard, N., Stobińska, M., Bussi eres, F., Afzelius, M. & Gisin, N. Proposal for exploring macroscopic entanglement with a single photon and coherent states. *Phys. Rev. A* **86**, 060301(R) (2012).
- [242] Lvovsky, A. I., Ghobadi, R., Chandra, A., Prasad, A. S. & Simon, C. Observation of micro-macro entanglement of light. *Nat. Phys.* **9**, 541 (2013).
- [243] Patel, R. B., Bennett, A. J., Cooper, K., Atkinson, P., Nicoll, C. A., Ritchie, D. A. & Shields, A. J. Postselective Two-Photon Interference from a Continuous Nonclassical Stream of Photons Emitted by a Quantum Dot. *Phys. Rev. Lett.* **100**, 207405 (2008).
- [244] Proux, R., Maragkou, M., Baudin, E., Voisin, C., Roussignol, P. & Diederichs, C. Measuring the Photon Coalescence Time Window in the Continuous-Wave Regime for Resonantly Driven Semiconductor Quantum Dots. *Phys. Rev. Lett.* **114**, 067401 (2015).
- [245] Fattal, D., Inoue, K., Vučković, J., Santori, C., Solomon, G. S. & Yamamoto, Y. Entanglement Formation and Violation of Bell's Inequality with a Semiconductor Single Photon Source. *Phys. Rev. Lett.* **92**, 037903 (2004).
- [246] He, Y., Ding, X., Su, Z.-E., Huang, H.-L., Qin, J., Wang, C., Unsleber, S., Chen, C., Wang, H., He, Y.-M., Wang, X.-L., Zhang, W.-J., Chen, S.-J., Schneider, C., Kamp, M., You, L.-X., Wang, Z., Höfling, S., Lu, C.-Y. & Pan, J.-W. Time-Bin-Encoded Boson Sampling with a Single-Photon Device. *Phys. Rev. Lett.* **118**, 190501 (2017).
- [247] Pilnyak, Y., Aharon, N., Istrati, D., Megidish, E., Retzker, A. & Eisenberg, H. S. Simple source for large linear cluster photonic states. *Phys. Rev. A* **95**, 022304 (2017).

- [248] Kitson, S. C., Jonsson, P., Rarity, J. G. & Tapster, P. R. Intensity fluctuation spectroscopy of small numbers of dye molecules in a microcavity. *Phys. Rev. A* **58**, 620 (1998).
- [249] Kurtsiefer, C., Mayer, S., Zarda, P. & Weinfurter, H. Stable Solid-State Source of Single Photons. *Phys. Rev. Lett.* **85**, 290 (2000).
- [250] Davanço, M., Hellberg, C. S., Ates, S., Badolato, A. & Srinivasan, K. Multiple time scale blinking in InAs quantum dot single-photon sources. *Phys. Rev. B* **89**, 161303(R) (2014).
- [251] Pittman, T. B., Jacobs, B. C. & Franson, J. D. Single photons on pseudodemand from stored parametric down-conversion. *Phys. Rev. A* **66**, 042303 (2002).
- [252] Baumgratz, T., Cramer, M. & Plenio, M. B. Quantifying coherence. *Physical Review Letters* **113**, 140401 (2014).
- [253] Hennrich, M., Kuhn, A. & Rempe, G. Transition from Antibunching to Bunching in Cavity QED. *Phys. Rev. Lett.* **94**, 053604 (2005).
- [254] Pototsky, A. & Janson, N. Correlation theory of delayed feedback in stochastic systems below Andronov-Hopf bifurcation. *Physical Review E* **76**, 056208 (2007).
- [255] Holzinger, S., Redlich, C., Lingnau, B., Schmidt, M., von Helversen, M., Beyer, J., Schneider, C., Kamp, M., Höfling, S., Lüdge, K., Porte, X. & Reitzenstein, S. Tailoring the mode-switching dynamics in quantum-dot micropillar lasers via time-delayed optical feedback. *Optics Express* **26**, 22457 (2018).
- [256] Wang, T., Deng, Z. L., Sun, J. C., Wang, X. H., Puccioni, G. P., Wang, G. F. & Lippi, G. L. Photon statistics and dynamics of nanolasers subject to intensity feedback. *Physical Review A* **101**, 023803 (2020).
- [257] Rohde, P. P. Simple scheme for universal linear-optics quantum computing with constant experimental complexity using fiber loops. *Phys. Rev. A* **91**, 012306 (2015).
- [258] Marek, P., Provazník, J. & Filip, R. Loop-based subtraction of a single photon from a traveling beam of light. *Optics Express* **26**, 29837 (2018).
- [259] Švarc, V., Hloušek, J., Nováková, M., Fiurášek, J. & Ježek, M. Feedforward-enhanced Fock state conversion with linear optics. *Opt. Express* **28**, 11634 (2020).
- [260] Mølmer, K. Optical coherence: A convenient fiction. *Phys. Rev. A* **55**, 3195 (1997).
- [261] van Enk, S. J. & Fuchs, C. A. Quantum State of an Ideal Propagating Laser Field. *Phys. Rev. Lett.* **88**, 027902 (2001).
- [262] Gea-Banacloche, J. Some implications of the quantum nature of laser fields for quantum computations. *Phys. Rev. A* **65**, 022308 (2002).
- [263] Pegg, D. T. & Jeffers, J. Quantum nature of laser light. *Journal of Modern Optics* **52**, 1835 (2005).
- [264] Noh, C. & Carmichael, H. J. Disentanglement of Source and Target and the Laser Quantum State. *Phys. Rev. Lett.* **100**, 120405 (2008).

- [265] Lubasch, M., Valido, A. A., Renema, J. J., Kolthammer, W. S., Jaksch, D., Kim, M. S., Walmsley, I. & García-Patrón, R. Tensor network states in time-bin quantum optics. *Phys. Rev. A* **97**, 062304 (2018).
- [266] Dhand, I., Engelkemeier, M., Sansoni, L., Barkhofen, S., Silberhorn, C. & Plenio, M. B. Proposal for Quantum Simulation via All-Optically-Generated Tensor Network States. *Physical Review Letters* **120**, 130501 (2018).
- [267] Peniakov, G., Su, Z.-E., Beck, A., Cogan, D., Amar, O. & Gershoni, D. Towards supersensitive optical phase measurement using a deterministic source of entangled multiphoton states. *Phys. Rev. B* **101**, 245406 (2020).
- [268] Asavanant, W., Shiozawa, Y., Yokoyama, S., Charoensombutamon, B., Emura, H., Alexander, R. N., Takeda, S., Ichi Yoshikawa, J., Menicucci, N. C., Yonezawa, H. & Furusawa, A. Generation of time-domain-multiplexed two-dimensional cluster state. *Science* **366**, 373 (2019).
- [269] Larsen, M. V., Guo, X., Breum, C. R., Neergaard-Nielsen, J. S. & Andersen, U. L. Deterministic generation of a two-dimensional cluster state. *Science* **366**, 369 (2019).

Summary

In this thesis, we explore foundational quantum optics experiments based on cavity quantum electrodynamics with a single self-assembled III-V quantum dot in an optical microcavity. This system has a number of exciting aspects, for instance, it enables high-fidelity single photon production for future quantum applications.

Semiconductor quantum dots (QDs) are nanometer-scale islands of one semiconductor embedded into a different semiconductor of a higher band gap. Due to their small size, QDs have discrete electronic levels, enabling the emission of single photons like in atoms. However, unlike in atoms, the QD energy levels can be fine-tuned by the composition and dimension of the quantum dot, and can afterwards be controlled via external fields. Our self-assembled InGaAs quantum dots were grown by molecular beam epitaxy in the intrinsic region of GaAs *p-i-n* junction, enabling tuning of the QD energy levels via the quantum confined Stark effect. We use this effect to bring a QD transition into resonance with the fundamental resonance of an optical microcavity in which the QD is embedded, or to trap an extra electron in the initially charge-neutral QD. The monolithic optical cavity is formed by two thin-film Bragg mirrors consisting of alternating layers of materials with different refractive indices. The light inside the high-quality optical cavity circulates around 40 000 times in the cavity before it is lost through a mirror, resulting in a near deterministic interaction with the QD and high-efficiency generation and extraction of single photons.

We discuss the quantum-dot devices used in this thesis and their optical characterization in Chapter 2. The device design inspired by samples originally developed for semiconductor lasers has an extra electron-blocking layer below the QDs. This layer supports deterministic and stable QD charging with an extra electron - a spin-based quantum memory. The extra electron in the QD significantly changes the optical selection rules connecting the photon polarization to the electron spin state. For example, if the singly-charged QD is optically excited to the trion state, energy-degenerate circularly polarized transitions emerge. Once placed in an in-plane (Voigt geometry) external magnetic field, electron and trion states are split by the Zeeman effect, and two pairs of orthogonally linearly polarized transitions appear, which we show in Chapter 4.

Studying the electron and trion states using resonant laser spectroscopy requires filtering out of the relatively strong excitation laser, for which we use the cross-polarization technique. The cross-polarization quality is quantified by the cross-polarization extinction ratio, which is limited by the quality of the optical elements. However, recently, it has been discovered that this ratio can be improved by spin-orbit coupling of light upon optical (Fresnel) reflection. In Chapter 3, we identify and explore these effects in our cryogenic confocal microscope and utilize it to improve the purity of the single photons produced by the trion transition of the QD. We find a unique polarization setting where the cross-polarization ratio exceeds the bare-polarizer extinction ratio by a factor 10. We prove that this enhancement is based on compensation of the small ellipticities of our polarizers, while spin-orbit coupling effects are mitigated by single-mode fiber filtering. In order to explore the use of the electron spin as a quantum memory, the spin states

need to be split by an external magnetic field. In Chapter 4, we develop a simple cold permanent magnet assembly delivering almost 0.5 T at cryogenic temperatures. Cooling down our singly-charged QD with this assembly allowed us to perform two-color laser spectroscopy and reveal the QD spin dynamics.

In Chapters 5 and 6, we use a high-quality single-photon source to perform quantum optics experiments that are impossible using classical fields. In our experiments, we use Hong-Ou-Mandel interference to bunch individual photons together and thus produce quantum states of light with a complex structure in photon statistics.

In Chapter 5, we theoretically study single-photon addition to coherent states on an unbalanced beam splitter. The quantum states emerging from one output port of the beam splitter have non-Gaussian properties. These states are interesting for continuous variable quantum computing and communication, however, are notoriously challenging to produce. We propose a simple method based on photon correlations to confirm successful single-photon addition. The two-photon correlations show a universal maximum enabling to maximize the fidelity of the single-photon addition.

Finally, in Chapter 6, we experimentally create artificial coherent states of light from scratch. In fact, we use Hong-Ou-Mandel interference repeatedly in an optical delay loop and manipulate a single-photon stream produced by our QD-cavity source. This allows us to engineer photon-by-photon complex photon-number superposition states with tunable photon number statistics, similar to Poissonian statistics of coherent states. The photon correlations and our models show that the artificial coherent states are more complicated than ordinary coherent states and contain multi-photon entanglement in the form of linear cluster states, a potential resource for universal quantum computing.

Samenvatting

In dit proefschrift verkennen we fundamentele experimenten in kwantumoptica, gebaseerd op kwantumelektrodynamica in een optische trillolte, met een enkele zelfgeassembleerde III-V kwantumdot in een optische microholte. Dit systeem heeft een aantal opwindende aspecten, zoals het mogelijk maken om enkele fotonen te produceren met een hoge fidelity voor toekomstige kwantum toepassingen.

Halfgeleider kwantumdots (QD's, in het Engels vertaald als quantum dots) zijn eilandjes op nanometerschaal van een halfgeleider die is ingebed in een andere halfgeleider met een hogere band gap. Door hun kleine omvang hebben QD's discrete elektronische niveaus, waardoor ze net als atomen afzonderlijke fotonen kunnen uitzenden. Anders dan in atomen kunnen de QD-energieniveaus echter worden afgesteld door de samenstelling en de dimensie van de kwantumdot te veranderen, of via het aanleggen van externe velden. Onze zelfgeassembleerde InGaAs kwantumdots zijn gegroeid in het intrinsieke gebied van de GaAs *p-i-n* junctie door het gebruik van moleculaire bundelepitaxie, waardoor de QD-energieniveaus kunnen worden afgesteld via het zogeheten quantum confined Stark-effect. Wij gebruiken dit effect om een QD-overgang in resonantie te brengen met de fundamentele resonantie van een optische microholte waarin de QD is ingebed, of om een extra elektron te vangen in de aanvankelijk ladingneutrale QD. De monolithische optische holte wordt gevormd door twee dunne film Bragg-spiegels bestaande uit afwisselende lagen materialen met verschillende brekingsindices. Het licht in de hoogwaardige optische holte circuleert ongeveer 40 000 keer in de holte voordat het via een spiegel verloren gaat, wat resulteert in een bijna deterministische interactie met de QD en een zeer efficiënte opwekking en extractie van afzonderlijke fotonen.

Wij bespreken de in dit proefschrift gebruikte kwantumdotapparaten en hun optische karakterisering in hoofdstuk 2. Het ontwerp, geïnspireerd op samples die oorspronkelijk zijn ontwikkeld voor halfgeleiderlasers, heeft een extra elektron blokkerende laag onder de QD's. Door deze extra laag kan de QD worden opgeladen met één elektron op stabiele en deterministische wijze - diens spin werkt als een kwantumgeheugen. Het extra elektron in de QD verandert ook de optische selectieregels die de polarisatie van de fotonen verbinden met de spintoestand aanzienlijk. Bijvoorbeeld: als de enkelvoudig geladen QD optisch wordt geëxciteerd tot de trion-toestand, ontstaan er energie-ontaarde circulair gepolariseerde overgangen. Eenmaal geplaatst in een extern magnetisch veld onder Voigt-geometrie, worden de elektron- en trion-toestand gesplitst door het Zeeman-effect, en verschijnen er twee paren orthogonaal lineair gepolariseerde overgangen, die wij in hoofdstuk 4 laten zien.

Om de elektron- en trion-toestanden te bestuderen met behulp van resonante laserspectroscopie moet de relatief sterke excitatie laser worden uitgefilterd, hiervoor gebruiken wij de kruispolarisatie techniek. De kwaliteit van de kruispolarisatie wordt gekwantificeerd door de extinctieverhouding, die wordt beperkt door de kwaliteit van de optische elementen. Onlangs is echter ontdekt dat deze verhouding kan worden verbeterd door spin-baan koppeling van licht bij optische (Fresnel) reflectie. In hoofdstuk 3 identificeren en onderzoeken we deze effecten in onze cryogene confocale microscoop en gebruiken

we die om de zuiverheid te verbeteren van de losse fotonen geproduceerd door de trion overgang van de QD. Wij vinden een unieke polarisatie-instelling waarbij de extinctieverhouding van een gewone polarisator met een factor 10 overtreft. Wij bewijzen dat deze verbetering gebaseerd is op compensatie van een kleine elliptische component van onze polarisatoren, terwijl spin-baan effecten worden onderdrukt door het filteren met een single-mode glasvezel. Om het gebruik van de elektronenspin als kwantumgeheugen te onderzoeken, moeten de spintoestanden worden gesplitst door een extern magnetisch veld. In hoofdstuk 4 ontwikkelen we een eenvoudige constructie met een koude permanente magneet die bijna 0,5 T levert bij cryogene temperaturen. Door onze enkelvoudig geladen QD met deze constructie af te koelen, konden we laserspectroscopie met twee kleuren uitvoeren en de spin dynamiek van de QD zichtbaar maken.

In de hoofdstukken 5 en 6 gebruiken we een hoogwaardige één-foton bron om kwantum-optica-experimenten uit te voeren die onmogelijk zijn met klassieke velden. In onze experimenten gebruiken wij Hong-Ou-Mandel-interferentie om met individuele fotonen te bundelen en zo kwantumtoestanden van licht te produceren met een complexe fotonstatistiek.

In hoofdstuk 5 bestuderen we theoretisch het toevoegen van één foton aan coherente toestanden op een onevenwichtige bundelsplitser. De kwantumtoestanden die uit één uitvoerpoort van de bundelsplitser komen, hebben niet-Gaussische eigenschappen. Deze toestanden zijn interessant voor kwantumcomputers en -communicatie die gebruik maken van continue variabelen, maar het is een hele uitdaging om deze te produceren. Wij stellen een eenvoudige methode voor, gebaseerd op foton correlaties, om het succes van het experiment te bevestigen. De twee-foton correlaties vertonen een universeel maximum waarmee de fidelity van de één-foton toevoeging kan worden geoptimaliseerd.

Tenslotte creëren we in hoofdstuk 6 experimenteel kunstmatige coherente toestanden van losse fotonen. In feite gebruiken we Hong-Ou-Mandel-interferentie herhaaldelijk in een optische vertraging lus en manipuleren we een stroom van losse fotonen die wordt geproduceerd door onze QD-trilholte-bron. Dit stelt ons in staat om per foton complexe superposities van foton-getallen te maken met afstembare statistiek, vergelijkbaar met Poisson verdeling van voor coherente toestanden. De foton correlaties in combinatie met onze modellen laat zien dat de kunstmatige coherente toestanden veel interessanter zijn dan gewone coherente toestanden en verstrengeling van meerdere fotonen bevat in de vorm van lineaire cluster toestanden, een potentiële bron voor universele kwantumcomputing.

Curriculum Vitae

Petr Steindl was born on 20th January of 1994 in Brno, Czechia. In 2013, after completing his pre-university education at Gymnázium Brno, třída Kapitána Jaroše, he started his studies in Physics at Masaryk University (Brno, Czechia). During his bachelor's studies, he worked under the supervision of Dr. Klenovský specialized in the optical spectroscopy of III-V semiconductor quantum dots with spatially indirect optical transitions.

After his bachelor's graduation in 2016, he joined the two-year Master's program at Masaryk University with a specialization in condensed matter physics and continued his research under Dr. Klenovský with two research topics. In his first year, he was developing metalized tips for tip-enhanced Raman spectroscopy of semiconductor quantum dots and used this method to study the strain distribution around, and defect implantation in, germanium-based quantum dots. Simultaneously and mostly in his second year, he worked on his master's thesis, where he investigated both experimentally and theoretically the optical properties of III-V quantum dots, including exotic antimony-rich material combinations proposed for flash memories. During this year, he collaborated with, visited, and performed experiments at several international institutions (JKU Linz, TU Berlin, IMM-CSIC Madrid). For his work, Petr was awarded with several awards, including the Award of the Czech Minister of Education, Youth, and Sports for outstanding students.

After graduating with a MSc degree in 2018, Petr started the Ph.D. program at Masaryk University on a theoretical research topic with semiconductor quantum dots. He spent six months at Tyndal Institute (Cork, Ireland), where he studied the emission properties of interstitial defects in germanium quantum dots using density-function theory, under the supervision of Dr. Murphy-Armando. During this period, Petr missed experimental work and decided to switch to a Ph.D. in experimental physics.

In April 2019, Petr joined the group of Wolfgang Löffler at Leiden University as a Ph.D. candidate and started mostly experimental work using devices with InGaAs quantum dots embedded in optical cavities. Using resonant optical fields to operate the devices, he improved cross-polarization filtering methods, enabling him to perform cavity-enhanced spin-state spectroscopy and optimize single-photon emission. Having the access to high-quality single photons, he explored their combining and synthesis of multi-photon states in simple linear optics setups.

List of publications

1. P. Klenovský, D. Hemzal, **P. Steindl**, M. Zíková, V. Křápek, and J. Humlíček. *Polarization anisotropy of the emission from type-II quantum dots*. Phys. Rev. B **92**, 241302(R) (2015)
2. P. Klenovský, **P. Steindl**, D. Geffroy, *Excitonic structure and pumping power dependent emission blue-shift of type-II quantum dots*, Scientific Reports **7**, 45568 (2017)
3. P. Klenovský, **P. Steindl**, J. Aberl, E. Zallo, R. Trotta, A. Rastelli, and T. Fromherz, *Effect of second-order piezoelectricity on the excitonic structure of stress-tuned In(Ga)As/GaAs quantum dots*, Phys. Rev. B **97**, 245314 (2018)
4. **P. Steindl**, E. M. Sala, B. Alén, D. Fuertes Marrón, D. Bimberg, and P. Klenovský, *Optical response of (InGa)(AsSb)/GaAs quantum dots embedded in a GaP matrix*, Phys. Rev. B **100**, 195407 (2019)
5. R. S. R. Gajjela, A. L. Hendriks, J. O. Douglas, E. M. Sala, **P. Steindl**, P. Klenovský, P. A. J. Bagot, M. P. Moody, D. Bimberg, P. M. Koenraad, *Structural and compositional analysis of (InGa)(AsSb)/GaAs/GaP Stranski–Krastanov quantum dots*, Light: Science & Applications **10**, 125 (2021)
6. F. Murphy-Armando, M. Brehm, **P. Steindl**, M. T. Lusk, T. Fromherz, K. Schwarz, P. Blaha, *Light emission from direct band gap germanium containing split-interstitial defects*, Phys. Rev. B **103**, 085310 (2021)
7. **P. Steindl**, E.M. Sala, B. Alén, D. Bimberg, P. Klenovský, *On the importance of antimony for temporal evolution of emission from self-assembled (InGa)(AsSb)/GaAs quantum dots on GaP(001)*, New J. Phys. **23**, 103029 (2021)
8. **P. Steindl**, H. Snijders, G. Westra, E. Hissink, K. Iakovlev, S. Polla, J. A. Frey, J. Norman, A. C. Gossard, J. E. Bowers, D. Bouwmeester, and W. Löffler, *Artificial Coherent States of Light by Multiphoton Interference in a Single-Photon Stream*, Phys. Rev. Lett. **126**, 143601 (2021)
9. **P. Steindl**, P. Klenovský, *Dimension-Dependent Phenomenological Model of Excitonic Electric Dipole in InGaAs Quantum Dots*, Nanomaterials **12**, 719 (2022)
10. **P. Steindl**, J.A. Frey, J. Norman, J.E. Bowers, D. Bouwmeester, W. Löffler, *Cross-polarization extinction enhancement and spin-orbit coupling of light for quantum-dot cavity-QED spectroscopy*, submitted, arXiv:2302.05359
11. **P. Steindl**, T. van der Ent, H. van der Meer, J.A. Frey, J. Norman, J.E. Bowers, D. Bouwmeester, W. Löffler, *Resonant two-laser spin-state spectroscopy of a negatively charged quantum dot-microcavity system with a cold permanent magnet*, submitted, arXiv:2303.02763

12. **P. Steindl**, V. Tubío, W. Löffler, *Single-photon addition and photon correlations*, in preparation
13. D. Hemzal, J. Dvořák, F. Münz, J. Čechal, **P. Steindl**, J. Humlíček, *In situ optical characterisation of surface plasmon resonance*, in preparation

Acknowledgments

During my Ph.D. I had the pleasure of working together with many people I would like to acknowledge gratefully. First and foremost, I would like to thank Wolfgang Löffler for our nearly daily interaction when he shared his immense knowledge and enthusiasm for science. It was a great inspiration to me and formed my scientific skills in performing independent research. My research also benefits from occasional discussions with other quantum optics experts at Leiden University, whom I am thankful: Dirk Bouwmeester, Martin van Exter, Michiel de Dood, and Michel Orrit.

I am also grateful to Henk Snijders, a former Ph.D. student in the group, for his guidance and explanatory laboratory work during my first months at Leiden University.

Over the four years, I shared the laboratory struggle and achievements with Matteo Fisicaro and Kirsten Kannevorff. My friends, you have been the cornerstones of the work in the Löffler lab and have a key role in the best memories I made there. Moreover, I want to appreciate the support and enthusiasm of Corné Koks for brainstorming about research at any time of the day. I am also thankful to our secretary Henriette van Leeuwen for her help with all administrative issues.

The research we do is simply impossible without technological development. Thankfully, at Leiden University, we work with an experienced team of engineers with expertise in mechanics and electronics who help turning our ideas into reality. I want to express my deep admiration for all these experts working in fine-mechanical and electronic departments. You repeatedly helped me give form to my simplistic ideas and made the experiments in this thesis possible. Among all, I wish to name Harmen van der Meer, who designed and manufactured all cryogenic-compatible mechanical components, including the sample/magnetic mount discussed extensively in the thesis. For several months I also had very interesting interactions with Harry Visser and Arno van Amersfoort about the electronics for electro-optic modulation of a continuous-wave laser to obtain picosecond-short pulses.

I was always pleased by the number of motivated bachelor and master students interested in doing their thesis projects in our group. As a Ph.D. student, I worked closely with many of them and would like to thank them for their patience with my supervision and for their contribution to my research. Sharing my fascination with photon number statistics, Victoria Domínguez Tubío explored the single-photon-addition mechanism to generate displaced Fock states, the groundwork of Chapter 5. Tessa van der Ent spent hundreds of hours on her bachelor project on the optical characterization of our new sample design and was involved in the trion hunt. Jasper van der Boom did his internship in our group and helped us optimize polarization control in our experiments using Mueller spectroscopy. Another master student, Ilse Kuijf, explored the capabilities of fiber-based electro-optic modulation of continuous-wave laser into picosecond-long pulses for our single-photon generation. I also acknowledge the dedication and hard work of Edward Hissink and Gerard Westra, who helped with the complex experiments in Chapter 6.

Additionally, I am grateful for the collaboration with the group of John Bowers from UC Santa Barbara, in particular with John Frey and Justin Norman, who designed and

fabricated the samples used in this thesis.

Doing science is always more motivating if one is part of a community. I was lucky to be a member of the newly forming international team of experts in the European project Qluster. Despite the physical exchange of enthusiasm and knowledge being limited by the covid pandemic, we had several great online sessions and an exhilarating two-day meeting in Leiden. I want to express special thanks to Nathan Coste, who arranged my visit to the laboratories of Pascale Senellart (CNRS Paris) and Paul Hilaire for extensive discussions about photonic states.

Over the course of my Ph.D., I got to know some great people who made LION a wonderful place to be. A special thanks to Norman Blümel, Peter Neu, Jimi de Haan, Guido Stam, Xing Chen, Mio Poortvliet, Stephano Polla, Alicja Dutkiewicz, Vitaly Fedoseev, Leon Raabe, Xinrui Wei, Willem Tromp, Amber Mozes, Kier Heeck, Felix Smits, Tom van der Reep, Erik Baalbergen, and others I shamefully forgot to mention.

For the support of my scientific hobby - a curiosity in exotic quantum dot systems, I want to appreciate scientists, working with me since my master's studies, especially Petr Klenovský, who introduced me to the field.

Finally, I am indebted to my family and friends who have respected and supported my decision to move to the Netherlands and dedicate over four years of life nearly entirely to science. Last but not least, this endeavor would not have been possible without my partner Anna, who has stood by me in every moment of this incredible journey.

